Plasmonic metasurfaces to tailor second harmonic generation

PAR

Kuang-Yu YANG

EPFL

ÉCOLE POLYTECHNIQUE
FÉDÉRALE DE LAUSANNE

Suisse
2018

Acknowledgements

I always believe that there is a fascinating mechanism behind every complex phenomenon. For gaining more insight into a physical mechanism which might be the key finding for the next technology, the most precious gift is time. Doing fundamental studies, I have realized how limited I am in front of the unexpected challenges and how important it is to tightly connect with people in different areas of expertise. I have truly found the meaning in the words of wisdom from an admired teacher: "The ultimate purpose in one's life is to help each other to fulfilling their own mission". I am grateful for countless supports and comments I got from the people I met during my PhD.

I first want to express my sincere gratitude to my advisor, Prof. Olivier Martin, for giving me the opportunities to do research with him and setting high standards in every required scientific skill. During every discussion with him, I learned how to obtain a better understanding of a complex optical phenomenon by simplifying the studied system with clear physics concepts. I would also like to thank him for always reminding me to concentrate on dealing with my defects and firmly improving it when I was at a loss to know how to move on. Many thanks to my co-advisor, Jeremy Butet, for many insightful advice and valuable discussions regarding to both experiments and simulations. They were extremely helpful for leading to a good understanding of physical mechanisms. I also, thank him for carefully checking my thesis and helping me to prepare my PhD private defense. I was fortunate to work with you in the nonlinear plasmonic team.

I want to thank my thesis committee Prof. Hans Peter Herzig, Prof. Ventsislav Valev, Dr. Olivier Demichel and Prof. Christophe Moser for thoroughly checking my thesis and providing fruitful discussions during the defense. It was a great pleasure and amazing experience for me to present my work and sharing ideas with you.

During these 4 years, I have a wonderful time staying with fascinating people in Nanophotonics and Metrology Laboratory (NAM). Thanks to Chen for the daily brainstorming and the knowledge of Fourier-imaging setup, I will always remember the moment when we observed the color-routing effect in the designed metasurfaces. Thanks to Gabriel for developing the eigenmode calculation which is extremely helpful for confirming the second-harmonic plasmonic modes supported by the double-resonant antenna. Thanks to Xiaolong for your supports on the nanofabrication and the spicy Chinese Fondue. Thanks to Raziman for checking the writing of my thesis and breakdown service when I needed urgent help in Istanbul. Thanks to Christian, Mohsen, Luc and Alessandro for sharing a broad range of life experience and scientific knowledge during each "balcony time". Thanks to Hsiang-Chu for sharing delicious Taiwanese food with me during my thesis writing. Thanks to Debdatta for sharing your presentation experience with me, which have been extremely useful for my presentation of the defense. Thanks to Toraf for always sharing insightful opinions on optics with humorous and cool style. Thanks to Maryam, Michail, Jenna, Giorgio, Madasamy, Dong Cheon and Hao Wang for your friendships

Abstract

Second harmonic (SH) generation (SHG) in plasmonic nanostructures originates from the surface of centrosymmetric metals where inversion symmetry is broken. The interest in that topic stems from the strong near-field enhancement on the surface of plasmonic nanostructures when the corresponding surface plasmon resonance is excited under far-field illumination, which can greatly increase the SH polarization in a deep subwavelength area, the so-called plasmonic *hot spot* (an area where the field is enhanced by several orders of magnitude). Therefore, plasmonic nanoantennas can serve as an efficient SH nanosource with relaxed SH phase-matching conditions. Furthermore, the SH emission is highly sensitive to the geometrical changes in the plasmonic system. Thus, the emission pattern of SHG can be drastically modified by the size and shape of plasmonic nanoantennas. In this thesis, different plasmonic effects are investigated and demonstrated in conjunction with the design of nonlinear metasurfaces to enhance and manipulate SHG.

In the first work reported therein, we study the mechanisms of SH enhancement in double-resonant aluminum nanoantennas supporting plasmonic dipolar modes at both fundamental and SH wavelengths. For this purpose, the plasmonic dipolar resonance at the fundamental wavelength was first optimized by an appropriate length of the long bar of double-resonant antennas (DRAs), while the short bar length was changed in a way such that the supported plasmonic dipolar mode can be tuned around the SH wavelength. By combining surface integral equation (SIE) simulations with optimized aluminum nanofabrication and sensitive measurements performed by multi-photon scanning microscope, the maximum SH intensity is clearly observed in the case when the short bar supports a plasmonic dipolar mode at the SH wavelength. The SH near-field distribution clearly confirms that the maximum enhancement of SHG is reached when the near-field coupling between the SH quadrupolar mode and SH dipolar mode is the strongest. Indeed, with the developed area-selective nonlinearity SIE method, the energy transfer between the SH quadrupolar mode and SH dipolar mode in such system can be clearly identified. These results provide a full understanding of the mechanisms of SH enhancement in the multi-resonant plasmonic nanoantennas which are important for the design of efficient SH nanoantennas for coherent extreme-ultraviolet nanosources and ultra-sensitive nonlinear refractive index sensors.

In the second work, we combine both experiments and SIE simulations to investigate ultra-thin metasurfaces composed of 3D gold nanopillars, which enable the control of the dependency of induced nonlinear polarization upon the incident wavevector of excitation light. By changing the tilted angle of 3D gold nanopillars, the asymmetric nonlinearity of the metasurface is investigated in details using a homebuilt flexible nonlinear Fourier microscope. As expected, the SH intensity from symmetric nanopillars is identical for negative and positive incidence angles. In this case, the maximal SH intensity is obtained for the highest incident angles reachable with the microscope objective. However, as soon as the tilt angle increases, the SH response becomes asymmetric. In this case, the plasmonic mode can only be excited with negative incident angle, since, for the positive angle, the incident electric field cannot be parallel to the nanopillar axis. Consequently, a variation of the SH intensity close to 80 is measured for opposite illumination angles, revealing a very high asymmetry in the SH response of the nanopillar metasurfaces. The asymmetry in the SH response comes from a modification in the interaction between the inci-

dent wave and the tilted nanopillars, modifying the strength of the nonlinear local sources. Interestingly, the observed specular reflection of SHG, without nonlinear scattering, emphasizes the design of homogeneous nonlinear source distributions. This work paves the way for the optimal design of directional nonlinear plasmonic meta-mirrors.

Finally, we propose a reflective phase-gradient metasurface that can convert a free-space propagating wave into an unidirectional hybrid surface plasmon wave supported on its silver backplate with nearly 80% absorption efficiency at a 800 nm excitation wavelength, leading to a SH enhancement as high as 235 folds in the measurements. The phase-gradient metasurface is designed and optimized to support an anomalous reflection channel at 800 nm following the generalized Snell's law. Interestingly, at specific incident angles, slightly larger than the one turning the anomalous beam into an evanescent wave, a plasmonic hybrid mode resulting from the interaction between localized and propagating plasmons is observed. The corresponding near-field distributions exhibit both the characteristics of localized and propagating plasmons, and the Poynting vector pointing out the unidirectional propagation of the hybrid plasmon mode. One might relate the hybrid plasmon mode to the spoof surface plasmons propagating along the corrugated metallic surfaces with periodically arranged subwavelength parallel metal plates due to the similarity of dispersion relationships. However, spoof surface plasmons are surface-bound electromagnetic waves at terahertz and microwave frequencies such that metal behaves as perfect electric conductor. Therefore, the spoof plasmons has different mechanism of near-field confinement in comparison of that for the hybrid plasmon wave. Indeed, the former is composed of waveguide modes confined in each parallel metal plate on the corrugated metal surfaces. To understand the mechanisms of SH enhancement when the hybrid plasmon wave is excited, we compare numerically two cases, the nonlinear susceptibility being applied either on the nanoantenna (case I) or on the silver mirror (case II). A strong SHG is revealed in case II when the incident angle is such that the hybrid plasmon mode is excited at the fundamental wavelength, indicating that the strong SH enhancement for the hybrid plasmon mode comes from the silver backplate. Interestingly, the single-channel SH emission governed by the SH phase-matching condition reveals the relationship of SH emission channel and excited hybrid plasmon mode in the designed metasurface. The unidirectional and confined propagation for the hybrid plasmon mode can boost the light-matter interactions along the in-plane direction, which provides a new scheme to enhance the SH efficiency by in-plane SH phase matching in the subwavelength-thick nonlinear metasurfaces.

IV

Résumé

La génération de second harmonique (acronyme anglais SHG) dans des nanostructures plasmoniques émane de la surface des métaux où la symétrie d'inversion est brisée. L'intérêt dans ce domaine découle de la forte exaltation du champ proche de la surface des nanostructures plasmoniques lorsque la résonance plasmonique de surface correspondante est excitée par la lumière incidente, ce qui peut augmenter considérablement les sources SHG dans un volume sub-longueurs d'onde appelé point chaud plasmonique (zone où le champ est exalté par plusieurs ordres de grandeur). C'est pourquoi, les nano-antennes plasmoniques peuvent servir comme nano-sources efficaces de SHG. De plus, l'émission de SH est hautement sensible aux changements géométriques dans le système plasmonique. Dès lors, le diagramme d'émission de SHG peut être radicalement modifié par la taille et la forme des nano-antennes plasmoniques. Dans cette thèse, un large éventail d'effets plasmoniques est analysé et démontré dans les méta-surfaces non-linéaires conçues afin d'améliorer la SHG ainsi que d'introduire des manipulations avancées de l'émission non linéaire.

Dans un premier temps, nous avons étudié les mécanismes d'amélioration de la SHG pour des nano-antennes à double résonance en aluminium supportant un mode dipolaire plasmonique à la fois fondamental et à la longueur d'onde harmonique. A cet effet, la résonance plasmonique dipolaire à la longueur d'onde fondamentale a, tout d'abord, été optimisée par une longueur appropriée de la longue barre d'une antenne double résonante (acronyme anglais DRA), tandis que la longueur de la petite barre a été ajusté de telle sorte que le mode dipolaire plasmonique supporté puisse être réglé autour de la longueur d'onde de SH. En combinant des simulations par équations d'intégrales de surface (acronyme anglais SIE) avec une nanofabrication optimisée en aluminium et des mesures sensibles effectuées à l'aide d'un microscope multi-photons à balayage, l'intensité maximale SH est clairement observée dans le cas où la petite barre supporte le mode dipolaire plasmonique à la longueur d'onde de SH. La distribution SH en champ proche confirme nettement que l'amélioration maximale de SHG est atteinte lorsque le couplage en champ proche entre le mode quadrupolaire SH et le mode dipolaire SH est à son maximum. En effet, avec la méthode SIE de surface sélective, le transfert d'énergie entre le mode quadrupolaire SH et le mode dipolaire SH dans un tel système peut être clairement identifié. Ces résultats fournissent une compréhension complète des mécanismes d'amélioration de la SHG dans les nano-antennes plasmoniques multi-résonantes, ceci étant important pour la conception de nano-antennes SH efficaces pour des nano-sources à ultraviolet extrême cohérentes et des capteurs d'indice non-linéaires ultra-sensibles.

Dans un second temps, nous avons combiné à la fois des approches expérimentales et SIE pour analyser des méta-surfaces ultrafines composées de nanopiliers 3D en or, qui permettent de contrôler la dépendance des polarisations induites non-linéaires selon le vecteur de l'onde incidente d'une lumière d'excitation. En changeant l'angle d'inclinaison de nanopiliers 3D en or, la non-linéarité asymétrique des méta-surfaces est analysée en détail via un microscope flexible fait maison i.e. un microscope de Fourier non- linéaire. Comme attendu, l'intensité de SH des nanopiliers symétriques est identique pour des angles d'incidence négatifs et positifs. Dans ce cas, l'intensité maximale de SH est obtenue pour les plus grands angles d'incidence atteignables avec l'objectif du microscope. Cependant, dès que l'angle d'inclinaison augmente, la réponse SH devient asymétrique. Dans ce cas, le mode plasmonique peut seulement être excité avec des

angles d'incidence négatifs puisque, pour des angles positifs, le champ électrique incident ne peut pas être parallèle à l'axe des nanopiliers. Par conséquent, une variation de l'intensité SH proche de 80 est mesurée pour des angles d'illumination opposés, révélant une très grande asymétrie dans la réponse SH des méta-surfaces composées de nanopiliers. L'asymétrie de la réponse SH vient de la modification de l'interaction entre l'onde incidente et les nanopiliers inclinés, ce qui modifie la force des sources locales non-linéaires. Etonnamment, la réflexion spéculaire de SHG observée, sans dispersion non-linéaire, accentue la conception des distributions de sources homogènes non-linéaires. Ce travail ouvre la voie à une conception optimale des méta-miroirs dirigés plasmoniques non-linéaires.

Enfin, nous proposons une méta-surface réfléchissante à gradient de phase qui peut convertir une onde se propageant librement dans l'espace en une onde de plasmons de surface hybride et unidirectionnelle, supportée sur sa plaque arrière en argent avec une efficacité d'absorption proche de 80% à une longueur d'onde d'excitation de 800 nm, menant à une amélioration de la SHG de 235 foiss via les mesures. La méta-surface à gradient de phase est conçue et optimisée pour supporter un canal de réflexion anormal à 800 nm suivant la loi généralisée de Snell-Descartes. Curieusement, à des angles d'incidence spécifiques, légèrement plus grands que celui transformant le faisceau anormal en une onde évanescente, un mode hybride plasmonique résultant de l'interaction entre les plasmons localisés et se propageant a été observé. Les distributions en champ proche correspondantes montrent aussi bien les caractéristiques de plasmons localisés et se propageant, et le vecteur de Poynting montre la propagation unidirectionnelle du mode de plasmon hydride. Pour comprendre les mécanismes d'amélioration de la SHG, nous comparons numériquement deux cas, la susceptibilité non-linéaire étant appliqué soit sur la nano-antenne (cas I) soit sur le miroir en argent (cas II). Une forte SHG est observée dans le cas II lorsque que l'angle d'incidence est tel que le mode de plasmon hybride vient de la plaque arrière en argent. L'émission SH en simple canal gouvernée par la condition d'adaptation de phase SH révèle la relation entre le canal d'émission SH et le mode de plasmon hybride excité dans la méta-surface conçue. La propagation unidirectionnelle et confinée pour le mode de plasmon hybride peut renforcer les interactions lumière-matière le long de la direction de propagation dans le plan, ce qui offre un nouveau schéma pour améliorer l'efficacité de la SHG par adaptation de phase SH dans le plan dans les méta-surfaces non-linéaires sub-longueurs d'onde.

Mots-clés: Génération de second harmonique, résonance de plasmon de surface localisée, onde de plasmons de surface hybride, antenne double résonante, couplage plasmonique, non-linéarité des vecteurs d'onde sélectifs, miroirs plasmoniques non-linéaires, loi généralisée de Snell-Descartes, méta-surfaces plasmoniques, méta-surfaces non-linéaires, imagerie non-linéaire par plan de Fourier, champ proche.

Contents

1. Introduction and thesis objectives

1.1 History and origin of nonlinear harmonic generation

In 1960, Maiman *et al.* built the first laser system using a ruby crystal as the gain medium [1]. The invention of high power coherent light sources can be applied to enhance light-matter interaction and thus opens up the possibility to modify the optical response of the exposed materials. Shortly after the first demonstration of an operating laser system, in 1961, Franken *et al.* reported the first observation of SHG from a quartz crystal [2]. The generated nonlinear signal from the quartz crystal exhibits mainly two unique characteristics, distinct from that of the linear optical response: First, its frequency is twice that of the pump laser. Secondly, its intensity increases quadratically with the intensity of the pump laser. The underlying physical mechanisms leading to SHG can be understood by first expressing the wave equation in nonlinear optical media [3, 4]

$$\nabla^2 \mathbf{E}^{NL} - \frac{n^2}{c^2}\frac{\partial^2 \mathbf{E}^{NL}}{\partial t^2} = \frac{1}{\varepsilon_0 c^2}\frac{\partial^2 \mathbf{P}^{NL}}{\partial t^2},\tag{1.1}$$

where n is the refractive index of the medium, c is the speed of light in vacuum, ε_0 is the permittivity of vacuum, $\mathbf{P}^{NL}$ is the nonlinear polarization associated with the nonlinear optical response in the medium and $\mathbf{E}^{NL}$ is the electric field driven by $\mathbf{P}^{NL}$. This means that the oscillating nonlinear polarization generated in the medium acts as a SH source and radiates SH light. In order to contribute to the radiation, a non-vanishing $\frac{\partial^2 \mathbf{P}^{NL}}{\partial t^2}$ term is required in this equation, which is consistent with Larmor's theorem of electromagnetism: Accelerated charges can generate electromagnetic radiation [5]. In addition, this equation clearly shows that the frequency of the radiated light is determined by the oscillation frequency of the nonlinear polarization. Indeed, if we expand the time-varying polarization $\mathbf{P}(t)$ into a power series as a function of the electric field of the pump laser $\mathbf{E}(t) = Ee^{-i\omega t}$,

$$\begin{aligned}\mathbf{P}(t) &= \varepsilon_0 \left[\chi^{(1)}\mathbf{E}(t) + \chi^{(2)}\mathbf{E}^2(t) + \chi^{(3)}\mathbf{E}^3(t) + \cdots \right] \\ &= \varepsilon_0\chi^{(1)}Ee^{-i\omega t} + \varepsilon_0\chi^{(2)}E^2 e^{-i2\omega t} + \varepsilon_0\chi^{(3)}E^3 e^{-i3\omega t} + \cdots \\ &\equiv \mathbf{P}^{(1)}(t) + \mathbf{P}^{(2)}(t) + \mathbf{P}^{(3)}(t) + \cdots.\end{aligned}\tag{1.2}$$

The quantities $\chi^{(1)}$, $\chi^{(2)}$ and $\chi^{(3)}$ are known as the linear, second-order and third-order optical susceptibilities, respectively. The linear polarization, second-order nonlinear polarization and third-order nonlinear polarization are denoted as $\mathbf{P}^{(1)}(t)$, $\mathbf{P}^{(2)}(t)$ and $\mathbf{P}^{(3)}(t)$, respectively. We can

1

notice that the second- and third-order nonlinear polarizations have distinct oscillation frequencies at 2ω and 3ω when the frequency of the excitation light is ω, which explains the relationship between the wavelength of the generated optical signal and that of the pump laser. Furthermore, the quadratic dependence of the second-order nonlinear polarization on the amplitude of incident electric field, and the third-order dependence for third-order nonlinear polarization are evidenced by this equation.

1.1.1 Practical applications based on nonlinear optics

The birth of the first laser, as well as the discovery of nonlinear optical response, has led to several important applications and shaped the evolution of modern optics. The frequency conversion, i.e. harmonic generation, has been commonly applied to convert the output of a fixed-wavelength laser to a different spectral range. For instance, by the mid-1970s, the second, third and fourth harmonics from Q-switched Nd:YAG lasers (operating in near infrared, at 1064 nm) were routinely utilized to generate coherent light at 532 nm, 355 nm and 266 nm ranging from the visible to the ultraviolet parts of the spectrum with the help of a potassium dideuterium phosphate (KDP) crystal [6, 7]. Another type of application is relying on the frequency matching between the nonlinear signal and atomic transitions in an atomic/molecular system. In this case, the transition between the two energy levels of the material system can be achieved by absorbing the nonlinear signal generated in the same system, and the relaxation of the excited state can result in a spontaneous emission. By employing a wavelength-tunable pulsed laser as the excitation source of nonlinear microscope, the energy levels of excited states in atomic systems can be characterized by nonlinear optical processes such as two-photon absorption [8, 9]. Furthermore, Doppler broadening of spectral lines due to the motion of analyzed atoms can be eliminated by sending two laser beams with identical frequency in opposite directions. In this case, for an atom moving toward one of the laser beams, the Doppler shift of apparent excitation frequency can be compensated with another beam illuminated from the opposite direction, which keeps the same total energy for two-photon transition as that from a rest atom [10]. The two-photon Doppler-free spectroscopy enables the possibility to probe the atomic transitions with extremely high precision in ambient temperature [11-13]. Nonlinear spectroscopy, initially developed by Bloembergen and Schawlow, was acknowledge by the 1981 Nobel Prize in physics [10]. Another important application in nonlinear optics is nonlinear microscopy [14-17]. The main advantages of the nonlinear microscope, such as enhanced spatial resolution and background-free imaging are associated with the nonlinear signal-input power dependence and frequency conversion, respectively [18, 19]. For example, the transverse and longitudinal resolutions are enhanced since the nonlinear signals are generated most efficiently in the region of maximum intensity of a focused laser beam. This provides a powerful tool to acquire three-dimensional images with subwavelength resolution even for a transparent (phase) object, as the investigation of biological samples with nonlinear confocal microscopes for example [16, 20].

1.1.2 Symmetry and second-order nonlinear susceptibility

Although the development of high power laser systems is essential for enhancing the nonlinear optical signal for practical applications, the exploration of the nonlinear materials/crystals also plays a key role for mastering various nonlinear optical processes. For example, it is well-established that SHG is forbidden in crystals with inversion symmetry in the electric dipole approximation [21-23]. The vanishing second-order nonlinear susceptibility $\chi^{(2)}$ inside such a material can be understood by first expressing the second-order nonlinear polarization as

$$\mathbf{P}^{(2)}(t) = \varepsilon_0 \chi^{(2)} \mathbf{E}^2(t). \tag{1.3}$$

Now, if we change the sign of the incident electric field $\mathbf{E}(t)$, the sign of the nonlinear polarization must change accordingly since we consider a centrosymmetric material:

$$-\mathbf{P}^{(2)}(t) = \varepsilon_0 \chi^{(2)} \left[-\mathbf{E}(t) \right]^2. \tag{1.4}$$

By comparing Eq. (1.4) with Eq. (1.3), one can recognize that the right-hand sides of both equations are identical. This is due to the fact that SHG is a nonlinear optical process with a quadratic dependence between the nonlinear polarization and the incident electric field. Consequently, $\mathbf{P}^{(2)}(t)$ must equal to $-\mathbf{P}^{(2)}(t)$ which can only be satisfied when $\chi^{(2)} = 0$, demonstrating that the second-order nonlinear susceptibility $\chi^{(2)}$ vanishes in centrosymmetric materials. In contrast, the third-order nonlinear susceptibility $\chi^{(3)}$, related to third harmonic generation (THG) for example, with a third-order dependence between the nonlinear polarization and the incident electric field, does not vanish in a centrosymmetric medium and possess different symmetry properties [3].

1.1.3 Phase-matching and quasi-phase-matching conditions

In order to accumulate the nonlinear signal along the propagation direction of the input light, the phase of the local nonlinear polarizations must be spatially arranged in such a way that the generated nonlinear signal adds coherently during the propagation. This is known as the phase-matching condition. To discuss this phase-matching condition in more details, we consider a z-polarized plane wave propagating along the $+x$ direction in a lossless nonlinear medium. For simplicity, if we consider at a specific time such that the incident electric field is $\mathbf{E}_z(x = 0) = E_z \hat{z}$ at the entrance of the nonlinear crystal ($x = 0$), at the position $x = \frac{2\pi}{k_\omega}$ inside the nonlinear crystal (k_ω is the wavevector of input laser in the medium with frequency ω), the incident electric field reaches the same value again as $\mathbf{E}_z(x = \frac{2\pi}{k_x}) = \mathbf{E}_z(x = 0) = E_z \hat{z}$. Consequently, the generated nonlinear polarizations at these two positions are in-phase, i.e. $\mathbf{P}_z(x = \frac{2\pi}{k_\omega}) = \mathbf{P}_z(x = 0) = P_z \hat{z}$. At the position $x = \frac{2\pi}{k_\omega}$, the electric field induced by the ''first'' nonlinear polarization (at $x = 0$) must be in-phase with the ''second'' nonlinear polarization (at $x = \frac{2\pi}{k_\omega}$) in order to allow the generated

3

nonlinear signals adding coherently along the +x direction. Since the electric field induced by the "first" nonlinear polarization is associated with the spatial dependence $e^{-ik_{n\omega}\cdot\frac{2\pi}{k_\omega}}$ at $x = \frac{2\pi}{k_\omega}$ ($k_{n\omega}$ is the wavevector of the generated harmonic wave in the medium with frequency $n\cdot\omega$). Hence the in-phase requirement results in $k_{n\omega} = nk_\omega$ in the nonlinear medium, which leads to the well-known phase-matching condition where the wavevector mismatch Δk must be zero

$$\Delta k = nk_\omega - k_{n\omega} = 0.\qquad(1.5)$$

Please note that n depends upon the considered nonlinear harmonic, for example, $n = 2$ for SHG whereas $n = 3$ for THG. This condition has been found difficult to be satisfied due to the chromatic dispersion. The variation of the refractive index at the pump and harmonic frequency in the medium leads to a non-zero wavevector mismatch and limits the overall nonlinear output signal. The most common solution to achieve the phase-matching condition is to make use of birefringence [24]. However, the idea to compensate the dispersion with birefringence cannot be realized if the nonlinear crystal possesses insufficient birefringence. Another promising technique to compensate the wavevector mismatch, namely nonlinear quasi-phase-matching, was first demonstrated by Armstrong *et al.* in 1962 [25]. This method introduced a periodically reversed sign of nonlinear susceptibility in the layered nonlinear medium. The sign reversal is launched at the positions where the wavevector mismatch is sufficiently large to result in a decrease of the amplitude of the generated wave. Consequently, reversing the sign of the nonlinear susceptibility corrects the phase of the newly generated nonlinear polarization and reduces its phase difference with the harmonic field generated by the previous nonlinear polarizations, which enables the field to grow continuously along the propagation of input light. The periodicity Λ of the sign reversal can be designed from the quasi-phase-matching condition given by

$$\Delta k = nk_\omega - k_{n\omega} - \frac{2\pi}{\Lambda} = 0.\qquad(1.6)$$

Comparing with the phase-matching requirement shown in Eq. (1.5), quasi-phase-matching technique introduces a grating momentum $\frac{2\pi}{\Lambda}$ to compensate for the wavevector mismatch originating from the chromatic dispersion of the nonlinear medium.

1.1.4 Surface properties probed by SHG

SHG is forbidden in the bulk of centrosymmetric objects in the electric dipole approximation. However, the inversion symmetry is broken at interfaces due to the finite dimension of the atomic lattice, which permits a non-vanishing SH polarization at the surface [26]. This surface contribution of SHG can be understood by the net SH polarization locally induced at the interface due to the difference between the nonlinear susceptibilities of two mediums. Therefore, SHG was found to be an extremely versatile tool for studying surface properties with a very high surface specificity and sensitivity [26-28]. For example, structure discontinuity is dominant at the dangling bonds on a silicon surface [29]. In addition, SHG can be applied to probe the symmetry of a crystalline structure by recording the SH intensity while varying the incident polarization. For example, a freshly cleaved Si(111) surface which has a structure characterized by a (2×1) low-energy electron diffraction (LEED) pattern, and this specific structural symmetry is reflected in the variation of SHG as a function of incident polarization [30]. In 1973, surface probing by SHG was found for the first time able to detect a sub-monolayer of metallic atoms deposited on a semiconductor surface [31]. The SHG intensity due to a single monolayer of Na coverage on the Ge substrate is about ten times higher than that for the clean Ge surface. Since then, the surface SH probing has been extensively adopted to study molecule-substrate interactions at various surfaces [32-37]. Probing the oxygen adsorption on a rhodium surface with monolayer resolution is a remarkable demonstration of SHG ability for gas sensing [32]. The adsorbed oxygen molecules tend to localize the free electrons at the rhodium surface and thus reduce the SH nonlinearity. Moreover, surface SH probing also allows *in situ* mapping of molecule arrangements and species monitoring thanks to the sensitive detection of the orientation of polar molecules [38, 39]. For example, it was found that the retinal chromophores adsorbed on membranes tend to have a certain polar alignment, which leads to a strong SHG signal [40]. Finally, surface SHG is highly directional with ultra-fast response time as a coherent nonlinear optical process. The employment of ultrafast laser pulses to generate SHG can further extend the technique to monitor the dynamics of fast molecule-surface reactions in real time [33, 34, 41, 42]. These advantages, together with the capability of surface probing in an ambient environment, make surface SH probing a sensitive and versatile tool for surface studies.

1.2 SH emission in plasmonic nanostructures

The physical mechanism underlying the first observation of SH enhancement from a sub-monolayer of metallic Na atoms was unclear at that time. The surface-enhanced nonlinearity in metals was rediscovered in an experiment comparing the SHG from a smooth and a 50-nm roughened silver surface [43]. The reflected SHG was enhanced by a factor of 10^4 as surface roughness is introduced. This enhancement was found to be correlated with the local field enhancement induced by the excitation of surface plasmon polaritons (SPP) propagating on the surface of a rough silver film. The strong field confinement of SPP on the metal surface is favorable to the enhancement of surface SHG. Furthermore, even higher degree of field confinement can be yielded in metallic nanoparticles supporting localized surface plasmon resonances (LSPR), resulting in a stronger near-field than SPP. Therefore, the plasmonic nanoparticles can be considered as efficient nonlinear sources thanks to the near-field enhancement at the nanoscale. Significantly, the size and shape of nanoparticles can drastically modify the emission pattern of SHG due to fascinating symmetry consideration in the SHG from plasmonic nanostructures.

1.2.1 Surface plasmon polaritons

Surface plasmons are the collective electron plasma oscillations at a metal surface driven by electromagnetic excitations [44]. These longitudinal oscillations of free electrons can only be launched at the metal surface due to the fact that no electromagnetic field can propagate in the metal with a negative dielectric constant when the frequency of light is lower than the plasma frequency of the metal. If we consider the case of a semi-infinite metal-dielectric interface (located at $z = 0$), the electric field distribution of the SPP propagating along $+x$ direction can be expressed as

$$E_{sp}(x, z) = E_0 e^{ik_{sp}x - k_z|z|}.$$ (1.6)

The field expression indicates that the wave is strictly propagating along the interface with the propagation vector $k_{sp} = \frac{2\pi}{\lambda_{sp}}$, and the field is confined close to the metal surface with the exponential decay away from the surface determined by the decay constant k_z [45]. The highly confined electric field at the metal surface leads to a significant field enhancement. Depending on both the dielectric constant and radiative losses, the maximum intensity at the interface can reach 2 orders of magnitude higher than that of the illuminated red light for a 60-nm thick silver film [46]. For a flat metal surface, the non-radiative feature of SPP implies that it cannot be directly excited by a free-space propagating wave. The dispersion relation of SPP supported on a smooth metal surface is given by

$$k_{sp}(\omega) = \frac{\omega}{c} \sqrt{\frac{\varepsilon_m \varepsilon_d}{\varepsilon_m + \varepsilon_d}} ,$$ (1.7)

where ε_m and ε_d are the dielectric constants of metal and dielectric background, respectively. Indeed, since the sign of ε_m and ε_d are different, the propagation vector of SPP is always larger than the maximum in-plane wavevector allowed in the dielectric medium $\frac{\omega}{c}\sqrt{\varepsilon_d}$ for a non-zero angular frequency ω. Therefore, in order to excite a propagating SPP on the surface of a semi-infinite metal, gratings, optical scatters or sufficient surface roughness either patterned on or nearby the metal surface are required to provide the required high-k components [46, 47]. On the other hand, for an optically thin metal film, the SPP can be excited by the evanescent wave from the total internal reflection in the famous Otto-Kretschmann configuration. In this case, the incident plane wave impinges on the metal film from a dielectric medium with high refractive index, and the evanescent wave with sufficiently large in-plane wavevector can launch the SPP on the other side of metal film surrounded by the dielectric medium with lower refractive index [48].

The strong near-field enhancement provided by SPP is highly interesting for enhancing the SHG due to the favorable spatial overlap between plasmonic near-fields and non-vanishing SH polarization on the metal surface, which has played a pivotal role in the birth of plasmonic-enhanced SHG. In 1974, enhanced SHG was revealed by a propagating SPP excited at the surface of a 56-nm silver film [49]. Experimentally, the reflected SHG was enhanced by 30 times, in comparison with the non-resonant optically thick silver film.

In addition to the propagating SPP on a plane metal surface, for the metal objects with bounded geometries and subwavelength dimensions, localized surface plasmon resonances can be more prominent. The three-dimensional confinement of LSPRs leads to a higher electromagnetic field enhancement than the propagating SPP [50]. Besides, it should be noted that the LSPR is a different type of excitation from the SPP. The latter should consider both the in-plane wavevector and frequency of the excitation wave to satisfy the dispersion relation as discussed previously. In contrast, LSPRs are only characterized by the frequency which is governed by the size, shape and dielectric constants of the metal objects due to the deep subwavelength confinement of the LSPR modes [50].

1.2.2 SHG in plasmonic nanoparticles

When a noble metal nanostructure is excited by light with the appropriate frequency, the excitation of LSPRs can lead to a strong enhancement of the field in the so-called *hot spot*, which can enhance the nonlinear optical process in nanostructures with size much smaller than the wavelength of the excitation light [51]. Indeed, the enhanced SHG in plasmonic *hot spots* can be clearly visualized and accurately mapped in nanostructures with SHG microscopy by scanning the ultrafast pumped laser spot across the plasmonic resonators. Consequently, the enhancement of SH intensity can be clearly observed when the excitation wavelength matches the resonant wavelength of the LSPR [51, 52]. The SHG from plasmonic nanostructures is found to exceed by 5-orders of magnitude that from the chromophores with a similar size and comparable to that from the nanoparticles composed of nonlinear materials [53, 54]. In order to choose plasmonic materials for efficient SHG, the surface nonlinear susceptibility, as well as the optical properties at both fundamental and SH wavelengths, should be carefully considered. For the

most popular plasmonic materials, gold (Au), silver (Ag) and aluminum (Al), the intrinsic material loss associated with the interband transitions will limit the favorable wavelength range of LSPRs. Indeed, the material loss either at fundamental or SH wavelength can significantly hamper the overall enhancement of SHG. For example, since the interband transition of Al is in the near-infrared region, the plasmonic damping effect will reduce the near-field enhancement induced by LSPRs in this range [55]. Despite that, Al has a low material loss in the visible to ultraviolet spectral range, which is favorable in providing an efficient emission channel for SHG through a near-infrared excitation. In contrast, Au and Ag are good plasmonic materials in the near-infrared region. However, with near-infrared excitation, the SH emission from the Au nanostructures will suffer from the interband absorption for SH wavelengths shorter than 500 nm [56]. For Ag, the interband absorption is located at 310 nm and thus the material loss at the SH wavelength is relatively low in comparison with Au with near-infrared excitation [57]. Additionally, the surface nonlinear susceptibilities $\chi^{(2)}$ of these plasmonic materials are also an important factor for an efficient SHG. In general, the surface nonlinear susceptibility of Al is 1 order of magnitude higher than the other plasmonic materials at a pump wavelength of 800 nm with the following values: 3×10^{-12} cm^2/statvolt for Al, 3.2×10^{-13} cm^2/statvolt for Ag and 2.3×10^{-13} cm^2/statvolt for Au [58]. The higher surface SH susceptibility for Al is related to the larger dielectric constant compared to Au and Ag at near-infrared wavelength, which is correlated with the interband transition of Al in this range [58]. Because of the high surface SH susceptibility and low optical loss in the visible range, Al nanostructures have gained a lot of interest recently in the enhancement of SHG, despite the resonance of Al nanostructure is hampered by the interband absorption at the excitation stage [59-61].

To optimize the SHG in the plasmonic nanostructures, in addition to a plasmonic resonance at the fundamental wavelength, the LSPR modes at the SH wavelength should also be designed in order to allow an efficient emission channel for SHG. The SH intensity enhancement can be clearly observed when the SH wavelength matches with the wavelength of dipolar plasmonic resonance [62]. With all these concepts in mind, an optimal design should consider a plasmonic system providing mode matching at both fundamental and SH wavelengths in order to obtain simultaneously a maximal fundamental excitation and an efficient SH emission. Several designs of multiresonant plasmonic nanostructures have been proved to exhibit a higher SHG than that from the simple plasmonic nanoantenna with only one resonance at the fundamental wavelength [63-65]. For instance, the SH intensity from the Al double-resonant antenna (DRA) supporting plasmonic dipolar modes at both fundamental and SH wavelengths is twice of that from an Al dipolar antenna (DA) supporting only a plasmonic dipolar mode at the fundamental wavelength [60]. The reason why the enhancement of SHG is only two-fold can be understood by considering the double-resonant condition in single Al nanorod. It has been experimentally observed that a single Al nanorod can also support a plasmonic dipolar mode and a plasmonic quadrupolar mode at the fundamental and SH wavelengths, respectively[66, 67]. In the case of Al dipolar antenna, plasmonic quadrupolar modes can be induced on each long nanorod at the SH wavelength. Therefore, a double-resonant condition can also be achieved in Al dipolar antenna under near-infrared illumination limiting the relative enhancement provided by the DRA. As discussed previously, the sources of SHG are situated at the surface of plasmonic nanostructures due to the centrosymmetric crystalline nature of the material. Particularly, the $\chi^{(2)}_{\perp\perp\perp}$ component perpendicular to and pointing outward on the surface of a plasmonic nanoparticle is the

largest component of the nonlinear susceptibility [58, 68, 69]. Therefore, the SH polarization induced on the plasmonic nanoparticles is essentially determined by both the geometry (shape) of the nanoparticles and the excited LSPR modes [70]. The latter correlation explains the quadrupolar SH emission observed in the SHG from plasmonic nanoparticles with centrosymmetric shapes, when a plasmonic dipolar mode is excited at the fundamental wavelength [71]. Indeed, for plasmonic nanostructures with centrosymmetric shape when excited at normal incidence (e.g. plasmonic nanodisc), the generated SH fields perfectly cancel each other in the plane perpendicular to the incident polarization in the electric dipole approximation [72]. To provide an efficient SH intensity in the backward and forward directions, one convenient method is to design a nanostructure with non-centrosymmetric shape when viewed in the direction of normal incidence. Consequently, a net SH dipolar mode can be induced in the plane perpendicular to the normal incidence. For example, L-shaped gold nanostructures, which have been employed as one of the basic plasmonic elements for SHG, can support a SH dipolar mode parallel to the polarization of the incident light [72-76]. Alternatively, plasmonic split-ring resonators (SRRs) with U-shape permit the generation of SH dipolar mode perpendicular to the polarization of the incident light [77-79]. The excited plasmonic magnetic dipolar mode in plasmonic SRRs can achieve a strong near-field enhancement at the fundamental wavelength, establishing the SRRs as a favorable meta-atom for efficient SHG. To further emphasize the importance of non-centrosymmetric nanoparticle shapes for efficient SH emission, one good example is the SH silencing effect observed in the plasmonic dipolar antenna with a narrow gap, although the high near-field enhancement observed in the gap can indeed result in a strong nonlinear polarization [80]. Indeed, the nonlinear polarization vectors at each side of the nanogap are out-of-phase due to the symmetric construction of the nanogaps, which tend to cancel each other out in the far-field [80, 81]. The SH silencing effect can be suppressed by introducing non-centrosymmetric construction of nanogaps such as gold nanodimers with T-shape [82], or inducing an amplitude variation between the nonlinear polarizations at each side of the nanogap by designing an asymmetric dipolar antenna consisting of two arms with different lengths [83]. The above-mentioned nanostructures exhibit symmetry-breaking features along the plane perpendicular to the propagation of excitation light. Thereby, the generated SH dipolar modes are essentially aligned in this plane. One way to tilt the SH dipolar mode out-of-plane is to introduce three-dimensional structural orientation such that SH radiation can be tuned into an inclined direction. For example, three-dimensional gold nanocups have been demonstrated to generate an oblique SH emission which can be controlled by the axis of the tilted nanocups [84]. However, single-channel SH emission with high directionality is challenging to achieve due to the multipolar nature of the single plasmonic nanoantenna [85]. Most recently, controllable SH emission with high directionality has been realized by a two-dimensional arrangement of nonlinear plasmonic meta-atoms, namely nonlinear metasurfaces [86-90]. This fascinating design principle is based on the universal formulation of wavefronts suggested by the Huygens's principle [91]. It was first demonstrated in the plasmonic metasurfaces, which allow extraordinary light manipulation in the linear regime [92-94]. In the following section, we will first describe the universal design principle of wavefront shaping with plasmonic metasurfaces and then review the state-of-the-art of the plasmonic metasurfaces in the linear regime.

1.2.3 Wave-front design and state of the art for linear metasurfaces

According to Huygens's principle, an arbitrary wavefront of an electromagnetic wave in the far-field can be considered as the result of interference of every spherical sources located at the interface [91]. In other words, arbitrary wavefront control can be achieved by engineering the phase/amplitude of these secondary spherical sources with subwavelength spatial resolution [95]. Plasmonic nanostructures supporting LSPRs can serve as artificial secondary sources with the required subwavelength dimensions [96-102]. Moreover, the highly dispersive characteristics of LSPRs permit a phase variation from 0 to 2π around the resonant wavelength of the plasmonic meta-atoms. For instance, 2π phase modulation can be fulfilled by a plasmonic system composed of plasmonic nanoantennas and a metallic backplate spaced by an optically thin dielectric layer as shown in Fig 1:1. The induced currents on the nanoantennas and metallic backplate are antiparallel due to the strong near-field coupling, which leads to a strong magnetic dipole inside the dielectric spacer and thus allows a 2π phase variation close to the resonant wavelength [103-106]. Thanks to this high phase modulation at the nanoscale, plasmonic nanostructures have become popular compounds and building blocks of metasurfaces. Significantly, the local phase modulation with subwavelength spatial resolution offered by plasmonic metasurfaces enables diffraction-free light manipulation in ultra-thin flat metasurfaces [92, 107-111]. The first demonstration of extraordinary light manipulation in metasurfaces is anomalous reflection/refraction, where the introduced phase gradient distribution along the interface provides an additional in-plane momentum and deflects the incident light into an anomalous reflection/refraction channel following the generalized Snell's law [103, 112-114]. Furthermore, as the in-plane momentum becomes sufficiently large, the free-space propagating wave can be converted into a unidirectional surface wave supported on a metallic backplate beneath the top nanoantenna [115-118]. In this case, the light absorption is significantly larger than the one with the anomalous channels radiated out to the far-field. Besides the ability to direct the incident plane wave into an anomalous reflection/refraction channel, a much more complex light manipulation can be achieved with plasmonic metasurfaces. For example, almost all the functionalities of conventional optical components have been reproduced by metasurfaces with only few tens of nanometers device thickness such as metalenses [109, 119, 120], meta-holograms generators [108, 121, 122] and metasurface-based waveplates [123, 124], just to cite a few of the recent achievements. Beyond that, by carefully designing the electromagnetic properties of individual plasmonic constituents, novel functionalities such as wavelength-selective color routing [125] and polarization-selective polarimetry devices [126-128] have been demonstrated. These works elaborate the design principle of wavefront construction with the exceptional optical properties of plasmonic meta-atoms.
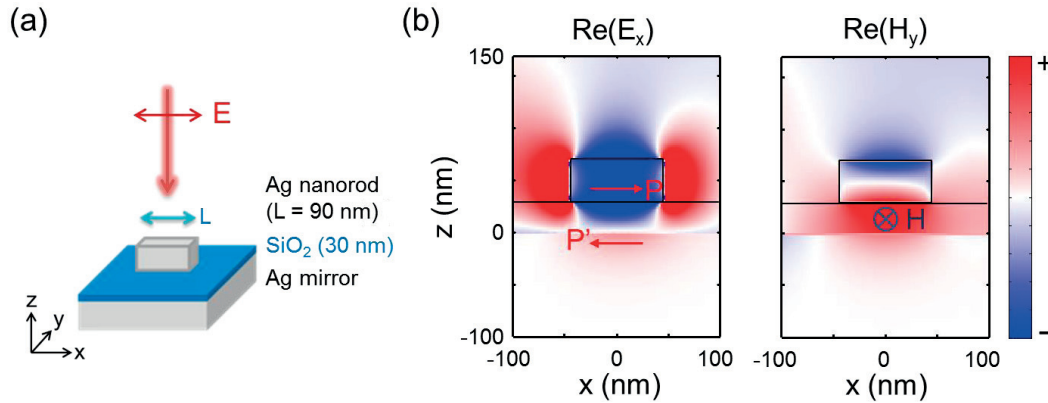
Figure 1:1 Plasmonic-induced magnetic resonance in the metal-dielectric-metal (MIM) nanostructure. The MIM nanostructure is composed of a silver nanorod (length L = 90nm, width and height are both 40 nm) and a silver mirror (200 nm thickness) separated by a thin SiO_2 layer (30 nm thickness) as shown in (a). In the simulation, we considered the periodicity of the arrays of nanorods is 200 nm in both x and y directions. The wavelength of the normal incident light is 800 nm and the polarization is along the nanorod axis (x axis). The background index is 1.5, which is the same as that of SiO_2 spacer. (b) The near-field distributions of the real part of the x-component electric field (left panel) and y-component magnetic field (right panel) in the (X, Z) plane of the MIM nanostructure. The induced dipole moments in the silver nanorod and mirror backplate (red arrows labelled P and P', respectively) are antiparallel generating a strong magnetic dipole moment (blue arrow with H label) in the SiO_2 spacer.

1.2.4 State of the art for the nonlinear metasurfaces

In the above mentioned research on plasmonic metasurfaces in the linear regime, there is no constraint on the shape of constitutive meta-atoms. In contrast, SHG requires exploiting their symmetry in order to optimize the emission from individual nonlinear elements. Nevertheless, to construct a specific wavefront in the far-field, the required spatial phase distributions for linear and SH fields follow the same design principle. Furthermore, as the phase distribution is performed by the phase delay of individual plasmonic constituent, the metasurfaces can then be equivalent to an optical slab with continuously varying linear/nonlinear material properties along the plane [129]. Indeed, the linear phase/amplitude response is essentially associated with the effective refractive index for the plasmonic meta-atoms according to the effective-medium theory [129-131]; Whereas, the nonlinear phase/amplitude response is governed by the local effective hyperpolarizability of the nanoantennas [86, 132]. For example, a π phase shift of SH radiation can be induced by reversing the nonlinear polarizability of the local SH sources [86]. This concept had been realized by the electric poling techniques using poled ferroelectric materials to achieve the quasi-phase-matching condition in nonlinear crystals [133]. Unlike the electric poling technique which requires applying a voltage to the ferroelectric materials, the artificial poling in the nonlinear metasurfaces has been performed by simply reversing the orientation of the SRRs [86]. Binary nonlinear phase engineering along the interface can manipulate the diffraction angle of SH emission with high directionality [86]. However, the diffraction effect is inevitable due to the present of phase singularities at the location where the phase of SH field changes abruptly from 0 to π. To achieve diffraction-free SH manipulation, a continuous and

full 2π phase modulation for SHG is necessary. This requirement can be accomplished by applying the nonlinear geometric Berry phase approach which works under a circularly polarized excitation to plasmonic metasurfaces. A full phase control can be acquired by rotating the plasmonic meta-atoms with identical geometry [89]. In order to understand the nonlinear geometric Berry phase induced by rotating the nanostructures, we can first look at the geometric Berry phase in the linear regime as the phase of harmonic waves is related to that of linear response. For a circularly polarized excitation light propagating along the rotation axis of a meta-atom, the excitation wave acquires a geometric phase in propagating through the structure. For a nanostructure with a rotation angle of θ, the electric field of fundamental light and the SH polarization can be expressed as $E_L^{\omega} = E^{\sigma}\, e^{i\sigma\theta}$ and $P_L^{2\omega} = \chi_L^{(2)}\left(E^{\sigma}\right)^2 e^{i2\sigma\theta}$, respectively. Here, we define $\sigma = \pm 1$ for left-handed circular polarization (LCP) and right-handed circular polarization (RCP) of excitation light, respectively. The SH polarization induced on the structure can be decomposed into two circular polarization states as $P_L^{2\omega} = P_{L,\sigma}^{2\omega} + P_{L,-\sigma}^{2\omega}$. Please note that till now we consider the electric field and SH polarization in the local coordinate L with axes rotated by θ with respect to the laboratory coordinate O. After transforming back to the laboratory coordinate, the left- and right-handed components of the SH polarization are given by $P_{O,\sigma}^{2\omega} = P_{L,\sigma}^{2\omega}\, e^{-i\sigma\theta} \propto e^{i(2-1)\theta}$ and $P_{O,-\sigma}^{2\omega} = P_{L,-\sigma}^{2\omega}\, e^{i\sigma\theta} \propto e^{i(2+1)\theta}$, respectively [89]. Therefore, the induced SH polarization will have the relative phase terms θ and 3θ depending only on the rotation angle θ of the meta-atoms with the rotational axis along the incident propagation, as schematically shown in Fig. 1:2. Here, the former and latter phase terms present the case of LCP and RCP of emitted SH light, respectively. The difference of SH phase responses between the two circular polarizations indicates that for a metasurface composed of meta-atoms with the specific θ arrangement, the phase distribution and the resulting SH wavefronts are different for the two circular polarizations [89]. This fascinating spin-dependent SH emission has been implemented in nonlinear meta-hologram which shows the crosstalk-free post-selective images for the two handednesses of SH polarizations [87]. Moreover, by choosing the proper rotational symmetry for the nanoantenna such as 3-fold rotational symmetry (c_3 rotational symmetry group), it is possible to tune the nonlinear geometric Berry phase from 0 to 2π while leaving the linear phase and amplitude response essentially homogeneous along the interface [134]. With this concept, nonlinear optical encryptions have been realized in which the hidden coding images can only be read out by SHG from the nonlinear metasurfaces [135]. Furthermore, the independent manipulation between linear and nonlinear waves is highly desirable for compensating the phase mismatch induced by the chromatic dispersive effects [3, 4]. The development of novel functionalities in nonlinear metasurfaces has been proven promising for several practical applications such as holographic multiplexing [136], optical encryption [135], nonlinear plasmonic sensing [137] and quantum optical communications [138]. Besides the ability of SH wavefront shaping, the selective response of SHG depending on the handedness of the incident light has also been realized in the plasmonic metasurfaces composed of chiral nanostructures. The so-called SH circular dichroism is originated in enantiomerically sensitive plasmonic modes at the fundamental wavelength by properly arranging the planar chiral nanoantennas, resulting in a different SH near-fields and thus far-field radiations under LCP and RCP incident light [139-141].
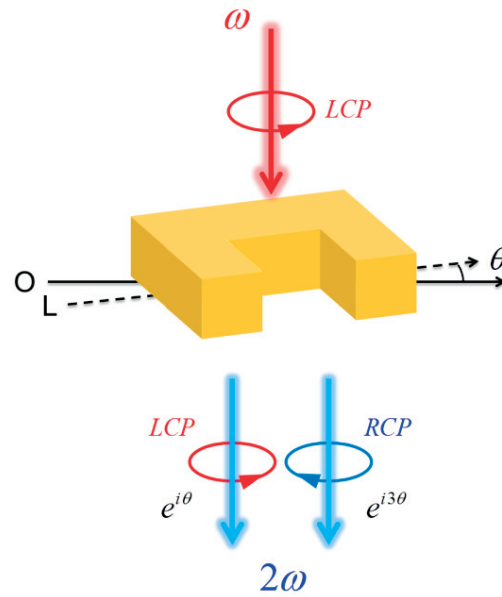
Figure 1:2 Relative nonlinear geometric phases of the SH waves (blue arrow) depending on the rotation angle θ of a one-fold rotational symmetric (C_1) meta-atom. The relative phases of the LCP and RCP SH waves are θ and 3θ under LCP fundamental excitation (red arrow), respectively. The local coordinate and laboratory coordinate are denoted as L and O, respectively. This schematic diagram is adapted from the reference [134].

1.3 Thesis objectives

This thesis has been driven by the excitement of developing new functionalities for nonlinear metasurfaces. The aim is to implement different plasmonic effects in the design of nonlinear metasurfaces in order to boost the SH enhancement and extend the possibility in the manipulation of SH emission. In the second chapter, we introduce different tools and methods used during this thesis. For the numerical tools, the physical background of the SIE method is first addressed followed by its applications to linear, SH and area-selective nonlinearity simulations. The optimized recipes of nanofabrication for both aluminum and silver nanostructures are then described. Finally, the home-built nonlinear Fourier-plane imaging setup which enables both plane-wave and Gaussian-beam illuminations, is discussed. With this Fourier-plane imaging setup, not only the intensity but also the SH emission pattern in the plasmonic metasurfaces can be recorded, which is essential for the experimental investigation of wavefront shaping with the designed nonlinear metasurfaces. Furthermore, the tunability of incident angle with the nonlinear Fourier-imaging setup permits the investigation of SH emission as a function of illumination angle. In the third chapter, we combine both simulation and experiments to explore the underlying physical mechanisms of SH enhancement in aluminum DRAs. Although the comparison of SHG between the plasmonic nanostructures with and without plasmonic resonance at the SH wavelength has been performed, the playing roles of each component in a DRA have not been fully understood yet. By tuning the resonant components around the SH wavelength, we clearly observe the enhancement of SH emission induced by the strong near-field coupling between the quadrupolar and dipolar SH modes enabled in such systems. In the fourth chapter, we implement a novel wavevector-selective nonlinearity function into an ultrathin nonlinear metasurface by using three-dimensional (3D) tilted gold nanopillars as the constituents. In general, the wavevector-selective nonlinear response has difficulty in realizing with discrete planar nanoantennas due to the required retardation effects on a LSPRs mode at the excitation stage. Here, with 3D gold nanopillars standing out from the substrate, a nonlinear mirror with the tunable wavevector-selective nonlinear response can be realized by controlling the tilted angle of the gold nanopillars. In the fifth chapter, we demonstrate a strong SH enhancement accompanied with phase-matching SH emission control in reflective phase-gradient metasurfaces composed of silver-dielectric-silver gap-plasmon meta-atoms. Especially, at the fundamental wavelength, such a system provides a sufficient in-plane momentum to tailor the incident light beam into a unique hybrid localized and propagating SPP wave supported on the silver backplate beneath the nanoantennas. The enhanced optical absorption, as well as the reduction of local symmetry for such propagating hybrid SPP mode, can lead to a 235-fold SH enhancement in the recorded SH intensity when the hybrid SPP mode is excited. Furthermore, the SH emission angle is highly restricted to a specific direction, as imposed by the quasi-phase-matching condition. To the best of our knowledge, most of the nonlinear metasurfaces are solely relying on LSPRs mode to reconstruct a desired SH wavefront. The main novelty of the proposed design is the employment of the propagating hybrid SPP mode which greatly facilitates the SH enhancement and controllable single-channel SH reflection.

2. Simulation tools, nanofabrications and experimental setups

In this thesis, we combine both simulations and experiments to design and investigate the SHG in various plasmonic systems. In order to transfer the initial ideas into final results with physical understanding, several steps including simulation tools, optimized nanofabrication and various measurement schemes are required. During my PhD, I have developed the nonlinear Fourier-plane imaging setup used for the angular-resolved measurement of SH emission from the systems studied in this thesis. In this chapter, a detailed description of the utilized tools for each step is provided before presenting the results obtained with these tools in the following chapters.

2.1 Surface integral equation (SIE) method

In this thesis, we use the SIE code developed in our laboratory to design and investigate the optical properties of plasmonic nanostructures. This method requires first the discretization of plasmonic objects' surface with triangular meshes. The size of each mesh should be around 10 times smaller than the incident wavelength for accurate near-field calculations. Also, for the SHG simulation, the mesh of the opposite two parallel facets in each domain should be identical to avoid the centrosymmetric breaking induced by the mismatch of mesh distribution as shown in Fig. 2:1. In the following, we will mainly focus on introducing the fundamental physical background by presenting the derivation of the surface integral formulation. We will provide a detailed description starting from the linear SIE, SH SIE and area-selective nonlinearity SIE methods, which have been utilized to engineer the linear and SH responses of plasmonic systems in this thesis. The schematic diagram of the process of field evaluation for each SIE method is shown in Fig. 2:2. The main advantage of SIE method is the limited number of discretizing elements, in comparison with other methods such as finite element method (FEM) and finite difference time domain (FDTD), which requires volume mesh [142, 143]. Furthermore, the triangular surface meshes provide a better approximation of complicated geometries without increasing too much the number of mesh elements required for the simulation [142, 144]. Finally, since the SH polarization is generated by the fundamental electric field very close to the surface of the plasmonic objects, SIE have been shown to be a suitable method for the accurate SHG simulation as it offers a direct evaluation of the fundamental electric field from the surface currents on the object's domains [145, 146].
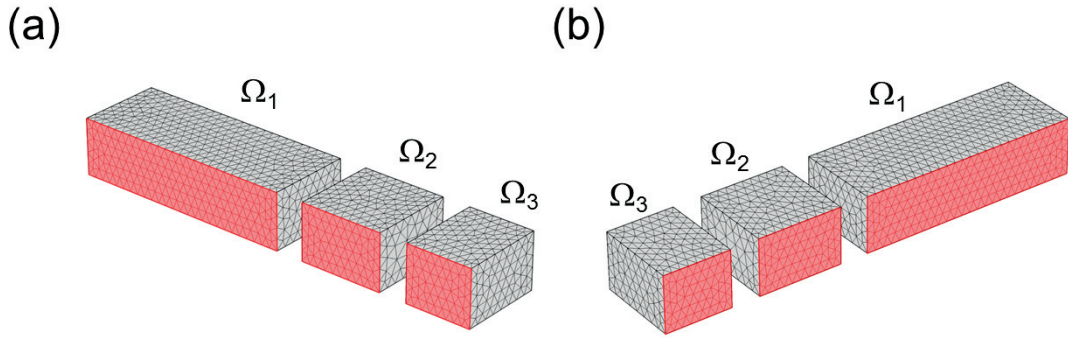
Figure 2:1 Mesh of the same DRA from different views (a) and (b) for SIE simulation, respectively. Note that the areas denoted in red have identical mesh distribution for each domain Ω_n, respectively.
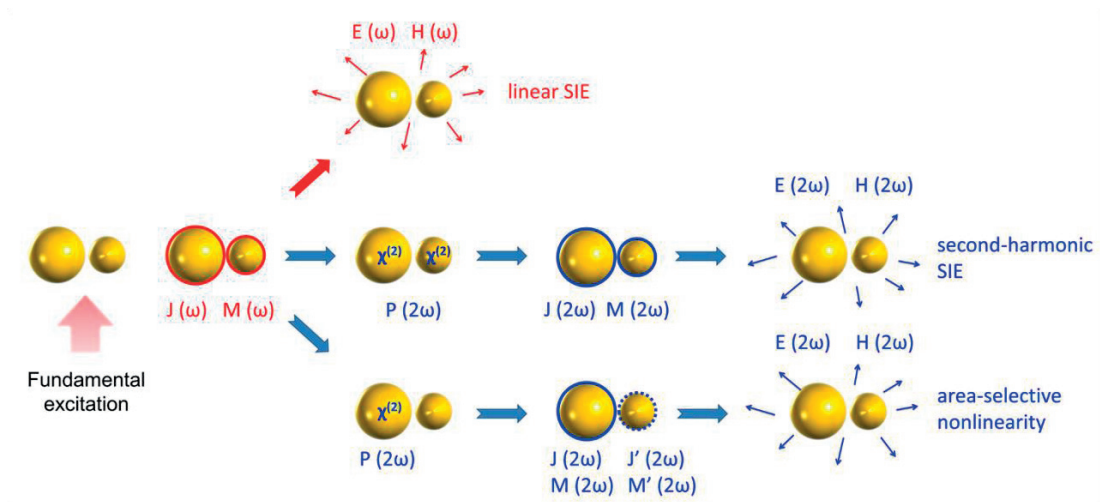
Figure 2:2 Schematic diagrams of simulation methods for the linear, SH and area-selective SH SIE. The electric surface currents, magnetic surface currents, electric field and magnetic field for fundamental/SH frequency are denoted as **J**, **M**, **E** and **H**, respectively. The SH susceptibility and polarization are presented as **J**(2ω) and **P**(2ω), respectively. And the induced SH electric and magnetic surface currents for the particle without applying $\chi^{(2)}$ are presented as **J'**(2ω) and **M'**(2ω), respectively.

2.1.1 Linear SIE and periodic SIE methods

To obtain the linear optical response of a plasmonic system with the SIE method, a homogeneous electric permittivity ε_n and a homogeneous magnetic permeability μ_n should be defined in each domain Ω_n. For a given incident wavelength range, the dispersion of the material properties should be also taken into account.

Starting from Maxwell's equations, we can formulate the wave equation for the electric field with time-harmonic dependence ($e^{i\omega t}$) as

$$\nabla \times \nabla \times \mathbf{E}_n(r) - k_n^2 \mathbf{E}_n(r) = i\omega\mu_n \mathbf{j}_n(r), \tag{2.1}$$

where $k_n = \omega\sqrt{\varepsilon_n\mu_n}$ is the wavenumber in the medium, and $\mathbf{E}_n$ and $\mathbf{j}_n$ are electric field and free current density, respectively. To solve the equation, we introduce the dyadic Green's function $\overline{\mathbf{G}}_n$ for homogeneous media [147],

$$\overline{\mathbf{G}}_n(r, r') = \left(\overline{1} + \frac{\overline{\nabla\nabla}}{k_n^2} \right) \frac{e^{ik_n|r-r'|}}{4\pi|r-r'|}, \tag{2.2}$$

and consider the dyadic Green's function to solve the equation

$$\nabla \times \nabla \times \overline{\mathbf{G}}_n(r, r') - k_n^2 \overline{\mathbf{G}}_n(r, r') = \overline{1}\,\delta(r-r'). \tag{2.3}$$

From Eq. (2.1) and Eq. (2.3), with simple derivation and integrating the obtained correlated equation over Ω_n, we can write a volume integral as

$$\int_{\Omega_n} dV \nabla \cdot \left(\left[\nabla \times \mathbf{E}_n(r) \right] \times \overline{\mathbf{G}}_n(r, r') + \mathbf{E}_n(r) \times \left[\nabla \times \overline{\mathbf{G}}_n(r, r') \right] \right)$$
$$= \mathbf{E}_n^{\text{inc}}(r') - \begin{cases} \mathbf{E}_n(r') : & r' \in \Omega_n \\ 0 : & \text{otherwise.} \end{cases} \tag{2.4}$$

Where $\mathbf{E}_n^{\text{inc}}$ is the electric field generated by the incident source upon Ω_n, which can be expressed as

$$\mathbf{E}_n^{\text{inc}}(r') = i\omega\mu_n \int_{\Omega_n} dV\, \mathbf{j}_n(r) \cdot \overline{\mathbf{G}}_n(r, r'), \tag{2.5}$$

Here, the incident electric field in the space is driven by the current density $\mathbf{j}_n$ situated at the consider position r. Now, the volume integral in Eq. (2.4) can be transformed to a surface integral using Gauss' theorem to obtain

$$\int_{\partial\Omega_n} dS\,\hat{n}_n \cdot \left(\left[\nabla \times \mathbf{E}_n(r) \right] \times \overline{\mathbf{G}}_n(r,r') + \mathbf{E}_n(r) \times \left[\nabla \times \overline{\mathbf{G}}_n(r,r') \right] \right)$$

$$= \mathbf{E}_n^{\text{inc}}(r') - \begin{cases} \mathbf{E}_n(r') : & r' \in \Omega_n \\ 0 : & \text{otherwise.} \end{cases} \tag{2.6}$$

Where $\hat{n}_n$ is the outward normal vector on the boundary $\partial\Omega_n$. Introducing the equivalent electric and magnetic surface currents,

$$\mathbf{J}_n(r) = \hat{n}_n(r) \times \mathbf{H}_n(r), \tag{2.7}$$

$$\mathbf{M}_n(r) = -\hat{n}_n(r) \times \mathbf{E}_n(r), \tag{2.8}$$

Eq. (2.6) can be written as

$$i\omega\mu_n \int_{\partial\Omega_n} dS'\,\overline{\mathbf{G}}_n(r,r') \cdot \mathbf{J}_n(r') + \int_{\partial\Omega_n} dS' \left[\nabla' \times \overline{\mathbf{G}}_n(r,r') \right] \cdot \mathbf{M}_n(r')$$

$$= \mathbf{E}_n^{\text{inc}}(r) - \begin{cases} \mathbf{E}_n(r) : & r \in \Omega_n \\ 0 : & \text{otherwise.} \end{cases} \tag{2.9}$$

Note that here we have swapped r and r' in comparison with Eq. (2.6). Now, we assume that the current density $\mathbf{j}_n$ is located outside the domain Ω_n such that the incident electric field is reaching the boundary of the domain $\partial\Omega_n$ from the outside, so $r \notin \Omega_n$. Also, with the tangential component of the fields at the boundary, we can take the limit and derived the so called electric field integral equation (EFIE) as [148]

$$\left(i\omega\mu_n \int_{\partial\Omega_n} dS'\,\overline{\mathbf{G}}_n(r,r') \cdot \mathbf{j}_n(r') + \int_{\partial\Omega_n} dS' \left[\nabla' \times \overline{\mathbf{G}}_n(r,r') \right] \cdot \mathbf{M}_n(r') \right)_{//} = \left(\mathbf{E}_n^{\text{inc}}(r) \right)_{//}. \tag{2.10}$$

With an analogous approach of derivation from the wave equation for the magnetic field, the magnetic field integral equation (MFIE) is then expressed as

$$\left(i\omega\varepsilon_n \int_{\partial\Omega_n} dS'\,\overline{\mathbf{G}}_n(r,r') \cdot \mathbf{M}_n(r') - \int_{\partial\Omega_n} dS' \left[\nabla' \times \overline{\mathbf{G}}_n(r,r') \right] \cdot \mathbf{J}_n(r') \right)_{//} = \left(\mathbf{H}_n^{\text{inc}}(r) \right)_{//}. \tag{2.11}$$

Please note that the subscript $//$ denotes the tangential boundary values of the integrals. Equations (2.10) and (2.11) provide a fundamental building block for solving the equivalent surface currents $\mathbf{J}_n$ and $\mathbf{M}_n$ on an object with arbitrary geometry excited by the given incident fields $\mathbf{E}_n^{\text{inc}}$ and $\mathbf{M}_n^{\text{inc}}$. Once the surface currents are evaluated, the electric and magnetic fields at any position can be calculated by

$$\mathbf{E}_n(r) = \mathbf{E}_n^{\text{inc}}(r) - i\omega\mu_n \int_{\partial\Omega_n} dS'\,\overline{\mathbf{G}}_n(r,r') \cdot \mathbf{J}_n(r') - \int_{\partial\Omega_n} dS' \left[\nabla' \times \overline{\mathbf{G}}_n(r,r') \right] \cdot \mathbf{M}_n(r'), \tag{2.12}$$

$$\mathbf{H}_n(r) = \mathbf{H}_n^{\text{inc}}(r) - i\omega\varepsilon_n \int\limits_{\partial\Omega_n} dS' \overline{\mathbf{G}}_n(r,r') \cdot \mathbf{H}_n(r') + \int\limits_{\partial\Omega_n} dS' \left[\nabla' \times \overline{\mathbf{G}}_n(r,r') \right] \cdot \mathbf{j}_n(r'), \quad (2.13)$$

In the case of two-dimensional (2D) periodic structures, the dyadic Green's function must satisfy the Floquet-periodic condition

$$\overline{\mathbf{G}}_{n,k}(r-\mathbf{t},r') = e^{-i\mathbf{k}\cdot\mathbf{t}} \overline{\mathbf{G}}_n(r,r'), \qquad (2.14)$$

where $\mathbf{k}$ is the Bloch wavevector in the first Brillouin zone and $\mathbf{t}$ is the lattice vector. To solving the equations for the 2D periodic structures, the dyadic $\overline{\mathbf{G}}_{n,k}(r,r')$ is the periodic Green's function

$$\overline{\mathbf{G}}_{n,k}(r-\mathbf{t},r') = \sum_{\mathbf{t}} e^{i\mathbf{k}\cdot\mathbf{t}} \overline{\mathbf{G}}_n(r-\mathbf{t},r'), \qquad (2.15)$$

Here we have described the physical background and derivation of the EFIE and MFIE, which is the basis of our SIE method. However, several numerical tools must be applied to find an approximate solution to the EFIE and MFIE. The detailed procedures for solving the EFIE and MFIE for the single and period nanostructures can be found in Ref [149] and Ref [150, 151], respectively. First, the equivalent electric and magnetic surface currents are expanded on Rao-Wilton-Glisson basis functions [152] with the discretized triangular meshes on the surface of each domain [153]. Next, the expanding coefficients are obtained by enforcing the boundary conditions on the surfaces using the Galerkin's method. A Poggio-Miller-Chang-Harrington-Wu-Tsai (PMCHWT) method is applied to ensure the accuracy of the solutions even at resonant conditions [151, 154].

2.1.2   SH SIE and area-selective nonlinearity SIE methods

As discussed in the previous chapter, the surface contributions of SHG are the dominant ones in the plasmonic nanostructures composed of centrosymmetric metals. Considering a metal/dielectric interface, the nonlinear polarization is given by

$$\mathbf{P}_\perp(r^+) \approx \chi_{\perp\perp\perp}^{(2)} : \mathbf{E}_\perp(r^-)\mathbf{E}_\perp(r^-). \qquad (2.16)$$

r^+ and r^- denote the point situated in the sheet positioned just above the metal and just beneath the interface, respectively. Therefore, the induced nonlinear polarization sheet is situated just above the metal and the fundamental electric field is estimated just below the interface [22, 155]. Here we only consider the normal component of surface nonlinear susceptibility $\chi_{\perp\perp\perp}^{(2)}$ since it has been proven to be the largest component of surface nonlinear susceptibility in plasmonic materials [58, 69, 156]. Therefore, in the Eq. (2.16), only the normal components of the electric field $\mathbf{E}_\perp(r^-)$ and the SH polarization $\mathbf{E}_\perp(r^+)$ are involved. Now, if we consider a plasmonic system composed of metallic nanoparticles embedded in a homogeneous dielectric medium, the electric field $\mathbf{E}_m(\omega)$ at the position just below the metal/dielectric interface of each nanoparticle Ω_m can be evaluated by using the surface electric current density $\mathbf{J}_m(\omega)$ and magnetic current density $\mathbf{M}_m(\omega)$ obtained with the linear SIE method as [157]

$$\nabla_{//} \cdot \mathbf{J}_m = -i\omega\varepsilon_m \hat{n}_n \cdot \mathbf{E}_m , \qquad \mathbf{M}_m = -\mathbf{E}_m \times \hat{n}_m , \qquad (2.17)$$

where m denotes the domains corresponding to the metallic nanoparticles and $\hat{n}_m$ is the normal vector pointing outward on the domain boundary $\partial\Omega_m$. Once the electric field is evaluated, the SH nonlinear polarization at the position just above the surface of nanoparticles can be evaluated following Eq. (2.16) [22, 155].

The generated SH polarization can be interpreted as a SH source standing just above the surface of metallic nanoparticles and drive the SH field following the boundary conditions for SHG [158]

$$(\Delta\mathbf{E}^{\mathrm{SH}})_{//} = \left(\mathbf{E}_d^{\mathrm{SH}}(r^+) - \mathbf{E}_m^{\mathrm{SH}}(r^+)\right)_{//} = -\frac{1}{\varepsilon'}\nabla_{//}\mathbf{P}_{\perp} , \qquad (2.18)$$

$$(\Delta\mathbf{H}^{\mathrm{SH}})_{//} = \left(\mathbf{H}_d^{\mathrm{SH}}(r^+) - \mathbf{H}_m^{\mathrm{SH}}(r^+)\right)_{//} = -2\omega\mathbf{P}\times\hat{n}_m , \qquad (2.19)$$

where d denote the dielectric side of a metal/dielectric interface. And ε' is the so-called selvedge region permittivity [68, 159]. Please note that $(\Delta\mathbf{H}^{\mathrm{SH}})_{//}$ is vanishing for $\mathbf{P}_{\perp}$. The surface integral formulation for the SH field can be derived by replacing the SH electric field $\mathbf{E}_{m,d}^{\mathrm{SH}}$ and magnetic field $\mathbf{H}_{m,d}^{\mathrm{SH}}$ in Eq. (2.18) and (2.19) with the integrands related to the equivalent SH surface densities $\mathbf{J}_{m,d}^{\mathrm{SH}}$ and $\mathbf{M}_{m,d}^{\mathrm{SH}}$:

$$\mathbf{E}_{m,d}^{\mathrm{SH}}(r) = i2\omega\mu_{m,d}\int_{\partial\Omega_{m,d}} dS' \overline{\mathbf{G}}_{m,d}^{\mathrm{SH}}(r,r') \cdot \mathbf{J}_{m,d}^{\mathrm{SH}}(r') + \int_{\partial\Omega_{m,d}} dS'\left[\nabla'\times\overline{\mathbf{G}}_{m,d}^{\mathrm{SH}}(r,r')\right]\cdot\mathbf{M}_{m,d}^{\mathrm{SH}}(r'), \ (2.20)$$

$$\mathbf{H}_{m,d}^{\mathrm{SH}}(r) = i2\omega\varepsilon_{m,d}\int_{\partial\Omega_{m,d}} dS' \overline{\mathbf{G}}_{m,d}^{\mathrm{SH}}(r,r') \cdot \mathbf{M}_{m,d}^{\mathrm{SH}}(r') - \int_{\partial\Omega_{m,d}} dS'\left[\nabla'\times\overline{\mathbf{G}}_{m,d}^{\mathrm{SH}}(r,r')\right]\cdot\mathbf{J}_{m,d}^{\mathrm{SH}}(r'), \ (2.21)$$

note that Eqs. (2.20) and (2.21) are very similar to the Eqs. (2.10) and (2.11) in the linear case. Here, the homogeneous electric permittivity $\varepsilon_{m,d}$ and homogenous magnetic permeability $\mu_{m,d}$ should apply the values at the SH frequency 2ω. The solving procedure can be simplified by considering the equality of SH surface currents standing at both sides (m and d) at a given interface. Here, in the case when only the component $\mathbf{P}_{\perp}$ is relevant, the equality $\mathbf{J}_m^{\mathrm{SH}} = -\mathbf{J}_d^{\mathrm{SH}}$ stands [68, 69]. Once the SH surface currents are evaluated, the SH electric and magnetic fields at any position can be calculated by

$$\mathbf{E}_{m,d}^{\mathrm{SH,scat}}(r) = -i2\omega\mu_{m,d}\int_{\partial\Omega_{m,d}} dS' \overline{\mathbf{G}}_{m,d}^{\mathrm{SH}}(r,r') \cdot \mathbf{J}_{m,d}^{\mathrm{SH}}(r') - \int_{\partial\Omega_{m,d}} dS'\left[\nabla'\times\overline{\mathbf{G}}_{m,d}^{\mathrm{SH}}(r,r')\right]\cdot\mathbf{M}_{m,d}^{\mathrm{SH}}(r'), \ (2.22)$$

$$\mathbf{H}_{m,d}^{\mathrm{SH,scat}}(r) = -i2\omega\varepsilon_{m,d}\int_{\partial\Omega_{m,d}} dS' \overline{\mathbf{G}}_{m,d}^{\mathrm{SH}}(r,r') \cdot \mathbf{M}_{m,d}^{\mathrm{SH}}(r') + \int_{\partial\Omega_{m,d}} dS'\left[\nabla'\times\overline{\mathbf{G}}_{m,d}^{\mathrm{SH}}(r,r')\right]\cdot\mathbf{J}_{m,d}^{\mathrm{SH}}(r'). \ (2.23)$$

Again, Eqs. (2.22) and (2.23) are very similar to the Eqs. (2.12) and (2.13) in the linear case. Contrary to the linear case, except the frequency here is double of the fundamental frequency (2ω) and the material properties should consider the values at the SH wavelength, the incident electric and magnetic field ($\mathbf{E}_n^{\mathrm{inc}}$ and $\mathbf{M}_n^{\mathrm{inc}}$) are not presented here as well. This can be understood by considering the fact that SH emission is originated from the SH surface currents $\mathbf{J}_{m,d}^{\mathrm{SH}}$ and $\mathbf{M}_{m,d}^{\mathrm{SH}}$ on the metallic objects as a nonlinear optical process, and the frequency of emitted field is twice of that of incident electric field.

In the case of a 2D periodic nanostructure array, the nonlinear polarization must satisfy the Floquet-periodic condition [160]:

$$\overline{\mathbf{P}}_\perp(r^+ - \mathbf{t}) = e^{-i\mathbf{K}\cdot\mathbf{t}}\overline{\mathbf{P}}_\perp(r^+), \tag{2.24}$$

where $\mathbf{K} = 2\mathbf{k}$ is the Bloch vector associated to the SH waves and $\mathbf{k}$ is the linear Bloch vector mentioned. The detailed procedure of SIE simulation for SHG can be found in Ref [161].

In order to investigate the SHG contributions from different metallic domains in coupled plasmonic systems, area-selective nonlinearity SIE method has been developed. This method permits to consider a non-zero nonlinear susceptibility $\chi_{\perp\perp\perp}^{(2)}$ only on the surface of the chosen metallic domains in a multi-domain coupled plasmonic system without removing the near-field coupling effect at the excitation and emission stages. In other words, although the nonlinear polarization is vanishing in the metallic domains with zero $\chi_{\perp\perp\perp}^{(2)}$ according to Eq. (2.17), it can still be polarized by the SH field generated by the other constitutive parts of the coupled plasmonic system with non-zero $\chi_{\perp\perp\perp}^{(2)}$, as schematically depicted in Fig. 2:2. As in the case of linear and SH SIE methods, once the equivalent SH surface currents are evaluated, the SH electric field and magnetic field at any position can be calculated by the Eqs. (2.22) and (2.23). The detailed information of area-selective nonlinearity SIE method can be found in Ref [162].

21

2.1.3 Fourier transform method

In this thesis, discrete Fourier transform (DFT) has been performed to analyze the radiation pattern from a 2D plasmonic array under plane-wave illumination. This method requires first evaluating the electric and magnetic field in a plane with an area defined by the unit cell of plasmonic array and positioned in the far-field region (e.g. 10 μm away from the structure plane). The electric field in this plane evaluated with the SIE simulation can be considered as a linear combination of the electric fields of different diffraction orders supported by the plasmonic array. For each $i\,th$ diffraction order, one can discribe the electric field distribution in this plane as $e^{i\mathbf{k}_i \cdot r}$ associated with the wavevector $\mathbf{k}_i$. Therefore, the DFT method is achieved by expanding the evaluated electric field $\mathbf{E}(r)$ on the field distributions corresponding to various diffraction orders and expressing in a Fourier series as:

$$\mathbf{E}(r) = \sum_{i=0}^{n} \mathbf{E}_i \cdot e^{i\mathbf{k}_i \cdot r}. \tag{2.25}$$

The amplitude coefficient of each diffraction order $\mathbf{E}_i$ can be analyzed via the discrete Fourier transform of $\mathbf{E}(r)$. In other words, the evaluated field with a complex spatial distribution in this plane can be decomposed into that from different diffraction orders sustained in the considered array. Please note that the existing wavevectors are determined by the lattice constants of plasmonic array following the grating equation. For example, if we consider a plasmonic array with the periodicity L along the x direction, the in-plane wavevectors of diffraction channels at normal incidence (along $+z$ direction) are given by:

$$\mathbf{k}_{i,x} = i \cdot \frac{2\pi}{L}, \tag{2.26}$$

One can easily find the diffraction angle since the in-plane wavevector is related to the wavevector k_0 in the medium as:

$$\mathbf{k}_{i,x} = k_0 \sin\theta_i, \tag{2.27}$$

and θ_i is the diffraction angle corresponding to the $i\,th$ diffraction order.

The main idea of DFT method is to sort out the contribution of the different diffraction orders by expressing the evaluated electric field into a Fourier series composed of spatial functions determined by the periodicity. Figure 2:3 gives an example of transforming an electric field distribution in the real space to the corresponding Fourier-space distribution with the DFT method. Here, we present the emission pattern of SHG from a plasmonic gold nanorod (with nanorod length 90 nm) array (with periodicity $L_x = L_y = 246.6$ nm) under 720-nm illumination at normal incidence. In this case, the whole system is embedded in a homogeneous medium with refractive index $n = 1.5$.
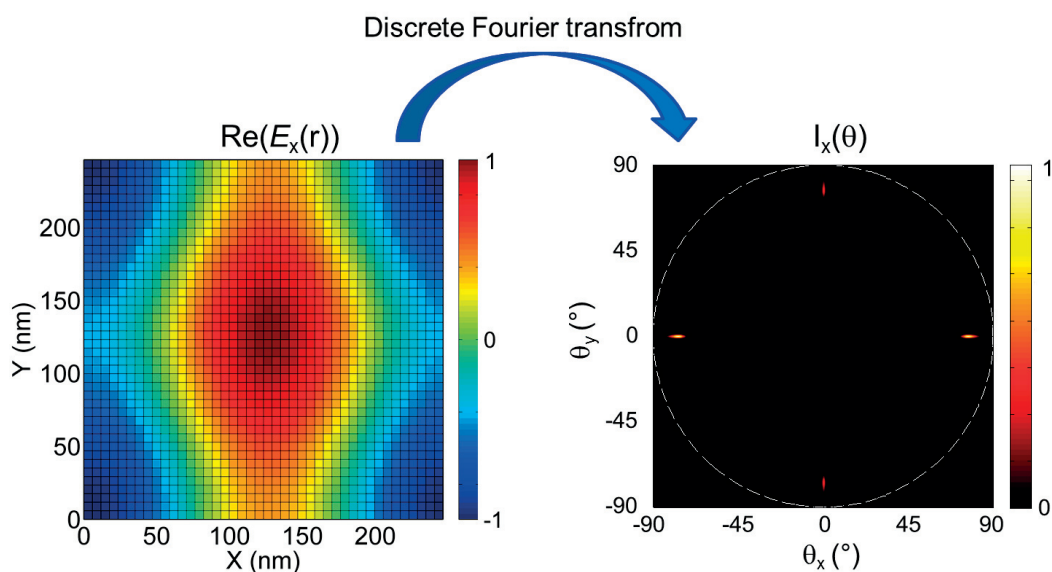
Discrete Fourier transfrom

Figure 2:3 Applying the discrete Fourier transformation to transform an evaluated electric field distribution in (a) real space to the (b) corresponding Fourier space.

2.2 Nanofabrication of plasmonic structures

In our laboratory, nanofabrications with several plasmonic materials have been optimized to realize nanostructures with well-defined geometries. This is essential especially for the SH emission, which has a high sensitivity to the surface morphology of plasmonic nanostructures [163, 164]. For the fabrication of aluminum nanostructures, it has been observed that the residual gases, especially H_2O and O_2 have a strong dissociative absorption leading to the formation of the oxide-hydroxide phase of aluminum and thus modifying the surface morphology of aluminum nanostructures [56, 165]. Therefore, H_2O present in the glass substrate, spin-coated photoresist, and the evaporation environment should be eliminated. Thus, the optimized recipe of aluminum nanostructures is developed and processed in the following: First, the water from glass substrate is removed by baking 24 hours at 120°C. Following, two PMMA layers with different weights are spin coated on the glass substrate in order to generate undercut and facilitate the lift-off. To minimize the water inside the coated photoresists, the sample is baked 10 hours at 80°C with periodic introduction of nitrogen. The conductive layer to prevent the charging effect during e-beam writing is the thermal evaporated 20-nm Cr layer on top of PMMA (Leybold-Optics LAB600 H). Afterward, we process e-beam writing directly with a 100 keV electron gun (Vistec EBPG5000), and the optimized dose is 800 µC/cm². After exposure, the Cr wet etching and the PMMA develop are done frequently. To minimize the water during the above processes, the sample is again baked for 10 hours at 80°C with periodic introduction of nitrogen. Next, the sample is immediately placed in the thermal evaporator (Leybold-Optics LAB600 H) and initially coated with 1-nm silver oxide as the adhesion layer. After initial evaporation, the chamber is pumped out for 9 hours before conducting the aluminum evaporation, to ensure that the water inside the chamber is nearly completely removed. Thereafter, 40 nm of aluminum is evaporated

23

at 0.1 Å/s. Finally, the sample is carefully lift-off with acetone solution, followed by the IPA cleaning and nitrogen drying. The whole fabrication process of aluminum nanostructures is schematically exhibited in Fig. 2:4. Figure 2:5 shows the SEM images of fabricated aluminum nanoantennas revealing high-quality nanostructures.
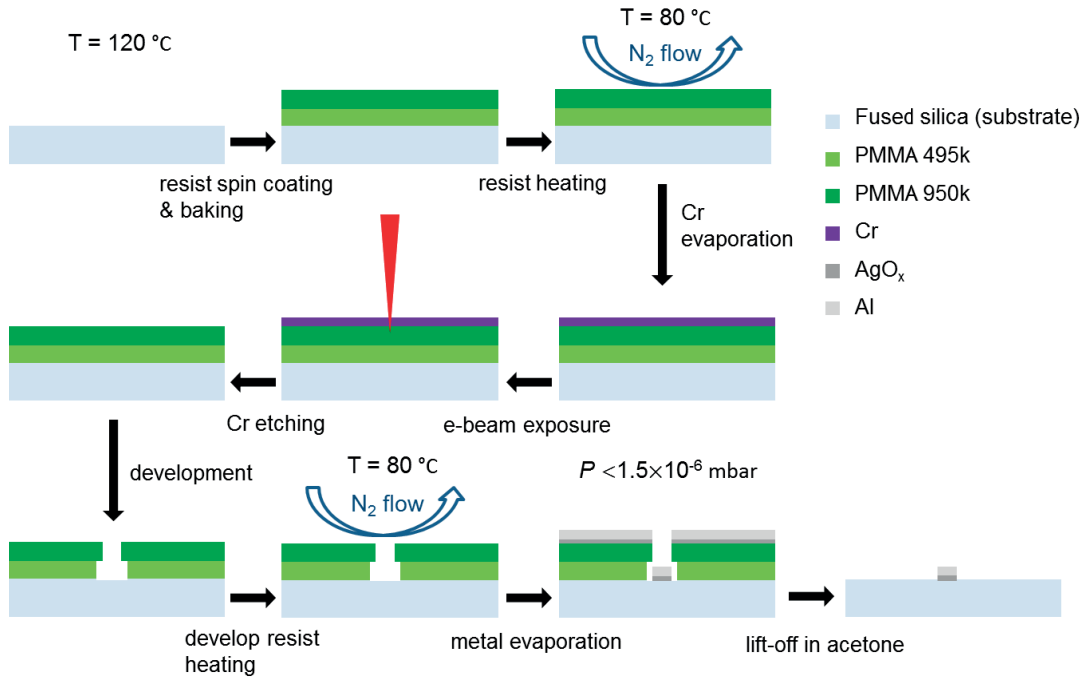
Figure 2:4 Process flow for the fabrication of the aluminum nanostructures.
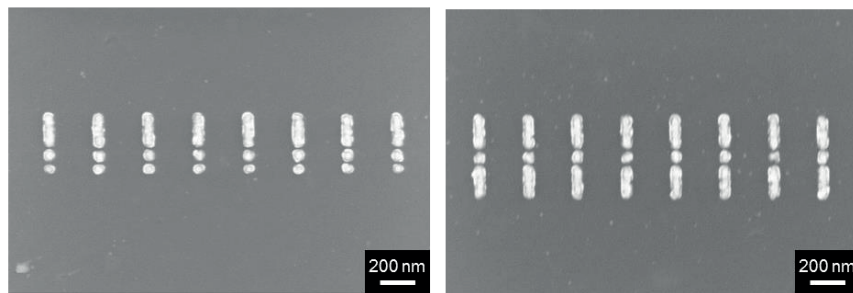
Figure 2:5 SEM images of the fabricated aluminum nanoantennas.

For the fabrication of the reflective silver-dielectric-silver metasurfaces, a float glass substrate was first prepared by depositing a 1 nm silver oxide adhesion layer and 200 nm-thick silver backplane followed by a 30 nm-thick SiO_2 spacer within a single thermal evaporation run at a rate of 4 Å/s to ensure a uniform thin film surface (Leybold-Optics LAB600 H). Silver nanostructures were then fabricated on top of the SiO_2 spacer using the electron beam lithography method mentioned previously. In brief, a double-layer PMMA photoresist with a 20-nm Cr conducting layer was exposed via electron beam lithography (Vistec EBPG5000 system) using a 100 keV and 200 pA electron beam. The nanostructures were obtained through the development of the exposed resist, thermal evaporation of a 1 nm silver oxide adhesion layer and 39 nm of Ag followed by a lift-off process. The whole fabrication process of the reflective silver-dielectric-silver metasurfaces is schematically presented in Fig. 2:6. Figure 2:7 shows the SEM images of fabricated reflective silver metasurfaces revealing high-quality nanostructures. Two different types of reflective metasurfaces have been fabricated during this thesis. They are made of different kinds of constituted meta-atoms, either silver nanorods or dolmen nanostructures.
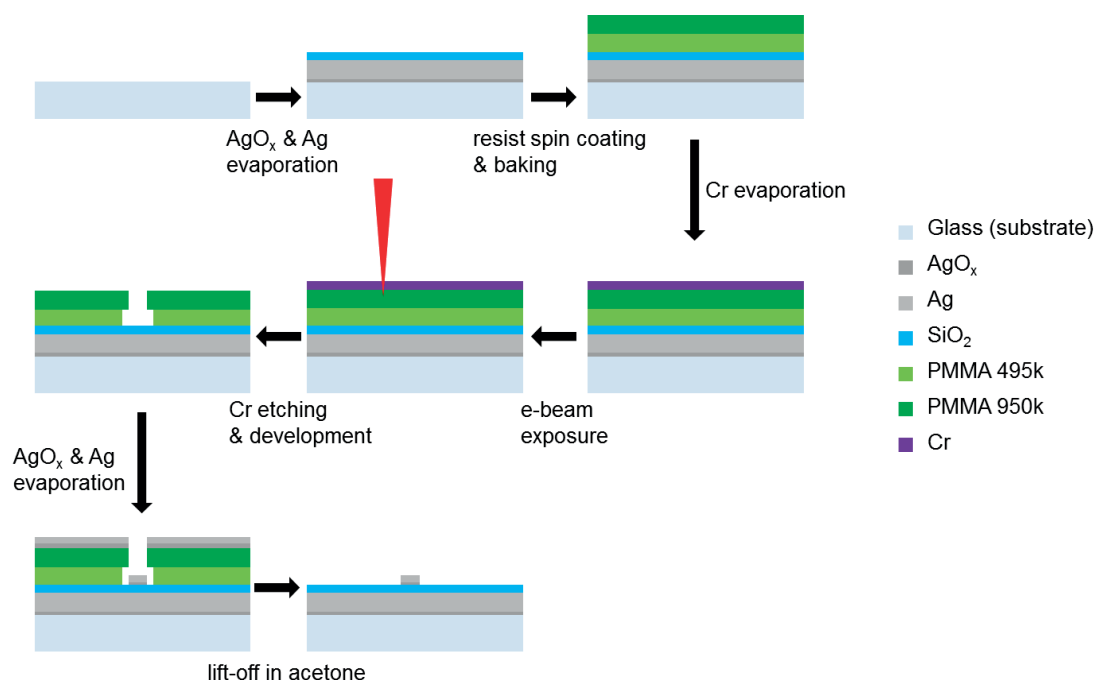
Figure 2:6 Process flow for the fabrication of the reflective metasurfaces with silver nanostructures and silver mirror spaced by a SiO_2 spacer.
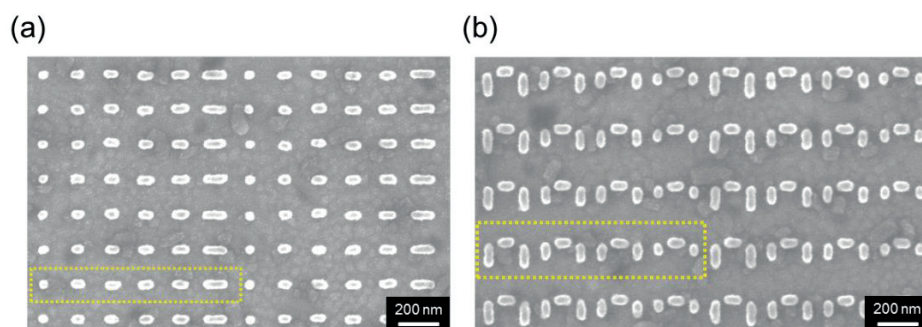
Figure 2:7 SEM images of the fabricated reflective phase-gradient metasurfaces with silver nanostructures and silver mirror spaced by a 30-nm SiO_2 spacer. The yellow dashed box depicts the supercell of the metasurface constituted by geometric varied (a) nanorods and (b) Dolmen meta-atoms, respectively.

2.3 Multiphoton confocal scanning microscope

In this thesis, we used various measurement configurations to record the images/radiation patterns of SHG from the studied plasmonic systems. For the SHG images measurements, we use a multi-photon scanning microscopy (LEICA SP5 MULTI-PHOTON) combined with a 20x/1.00 water-immersion objective (HCX PL APO), and a Ti:Sapphire femtosecond laser (Chameleon ultra laser with a 80 MHz repetition rate) operating at 800 nm with a 140 fs pulse duration combined with an electro-optical modulator (EOM) to adjust the input power. The backward scattered SHG from the structures is collected by the same objective followed by a beam splitter, a band-pass filter (400/15 BrightLine® fluorescence filter) and a non-descanned (external) detector photomultiplier tube (NDD PMT) to increase the amount of SH emission collected. The XY resonance scanner (400 Hz scanning speed) of the microscopy enables a 387.5 μm $\times$ 387.5 μm field range with 758.32 nm pixel resolution. Figure 2:8 shows the setup configuration of the multi-photon scanning microscope used for recording SHG images.
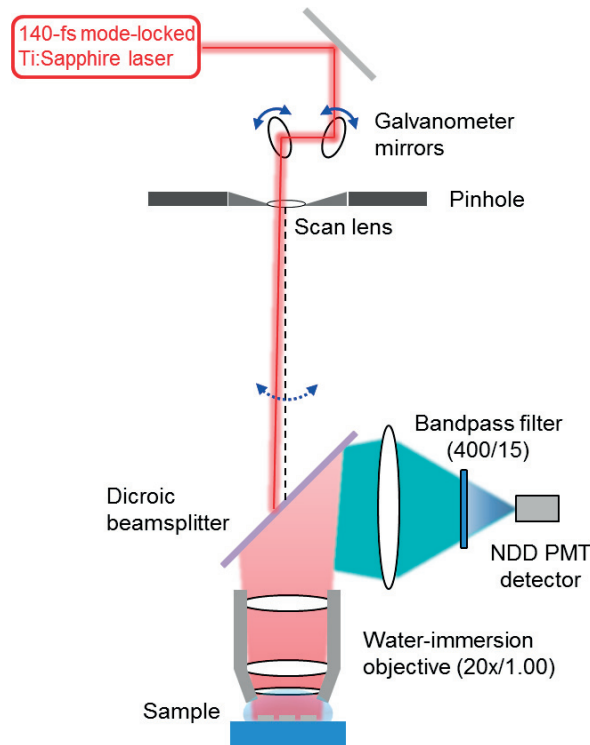
Figure 2:8 The experimental setup for the nonlinear optical measurements corresponds to a multi-photon scanning microscope with galvanometer resonant mirrors (400 Hz scanning speed), scan lens and 20x/NA 1.00 water-immersion objective, which enable a 387.5 μm × 387.5 μm scanning field with a 758.32 nm pixel resolution for a Ti:Sapphire 140-fs laser working at 800 nm. The backward SH scattering is collected with the same objective, a dichroic beam splitter (reflecting the wavelength below 700 nm), a collection lens, a bandpass filter (400/15 nm) and a photomultiplier tube (NDD PMT).

2.4 Angular-resolved setup with Fourier-plane imaging method

2.4.1 Plane-wave illumination

I have implemented an angular-resolved nonlinear setup based on Fourier imaging method incorporated with a tunable plane-wave illumination scheme. The plane-wave illumination is realized by focusing a Ti-Sapphire pumped laser beam (Coherent Mira 900, 80 MHz, 180 fs, 800 nm, average power 10 mW) on the back focal plane (BFP) of a 60× oil-immersion objective (NA 1.45) with a focusing lens L_0 (focus length f = 28 cm), leading to a spot size of ~20 μm on the sample. Please note that the advantage of this configuration is that the incident angle can be controlled by moving the laser spot in the BFP of objective with two mirrors mounted on translation stages. The nonlinear radiation patterns of our reflective sample are acquired by recording the BFP images collected with the same objective. For the measurement of SH radiation, in order to eliminate the near-infrared excitation and record the BFP images on a back-illuminated camera (iDus 420), a longpass dichroic mirror (DMLP550R), a tube lens L_1 (focus length f = 18 cm), an imaging lens L_2 (focus length f = 5 cm) and a set of 3 narrow bandpass filters (BP, 400/20 nm) transmits only the SH at 400 nm are placed in front of the spectrograph (Andor SR303i-B), as

shown in Fig. 2:9(a). The blazed grating (300 l/mm) inside the spectrograph is also used to further remove the possible background and excitation light by dispersing different wavelengths into the horizontal direction of the camera pixels (1024 pixels). In this case, we can select the signal corresponding to the SH wavelength along the horizontal pixels, and the intensity distribution along the vertical direction of camera pixels (255 pixels) provides the angular distribution of SH emission. Figure 2:9(b) presents the recorded SH intensity as a function of both illumination angle and SH emission angle for a symmetric three-dimensional (3D) gold nanopillars sample. Besides, in order to bring the sample into focus and align its position with the laser illumination, a dark-field illumination system (with a halogen lamp) was implemented, which enables the imaging of sample and laser-illuminated spot simultaneously by a charge-coupled camera installed at the imaging plane of tube lens L_1.

Figure 2:9(a) Schematic diagram of the Fourier-plane imaging setup for SH emission with plane-wave illuminations. (b) Measured SH emission as a function of the angle of illumination from a symmetric gold nanopillars sample with the base diameter 100 nm and height 130 nm. The SEM image of the sample is shown in the top panel. The scale bar corresponds to 500 nm.

2.4.2 Gaussian-beam illumination

Although the tunable plane-wave illumination scheme is favorable for the investigation of the SH radiation as a function of incident angle, scanning the incident angle to achieve a most efficient SHG could be sometimes time-consuming especially when very precise incident angles are required (e.g. a plasmonic thin film supporting SPPs). In contrast, for a given excitation wavelength, a Gaussian-beam illumination scheme simultaneously provides a broad range of incident wavevectors depending on the NA of microscope objective. This can be done by introducing a laser beam expander consisted of a lens L_{01} (focus length f = 5 cm), a 100-μm pinhole and a lens L_{02} (focus length f = 10 cm) to fulfill the whole back aperture of the microscope objective with an expanded laser beam as shown in Fig. 2:9. In this case, the size of laser-illuminated spot on the sample is reduced to only a few micrometers. With this approach, the wavevector-selective plasmonic mode can still be resonantly excited by a Gaussian focused beam providing

a broad range of incident wavevectors. Therefore, the excitation of the plasmonic mode in the linear regime results in an efficient SH emission, which is favorable for recording the SH signal without repeatedly tuning and optimizing the illumination angle [166]. Please note that in this case, the grating inside the spectrograph is replaced by a mirror to provide the angular-resolved information of SH emission along both horizontal rows and vertical columns of camera pixels. Figure 2:10(b) presents the recorded SH radiation pattern of a 200-nm silver film under y-polarized Gaussian-beam illumination. The photograph exhibits different parts of the Fourier-plane imaging setup is presented in Fig. 2:11.
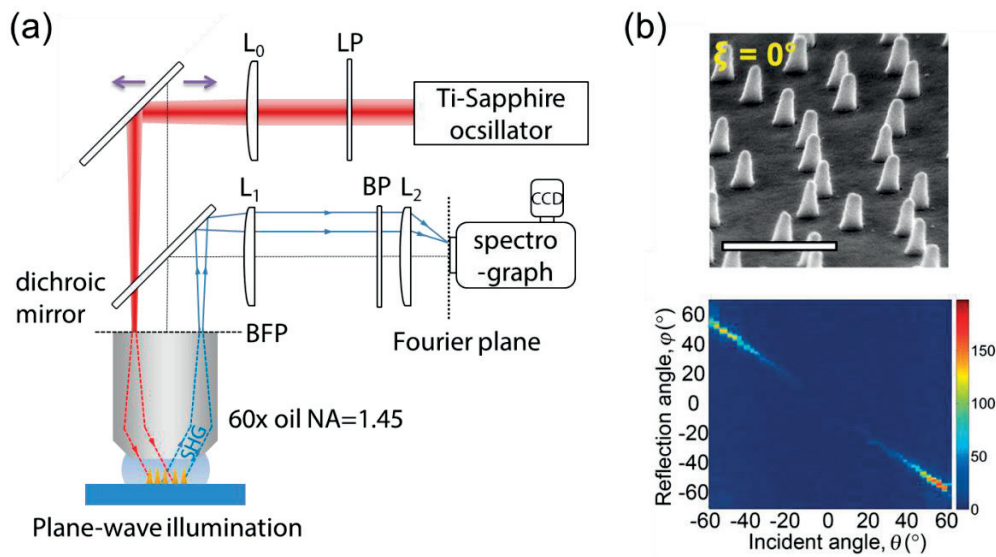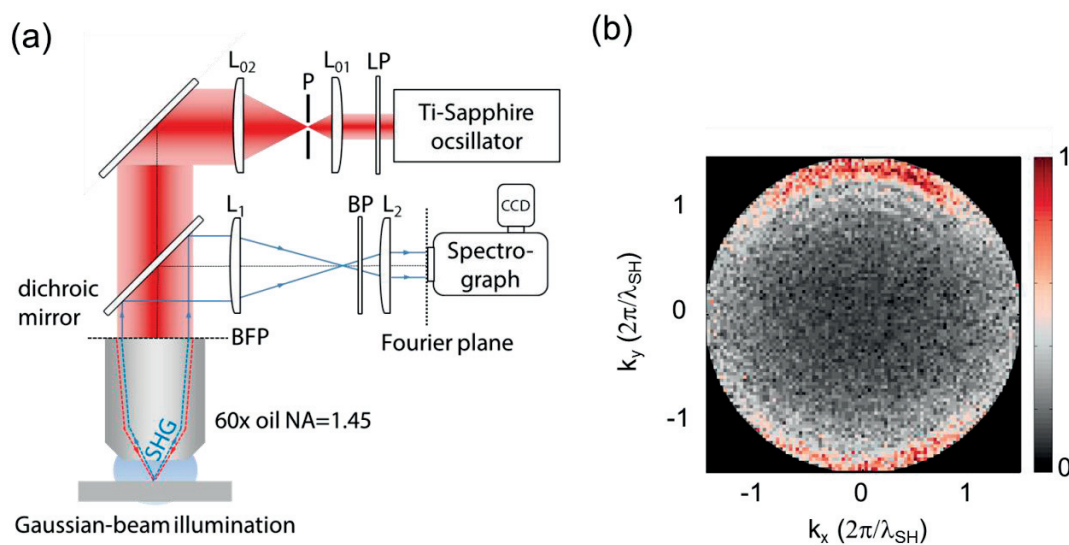

Figure 2:10 (a) Schematic diagram of the Fourier-plane imaging setup for SH emission with a Gaussian-beam illumination. (b) Measured SH emission from a silver mirror with y-polarized Gaussian-beam illumination.
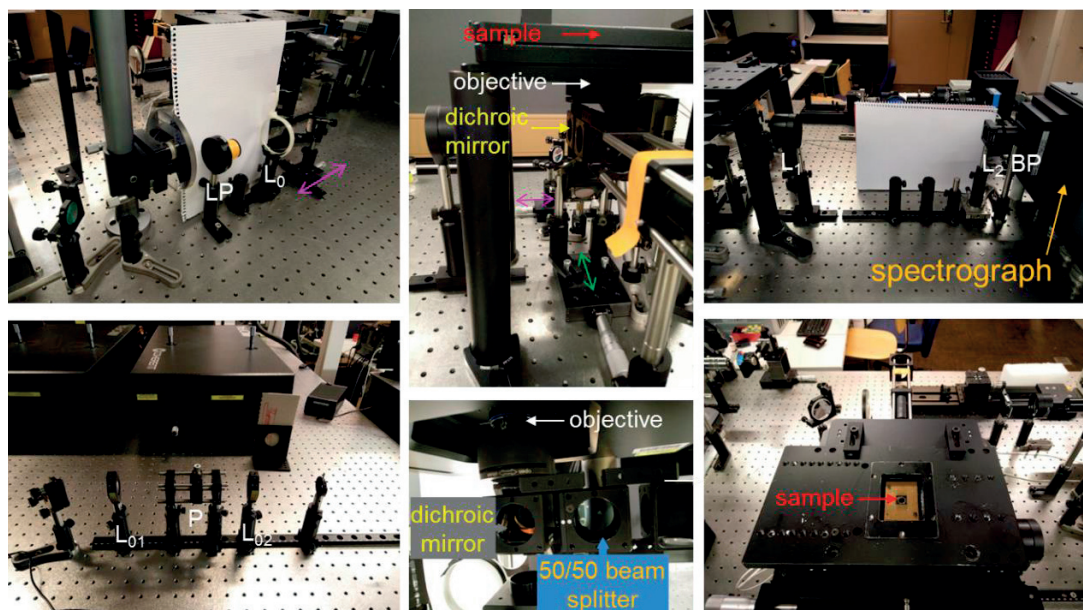
Figure 2:11 Photographs showing different parts of the nonlinear Fourier-plane imaging setup.

For a Gaussian-beam illumination, the intensity profile of the expanded laser beam in the BFP of objective is associated with the intensity contribution for various incident wavevectors in the focused laser beam. To obtain the intensity profile of the illumination, the reflection of a 200-nm silver film in the Fourier plane was measured as shown in Fig. 2:12(a). Note that the SH band-pass filters set is removed during the measurement. The recorded intensity profile is then fitted with a Gaussian distribution and the obtained fitting profile in the Fourier plane is presented in Fig. 2:12(b). Now, the Gaussian fitting of recorded intensity distribution in the Fourier plane is associated with the intensity distribution of various incident wavevectors provided by the 800-nm Gaussian-beam illumination. Therefore, due to the quadratic power dependence of SHG, the intensity squared profile of the Gaussian fitting should be considered in the normalization of the recorded SH radiation pattern as shown in Fig. 2:10(b). Figure 2:12(c) exhibits the intensity squared profile of Gaussian fitting in the Fourier plane.
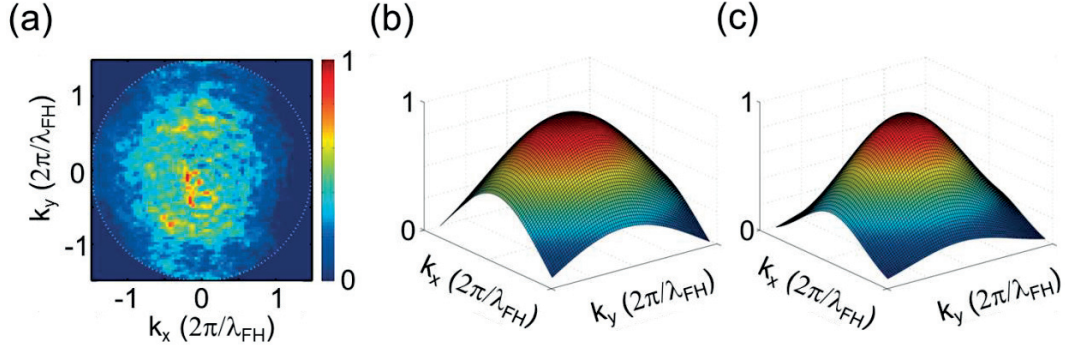
Figure 2:12 Intensity profile fitting of the Fourier-plane image corresponding to the reflection of a 200-nm silver mirror with 800-nm Gaussian-beam illumination. (a) The recorded intensity distribution, (b) the Gaussian fitting of recorded intensity distribution and (c) the intensity squared profile of the Gaussian fitting for the reflection of a 200-nm silver mirror.

The measurement of the linear spectrum is performed with another Fourier-imaging microscopic setup developed in our laboratory [167]. The tuning of the incident angle is achieved by scanning the laser spot in the BFP of microscopic objective as in the nonlinear Fourier-imaging setup. However, instead of Ti-Sapphire oscillator, the linear optical setup utilizes a supercontinuum light source (Fianium FemtoPower 1060) combined with an 8-channel acousto-optical tunable filter (AOTF) in order to control the incident wavelength from visible to near-infrared region. Therefore, the linear spectrum as a function of incident angle can be measured and analyzed. Also, the dichroic mirror is replaced by a 50/50 beam splitter and also the set of bandpass filters in front of spectrograph is removed.

2.5 Summary

In this chapter, all the tools utilized to lead to the results in this thesis are described in detail. The simulations of both linear and SH responses in a plasmonic system are performed by the linear and SH SIE methods developed in our laboratory, respectively. This method is based on the surface integral equation of Maxwell's equations to solve the equivalent surface currents of plasmonic objects in the presence of excitation source. In the case of linear SIE method, the incident electric field generated by the current density located at the considered position is the excitation source of surface currents. By considering the excitation source as well as a homogeneous electric permittivity and magnetic permeability in each domain of a plasmonic object, we can evaluate the surface currents by solving the SIE equations with the introduced Green's function. Once the surface currents are evaluated, the SH polarization standing at the surface of metallic domains can be calculated by considering the normal component of surface nonlinear susceptibility $\chi^{(2)}_{\perp\perp\perp}$. Please note that in this case, the SH polarization acts as an excitation source to locally driven SH surface currents on a plasmonic object. Indeed, the non-vanishing SH polarization at the metal/dielectric interface can induce the SH surface currents following the boundary conditions for SHG. After acquiring the linear/SH surface currents by solving the corresponding surface integral equations, electric and magnetic fields at any location can be computed. Furthermore, the area-selective nonlinearity method enables the possibility of applying the nonlinear

susceptibility in the chosen metallic domains, resulting in a non-zero nonlinear polarization in these domains. Noted that this method considers the near-field coupling between constitutive elements of a coupled plasmonic system for both the linear and SH responses. Therefore, the SH surface currents can still be polarized on the domains with zero nonlinear susceptibility, permitting the study of SH mode coupling in a coupled plasmonic nanoantenna. The discrete Fourier transform has been shown as a useful method to analyze the radiation pattern of 2D plasmonic arrays from the evaluated electric field distribution in the far-field. For the fabrication of plasmonic nanostructures, the optimized recipes for the fabrication of aluminum and silver nanostructures with well-defined morphologies are introduced, which is essentially, especially for SHG. Finally, the SH images and the corresponding radiation patterns from plasmonic nanostructures can be recorded with a multiphoton scanning microscope and a homebuilt nonlinear Fourier-imaging setup, respectively. I have implemented the nonlinear Fourier-plane imaging setup which can be worked with both plane-wave and focused-beam illuminations during my PhD. The plane-wave illumination is realized by focusing the excitation laser beam on the back focal plane of the microscopic objective, and the illumination angle can be tuned by moving the focused laser spot in the back focal plane. By incorporating with the nonlinear Fourier-plane imaging method to record SH reflection with the same objective for illumination, this scheme allows one to study the SH emission as a function of illumination angle. In contrast, Gaussian-beam illumination is acquired by expanding the laser beam to fulfill the whole aperture of microscopic objective, providing a broad range of incident wavevectors simultaneously depending on the NA of microscope objective. The Gaussian-beam illumination scheme is useful for characterizing the SH radiation pattern from the wavevector-selective plasmonic systems.

3. Mechanism of SH enhancement in double-resonant antennas

Multiresonant plasmonic nanoantennas have recently gained a lot of attention due to their ability to enhance nonlinear optical processes at the nanoscale [168-175]. For SHG in multiresonant plasmonic nanoantennas, the nonlinear polarization is mainly induced on the surface of plasmonic components possessing a strong dipolar resonance with enhanced near-field at the fundamental wavelength. However, due to the symmetry, the SH modes induced over the plasmonic components usually is corresponding to a high-order SH mode, resulting in an inefficient SH emission [70]. By implementing an additional plasmonic dipolar mode at the SH wavelength such that it can be efficiently excited by the SH near-field generated by the fundamental dipolar mode, the enhancement of SH emission has been clearly demonstrated in multiresonant plasmonic nanoantennas with geometries including, for example, a V-shaped nanoantenna and a single nanorod [64], a nanorod and small nanodiscs [175], Fano-resonant plasmonic heptamers [171] and multiresonant log-period optical antennas [63]. The first nanostructure designed for this purpose was the aluminum DRAs [169]. It was demonstrated that SHG resulting from its resonances at both the fundamental and SH wavelengths is higher than the one from a simple dipolar nanoantenna (DA) supporting a resonance at the fundamental wavelength only [169]. However, the underlying mechanisms leading to a strong nonlinear signal in multiresonant plasmonic nanostructures are still unknown. In this chapter, we combine both simulations and experiments in order to investigate in details the role of the mode coupling in the enhancement of SHG. By varying the length of the aluminum DRAs, it is clearly demonstrated that the maximum enhancement of SHG is reached when the coupling between the quadrupolar and the dipolar modes is the strongest. Indeed, using the developed area-selective nonlinearity SIE method, it is shown that the SH quadrupolar mode, which is *directly* excited by the fundamental pump [51, 176], can resonantly transfer its energy to the SH dipolar mode supported by another part of the DRA. This resonant energy transfer results from the symmetry breaking in the DRA and the near-field coupling at the SH wavelength. In comparison, the SH quadrupole-quadrupole mode coupling is found to generate a small SH signal despite a higher fundamental near-field enhancement. The study of the SHG mechanisms of double resonant plasmonic systems is important for the design of efficient SH meta-devices such as coherent extreme-ultraviolet (EUV) source, ultra-sensitive index and chiral plasmonic sensors [141, 177-184]. Parts of this chapter have been published in Ref. [185]. In this study, I have done the nanofabrication, nonlinear measurements, as well as the linear and SH SIE simulations of the aluminum DRAs. The multipolar analysis of the SH emission were made by G.D. Bernasconi from the NAM-EPFL.

3.1 Introduction

So far, most of the previous research works focus on the SHG with a single engineered plasmonic resonance at either the fundamental or SH wavelength. In both cases, it was clearly shown that the SHG can be enhanced by an order of magnitude in comparison with off-resonance excitation and emission [51, 52, 61]. In general, the SH radiation pattern from the plasmonic nanoparticles is similar to that of a quadrupole or a dipole [51]. To further improve the SHG, the plasmonic nanostructures supporting resonances at both the fundamental and SH wavelengths have been recently designed in various novel nanostructures such as DRA supporting plasmonic *bright* modes at both wavelengths [83, 169] and plasmonic Fano structures with a plasmonic *dark* mode at fundamental wavelength and a *bright* mode at SH wavelength [171, 186]. Interestingly, for the DRA, even though the fundamental near-field intensity is lower than that of the DA resonating only at the fundamental wavelength, the SH scattering intensity is still enhanced by several times [83]. Yet, the physical mechanisms leading to the enhancement of SHG in these nanostructures are still unknown but are an essential basis for the design of efficient SHG plasmonic devices.

In this chapter, we use a SIE method [149, 187] and nonlinear optical experiments to study the SHG mechanism in DRAs by detuning the resonance close to the SH wavelength while the fundamental resonance is fixed. The enhancement of SHG in the double-resonance plasmonic nanostructures can be simply understood by the near-field coupling between SH non-radiative mode, directly driven by fundamental excitation, and SH radiative mode, as schematically illustrated in Fig. 3:1(a). In the case of DRA supporting both fundamental and SH resonances, a fundamental dipolar mode is excited on the long bar of DRA under illumination, which generates a SH quadrupolar mode with an inefficient radiation of the SH signal to the far-field (indicated by the blue dashed arrow). However, when a short bar supporting a dipolar mode at the SH wavelength is placed in proximity, the non-radiative SH quadrupolar mode can transfer its energy to the SH dipolar mode in the near-field, opening a new radiative channel (indicated by the blue arrow). This energy transfer between different parts of DRAs is confirmed with an area-selected SH nonlinearity method. As the resonance close to the SH wavelength is gradually tuned by changing geometry parameters, the variation of the SH signal is analyzed revealing the relationship between the near-field and far-field responses (schematic diagram in Fig. 3:1(b)). The DRAs samples are fabricated with aluminum following a recipe permitting to reduce the defects caused by oxidation as discussed in section 2.2. These theoretical predictions are confirmed by experimental results which are in excellent agreement with the numerical results.
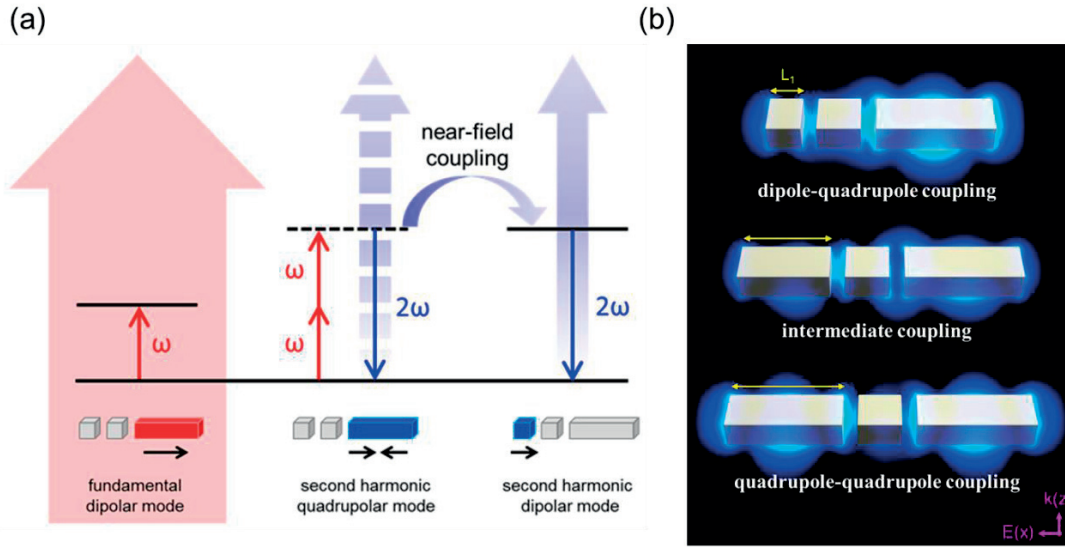
Figure 3:1 (a) Mechanisms of the SHG enhancement in DRA with both fundamental (long bar) and SH (short bar) resonances. The fundamental excitation, the direct SH quadrupolar emission (long bar) and SH dipolar mode (short bar) are depicted as a red arrow, a blue dashed arrow and a blue arrow, respectively. Note that the near-field coupling occurs when the short bar supports a dipolar mode at the SH wavelength. (b) Calculated 3-dimensional SH near-field distributions for three different aluminum DRAs with short bar length $L_1 = 47$ nm, 123.5 nm and 157.5 nm (from top to bottom) corresponding to different coupling regimes. The DRAs are driven by a planewave ($\lambda = 800$ nm) propagating along the z-axis and polarized along x-axis (along the antenna arms). The thickness and width of the DRAs are 40 and 60 nm, respectively. The lengths of middle bar and long bar of DRAs are optimized and fixed at 60 and 160 nm, respectively. The refractive index of the surrounding medium is n = 1.45.

3.2 Simulation

3.2.1 Excited plasmonic mode at linear and SH wavelength

The DRAs studied in this work consist of three aluminum nanorods aligned along the x-axis separated with 20 nm gaps. The small gap dimension facilitates a strong near-field coupling in both the linear and SHG regimes. Other geometric parameters, namely the width and thickness of the DRAs, are set to 60 nm and 40 nm, respectively (Figure 3:1(b)). The simulations were performed considering isolated structures in a homogenous background with a refractive index n = 1.45, corresponding to the averaged value between the refractive index of water and of the glass substrate. In order to design the DRAs with plasmonic resonances at both fundamental excitation (800 nm) and the corresponding SH wavelength (400 nm), the length L_2 of long rod a is first optimized using the linear SIE simulation. Figure 3:2(a) shows the scattered intensity as a function of the length L_2 for an incoming planewave with a wavelength $\lambda = 800$ nm. The incident planewave comes at normal incidence and is polarized along the antenna arms. Please, note that the lengths of the two short rods are fixed to 60 nm and that the two short bars are off-resonant parts of the system for the moment. A maximum of the scattered intensity is observed when the length L_2 is about 160 nm corresponding to a strong resonant excitation at the fundamental wavelength (800 nm). In a second step, the length L_2 is fixed at 160 nm in order to gener-

ate the maximum fundamental near-field intensity close to the long bar a and only the length L_1 of short bar c is changed for tuning the second resonance close to the SH wavelength (400 nm). Figure 3:2(b) presents the scattering intensity for different lengths L_1 ranging from 20 nm to 200 nm. The blue and red curves represent the variation of the scattering intensity with the length L_1 for a planewave excitation with a wavelength $\lambda = 800$ nm and 400 nm, respectively. The red curve clearly indicates that a maximum enhancement at 400 nm can be yielded for length L_1 close to 70 nm. On the other hand, the blue curve shows that a small decrease of the scattering at 800 nm is observed in this case. However, this decreasing is small (~30%) and the DRA is still considered to be resonant at 800 nm.

In order to determine which part of the DRAs is active under 400 nm and 800 nm planewave excitation, the near-field intensity distributions are computed in the Oxz plane and are plotted in Figs. 3:2(c) and 3:2(d), respectively, for 6 interesting length $L_1 = 21.5$ nm, 30 nm, 47 nm, 98 nm, 123.5 nm and 157.5 nm. For an illumination with a wavelength $\lambda = 400$ nm, a weakly excited quadrupolar plasmonic mode supported by the long bar a is observed in all the cases and a dipolar plasmonic mode with a strongly enhanced electric field is observed on the short bar c when $L_1 = 47$ nm. Please note that the small deviation between the cases of maximal scattering and maximal near-field enhancement could be understood as the result of damping from the radiative decay of LSPR modes [188]. In contrast, considering a 800 nm planewave excitation, a strong dipolar plasmonic mode is excited inducing a large electric field on the long bar a. Furthermore, the off-resonance behavior of the short bar c at this wavelength is confirmed for the asymmetric cases (short L_1).
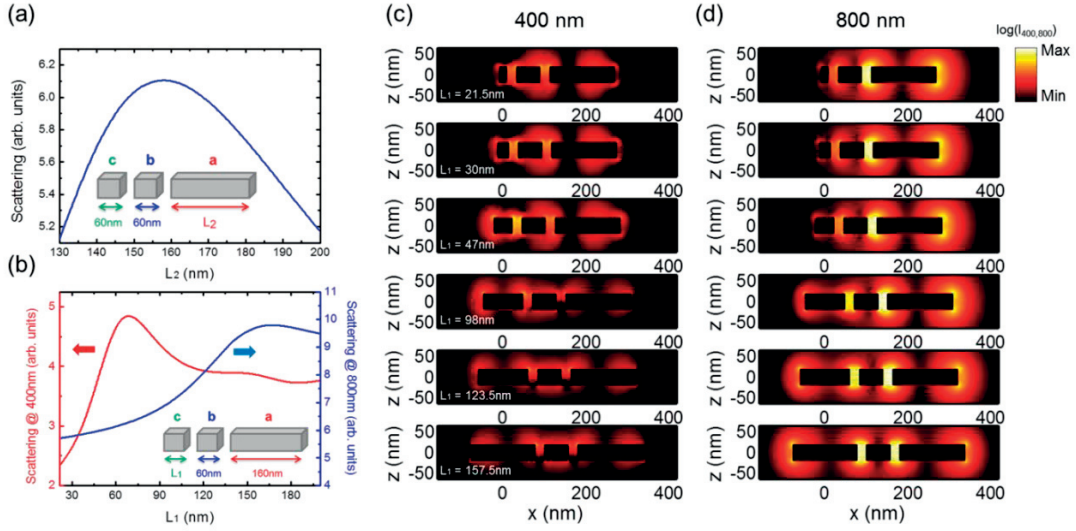
Figure 3:2 Linear scattering and near-field intensity distributions for different DRAs geometries. (a) Linear scattering as a function of the length L_2 of the long rod c for an incident wavelength of 800 nm. The lengths of the middle bar *b* and of the short bar *a* are fixed to 60 nm. (b) Linear scattering as a function of the length L_1 of the short bar a for an incident wavelength of 400 nm (red curve) and 800 nm (blue curve). Linear near-field intensity (in logarithmic scale) distributions close to the DRAs for 6 lengths L_1 considering an incoming planewave with a wavelength of (c) 400 nm and of (d) 800 nm. From the top to the bottom: $L_1 = 21.5$ nm, 30 nm, 47 nm, 98 nm, 123.5 nm and 157.5 nm.

3.2.2   SH enhancement versus plasmonic resonance

Figure 3:3(a) presents the SH intensity as a function of the length L_1 with a non-zero SH susceptibility $\chi^{(2)}$ at the surface of the total structure (gray dashed curve), long bar *a* (red curve), middle bar b (blue curve) and short bar c (green curve). The main purpose of the study is to reveal the mechanisms leading to a strong enhancement of SHG in coupled plasmonic structures supporting resonances at both the fundamental and SH wavelengths. The SH sources are generated at the edges and surface of plasmonic nanoantennas where the inversion symmetry is locally broken. Although the SH sources originate from the surface of plasmonic nanostructures, which is physically different from a far-field excitation at 400 nm, it is appealing that the enhancement of SHG in DRAs can be analyzed with far-field excitation. For instance, the SH intensity as a function of the short bar length reveals a maximum intensity when $L_1 = 47$ nm, which is matching well with the linear scattering peak under 400 nm plane-wave illumination (compare the gray dashed curve in Fig. 3:3(a) with the red curve in Fig. 3:2(b)). As the length L_1 increases, the DRA becomes off-resonance at 400 nm and the SH intensity decreases dramatically. SHG increases again when L_1 is above 130 nm since that increases the linear scattering intensity at 800 nm as shown in Fig. 3:2(b). Close to the symmetric case, the SH far-field scattering is partially suppressed due to the symmetric SH sources distribution inherent to centrosymmetric nanostructures [51, 176]. Although the linear scattering of the symmetric antenna is around 1.5 times higher than that with $L_1 = 47$ nm for an incident wavelength of 800 nm (see Fig. 3:2(b)).
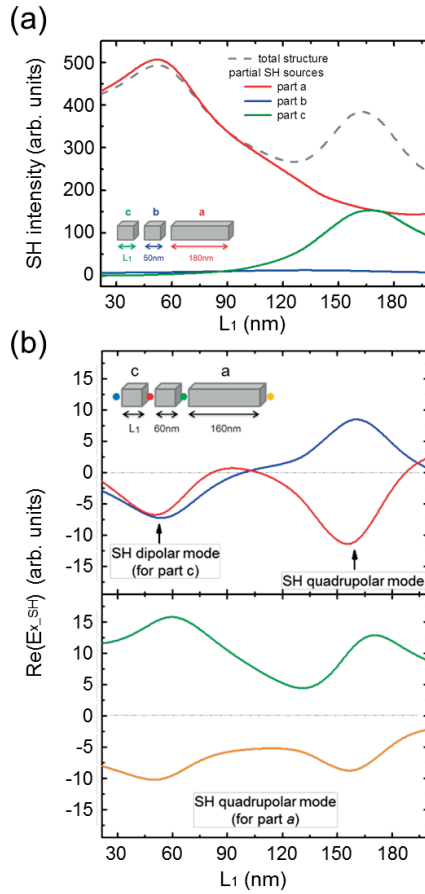
Figure 3:3 SH generation. (a) SH intensity from the total structure (gray dashed curve), long bar *a* (red curve), middle bar b (blue curve) and short bar c (green curve) as functions of L_1. (b) The real part of the *x*-component of the SH electric fields evaluated at four interesting positions as a function of the length L_1. The four considered positions are indicated in the inset with two points located at the center of the nanogaps (red and green dots) and two points situated 10 nm away from both sides of the DRAs (blue and yellow dots). The colored curves indicate the SH field at each position as a function of the length L_1.

Figure 3:4 schematically illustrates the SHG mechanism in the symmetric DRA case with both bars supporting dipolar modes at fundamental excitation. In Comparison with the DRA with one bar supporting a SH dipolar mode as shown in Fig, 3:1(b), there are mainly two differences: First of all, in the symmetric case, both bars support a dipolar resonance at the fundamental wavelength, which increases the total fundamental near-field enhancement. Second, there is no SH radiative channel (SH dipolar mode) coupled to the weakly radiative SH quadrupolar mode. Considering these factors, one can realize the reasons of higher SH intensity for DRA with $L_1 = 47$ nm than the symmetric case (shown in Fig. 3:3(a)), despite having a lower fundamental field enhancement for the prior (shown in Fig. 3:2(b)). At this stage, it is also interesting to study the SHG for aluminum nanoantenna composed of three rods resonantly coupled and each rod is resonant at the SH wavelength. In this case, the two bars on both sides of nanoantenna with a length of 47 nm can support plasmonic dipolar modes at the SH wavelength, and the gap size, the length of middle bar, width and height of the nanoantenna are remained the same as that of the DRAs, as shown in Fig. 3:5(b). First of all, we have observed that the ratio between the total SH intensity scattering by such nanoantenna and that scattered by the DRA with $L_1 = 47$ nm is 0.057. The weak SHG for the nanoantenna can be understand by the fact that a strong near-field enhancement at the fundamental wavelength is essential for an efficient SHG. Indeed, the strength of SH polarization grows quadratically with the amplitude of electric field in the linear regime due to the quadratic power dependency for SHG. Second, the near-field distribution of SH field reveals that the two bars with identical size can support the SH dipolar modes, and the two SH dipolar modes have opposite phases due to the symmetry. Therefore, the total structure can support a SH quadrupolar mode and exhibit a SH multipolar radiation as shown in Fig. 3:5(a).

To understand the influence of the length L_1 on the SH modes supported by the bars a and c, the real part of the x-component of the SH electric field $E_{x\,SH}$ at 4 interesting points, two at the center of the nanogaps and two at 10 nm away from both sides of the DRA, was evaluated as a function of short bar length L_1 as shown in Fig. 3:3(b). The top figure presents the variation of $E_{x\,SH}$ close to the short bar c. The amplitude of the SH electric fields at these points reach a maximum of amplitude around $L_1 = 47$ nm. The phase indicates that a SH dipolar mode is supported by the short bar c which induces a maximum of the SH scattering as shown in Fig. 3:3(a). The maximal excitation of the SH quadrupolar mode on the long bar a is also observed when $L_1 = 47$ nm (see the bottom panel in Fig. 3:3(b)). Two important observations can be made comparing the top and bottom panels of Fig. 3:3(b). First, as L_1 increases, the SH mode supported by the short bar c gradually vary from a dipolar nature ($L_1 = 47$ nm) to a quadrupolar nature which reaches its maximum in the symmetric case ($L_1 = 160$ nm) with no excitation for intermediate lengths ($L_1 = 98$ nm). Second, the intensity variations of SH modes on the short bar c (top panel) and the long bar a (bottom panel) indicate a coupling effect. At this point, one can suspect that the SH dipolar mode on the short bar c is excited by near-field coupling with the SH quadrupolar mode on long bar a through the *passive* middle bar b. Indeed, close to $L_1 = 47$ nm, the SH dipolar mode of bar c and the quadrupolar mode of bar a are maximal, indicating a strong dipole-quadrupole mode coupling. These two modes become weaker in the off resonance regime and increase again close to the symmetric case (when $L_1 = L_2$).
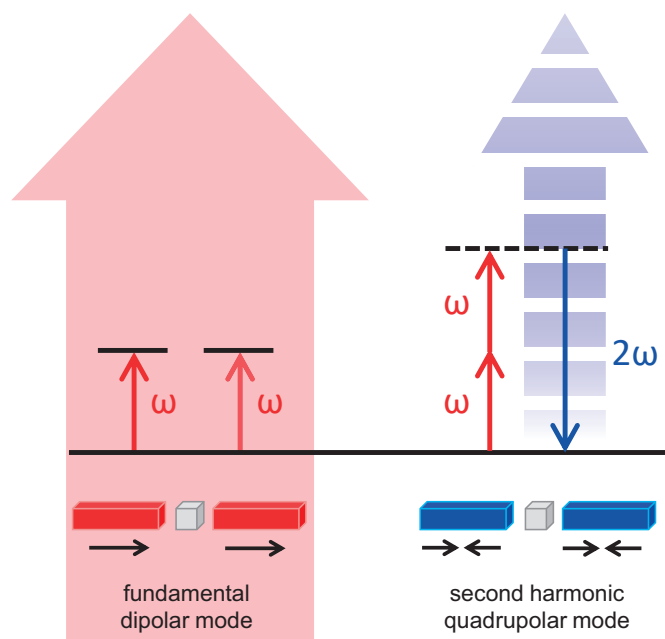
Figure 3:4 Schematic diagram of the SHG mechanism in the symmetric DRA with both bars supporting a dipolar mode under the fundamental illumination. Both of the dipolar fundamental modes generate a quadrupolar mode at the SH wavelength. The fundamental excitation and SH radiation are depicted as a red arrow and a blue dashed arrow, respectively.
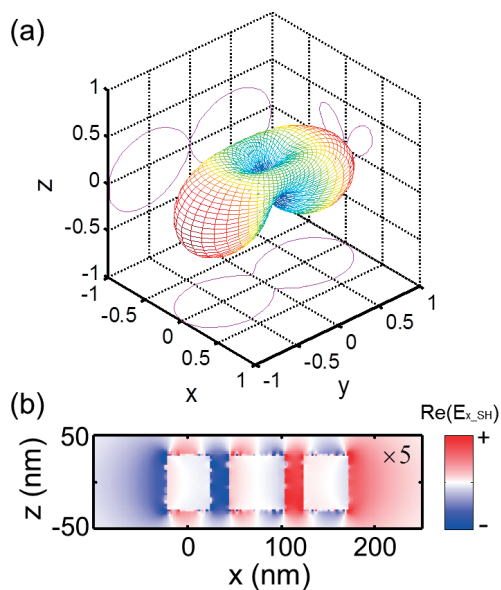
Figure 3:5 (a) Emission pattern and (b) SH near-field distribution of nanoantenna supports two plasmonic dipolar modes at the SH wavelength. The SH intensity in the near-field plot has been multiplied by 5 for viewing.

3.2.3   Roles of the different elements in double-resonant antenna

In order to confirm the importance of the mode coupling in SHG, the area-selective nonlinearity SIE method is applied to evaluate the contribution of each constituting part of DRAs. As mentioned in the previous section, the red, blue and green curves in Fig. 3:3(a) show the SH far-field scattering intensity as a function of the length L_1 considering only the nonlinear signal from the bar *a*, *b* and *c*, respectively. Note that each curve can be considered as the contribution of the SH sources standing on the surface of a given bar of the DRA. The comparison between the total SH intensity (gray dashed curve) with the SH signal from the long bar *a* (red curve) and the coincidence of the SH intensity peaks around $L_1 = 47$ nm reveals the mechanism of SHG enhancement in DRA: the near-field SH intensity from the *active* bar *a* excites the dipolar mode of the short bar *c* increasing the scattering of the SH intensity in the far-field. In addition, the long bar *a* is found to be the main contribution of the SHG from the DRAs due to its strong resonance at 800 nm. The contribution of the other constituting elements of the DRA was also evaluated. For the short bar *c* (green curve), the SH intensity is gradually increased with the bar length L_1 and reach a maximum value in the symmetric case, which is due to the resonance standing on bar *c* at the fundamental wavelength. For the middle bar *b* (blue curve), a weak SH intensity is always observed due to the off-resonance behavior at both fundamental and SH regimes. The middle bar *b* serve as a plasmonic *bridge* transferring the energy between bar *a* and *c* through the plasmonic near-field coupling at the SH wavelength.

To further confirm the importance of the mode coupling in the enhancement of the SHG from DRA, the SH near-field intensity has been evaluated using the SIE method with partial nonlinear source. The SH near-field distributions for 6 interesting lengths (L_1 = 21.5 nm, 30 nm, 47 nm, 98 nm, 123.5 nm and 157.5 nm) considering a non-zero surface susceptibility $\chi^{(2)}$ only for the long bar *a* and for the total antenna are presented in Figs. 3:6(a) and 3:6(b), respectively. From Fig. 3:4(a), one can deduce that the SH quadrupolar mode of long bar *a* transfers more energy to the short bar *c* when the small bar supports a dipolar mode than a quadrupolar mode (large L_1). The strongest dipolar mode is observed when $L_1 = 47$ nm generating a very strong SH signal (see the red curve in Fig. 3:3(a)). Interestingly, the SH near-field intensity close to the long bar *a* is also enhanced when the energy transfer occurs due to constructive interferences.
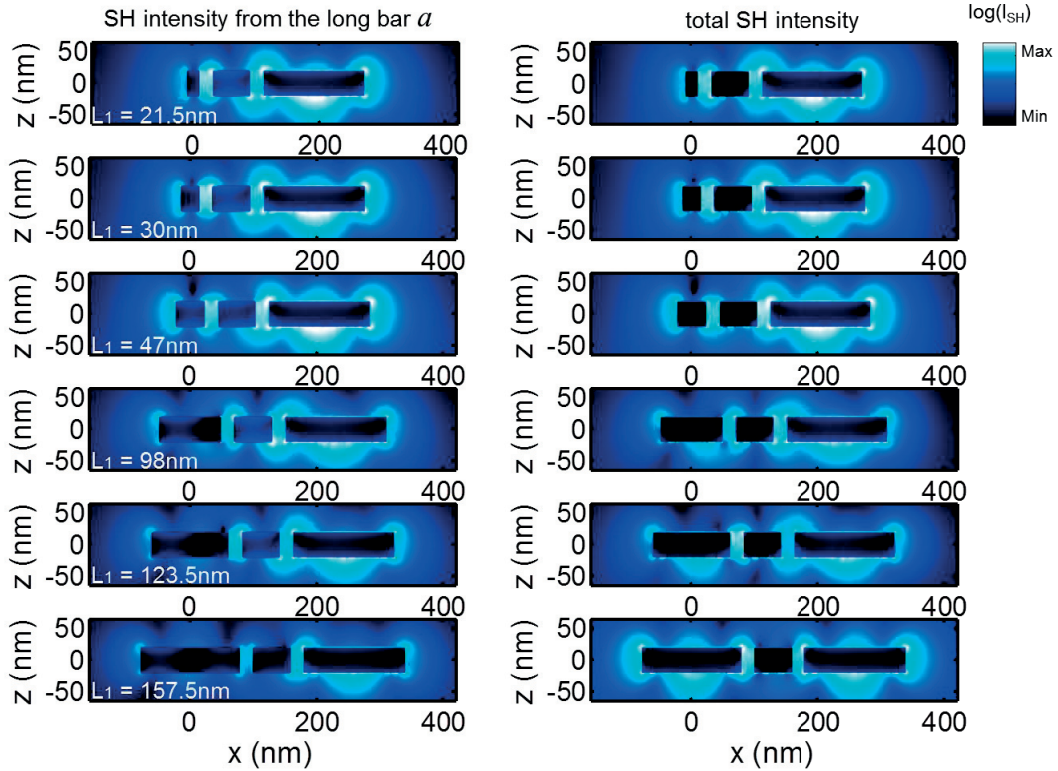
Figure 3:6 Near-field distributions of the SH intensity. 6 interesting lengths L_1 cases (L_1 = 21.5 nm, 30 nm, 47 nm, 98 nm, 123.5 nm and 157.5 nm) are considered. (a) Partial SHG from the bar a and (b) total SHG from the whole structure.

Figures 3:7 shows the SH near-field intensity and the real part of the electric field E_{x_SH} for 6 for 6 interesting lengths L_1 (L_1 = 21.5 nm, 30 nm, 47 nm, 98 nm, 123.5 nm and 157.5 nm) considering only a non-zero SH susceptibility $\chi^{(2)}$ at the surface of the short bar c (Figs. 3:7(a) and 3:7(d)), the middle bar b (Figs. 3:7(b) and 3:7(e)) and the long bar a (Figs. 3:7(c) and 3:7(f)). Figures 3:7(b) and 3:7(e) confirm the relatively weak SHG from the middle bar b and insufficient coupling strength to the other parts of the DRA due to its off-resonance properties at both fundamental and SH wavelengths. In contrast, the quadrupolar mode on the long bar a induces a strong near-field intensity for all the length L_1 and a strong coupling to the other parts of the DRA is observed (Figs. 3:7(c) and 3:7(f)). Thus, inducing a strong dipolar mode supported by the short bar c (L_1 = 47 nm) yields to the maximum SHG. When L_1 is such that the structure becomes symmetric, one can observe that the field E_{x_SH} of the quadrupolar mode supported by the bar c is symmetric with the field supported by the long bar a. The symmetry plane is defined by x = 130 nm.
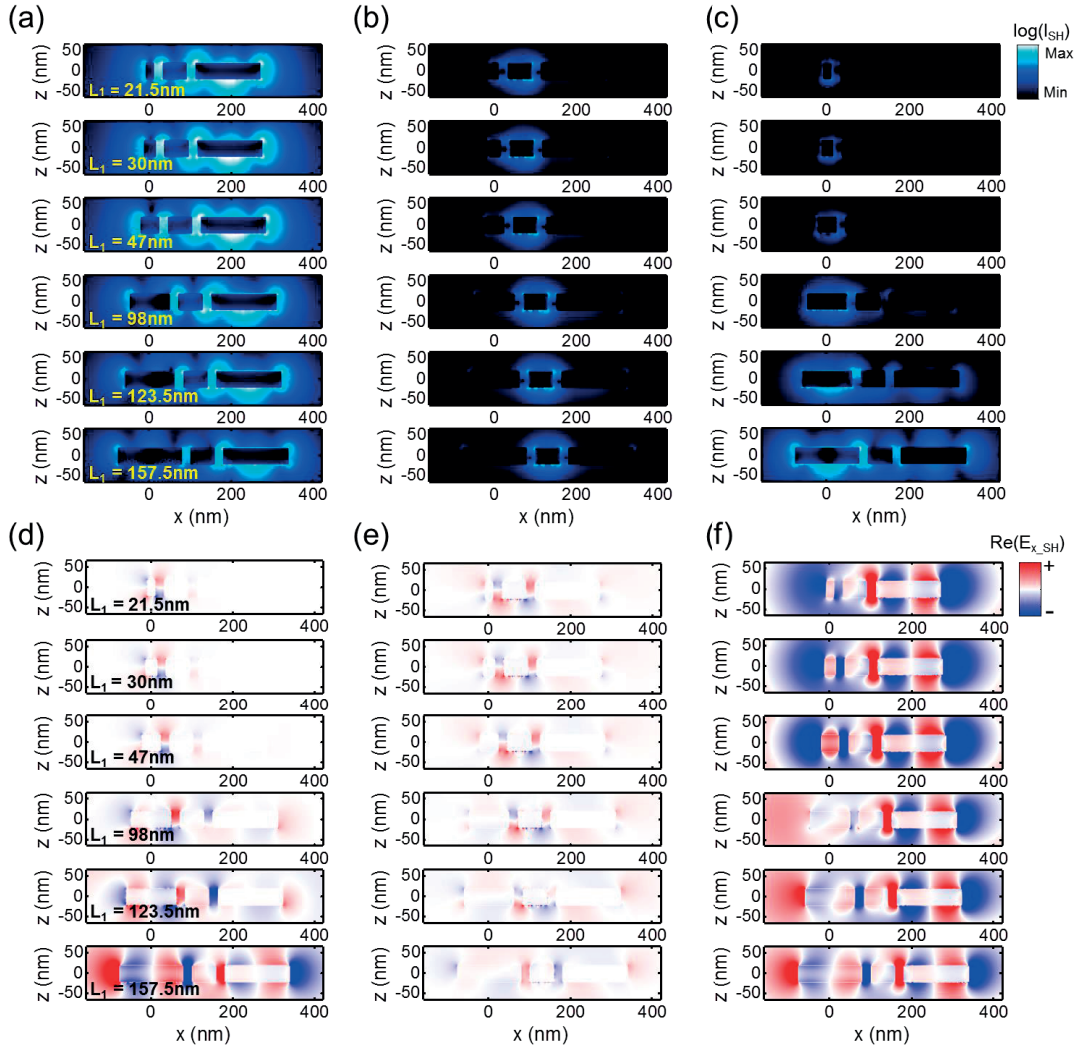
Figure 3:7 SH near-field intensity distributions for 6 interesting lengths L_1 (L_1 = 21.5 nm, 30 nm, 47 nm, 98 nm, 123.5 nm, and 157.5 nm) with a non-zero SH susceptibility $\chi^{(2)}$ at the surface of (a) the long bar c, (b) the middle bar b and (c) the short bar a, respectively. The corresponding near-field distributions of the real part of the x-component SH electric fields are presented in the bottom panel with non-zero susceptibility $\chi^{(2)}$ on the surface of the (d) short bar c, (e) the middle bar b and (f) the long bar a, respectively.

The different coupling regimes induce various SH near-field distributions resulting in various SH radiation patterns (Fig. 3:8). First, the symmetry is broken along z direction i. e. the emission patterns in the forward and backward directions are different. This fact is due to the retardation effects in SHG although the structure is 40 nm thick. The SH intensity is higher in the backward direction (bottom part of the polar plots) than in the forward direction (top part of the polar plots). Second, the SH emission pattern is different in the +x and –x directions due to the different scattering intensity from the SH mode supported by the bar c and the SH quadrupolar mode of long bar a. For the top three cases (L_1 = 21.5 nm, 30 nm, and 47 nm), the radiation patterns are found very similar since all correspond to a strong dipole-quadrupole mode coupling. In the case of L_1 = 47 nm, the strongest SH intensity is observed (Fig. 3:3). For the cases with L_1 = 98 nm

and 123.5 nm, the SH scattering intensities are reduced by the off-resonant behavior of the short bar c. A symmetric emission pattern is observed when $L_1 = 157.5$ nm as expected for a symmetric nanostructures. The right panel in Fig. 3:7 shows the evolution of SH near-field distributions depends on the length of L_1 for the case where $\chi^{(2)}$ is applied to the whole nanoantennas. Indeed, on the short bar c, the near-field distributions corresponding to a pronounced SH dipolar mode and a SH quadrupolar mode can be clearly recognized in the case of $L_1 = 47$ nm and 157.5 nm, respectively.

Except the study of SH near-field distributions and SH radiation patterns, the multipolar analysis of the SH emission also provides a clear information of the contribution of SH modes supported on the subwavelength plasmonic nanoantennas. To further understand the role of the energy transfer occurring at the SH wavelength in the enhancement of the SHG from the DRA, a multipolar analysis of the SH emission has been performed for a single Al nanorod (L = 160 nm), the DRA ($L_1 = 47$ nm), and the symmetric antenna ($L_1 = 160$ nm) as shown in Fig. 3:9. Here, the approach used is similar to the one developed by S. Mühlig et al. [189], excepted that the SH emission is considered instead of the linear scattering. The case of SHG from a single Al nanorod is considered first, in order to emphasize the specificity of the DRA. The multipolar analysis reveals that the SH emission corresponds to a quadrupolar emission associated with a dipolar one. Note that the dipole moment is aligned along the propagation direction and is due to the retardation effect at the fundamental wavelength as intensively discussed in the past [190-193]. These observations are then characteristic of the SHG from a centrosymmetric object with a small size (shorter than the wavelength) [190-193]. Indeed, for this class of nano-objects, the centrosymmetry must be broken by the field properties and SHG is not possible in the electric dipole approximation [190-193]. In comparison with a single nanorod, the SHG from the DRA and the symmetric antenna involves high order modes, starting with the octupolar one. However, two main differences are observed. First, the SHG from the symmetric antenna has higher contributions from higher multipolar moments. For example, the octupolar contribution is higher in the case of the symmetric antenna. Second, the orientation of the SH dipolar moment is not the same for the two antennas. For the symmetric antenna, the SH dipolar moment is along the propagation direction of the incident wave, as observed for the single nanorod, meaning that this excitation of this mode comes from the retardation effects at the fundamental wavelength. On the contrary, the SH dipolar moment supported by the DRA is mainly along the antenna arms (only a small component is induced by the field variation at the pump wavelength). The new orientation of the SH dipolar moment is a direct consequence of the energy transfer occurring at the SH wavelength. Indeed, as discussed in the previous section, the nonlinear sources standing at the surface of the long nanorod resonantly drive the dipolar mode of the short nanorod at the SH wavelength, resulting into a dipolar SH far-field radiation polarized along the antenna axis. Although the DRA gives the highest SHG, it should be mentioned that the ratio between the total SH intensity scattered by the DRA and that scattered by the single nanorod is 1.6 and that the ratio between the total SH intensity scattered by the DRA and that scattered by the symmetric antenna is 1.4 in the simulation.
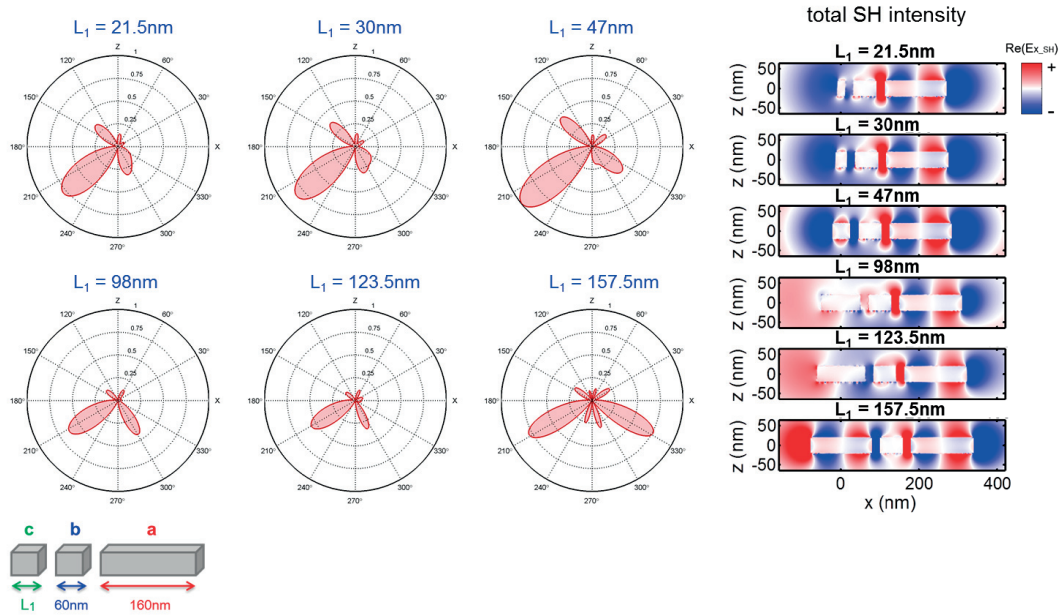
Figure 3:8 Simulated SH radiation patterns in the Oxz plane ($y = 0$) of 6 interesting length L_1 (L_1 = 21.5 nm, 30 nm, 47 nm, 98 nm, 123.5 nm and 157.5 nm). The 800 nm incident plane wave is linearly polarized along the antennas arms and propagates along the z-axis. The corresponding near-field distributions of the real part of the x-component of the SH electric fields is presented in the right panel with non-zero $\chi^{(2)}$ on the surface of the whole nanostructures.
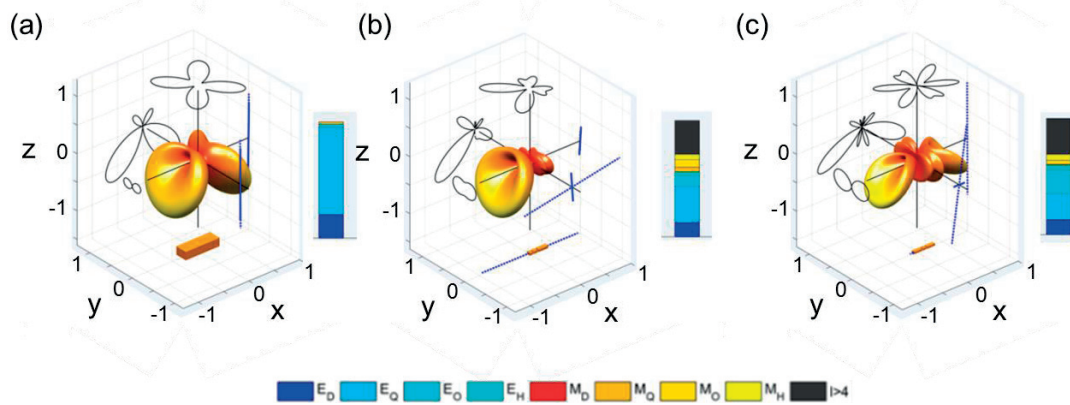
Figure 3:9 SH emission patterns for (a) a single Al nanorod (L = 160 nm), (b) the DRA (L_1 = 47 nm), and (c) the symmetric antenna (L_1 = 160 nm). The corresponding emission patterns have been decomposed into the vector spherical harmonics and the weights of the different orders are shown as histograms. The calculations were made by G.D. Bernasconi from the NAM-EPFL.

To clarify the choice of DRA for enhancing the SH emission, it is worth to study the SHG in a double-resonant aluminum dimer composed of a long rod (160 nm) and a short rod (47 nm) resonant at the fundamental and SH wavelength, respectively. Similarly to the DRA with L_1 = 47 nm, the SH dipole-quadrupole coupling can also be clearly identified in the double-resonant dimer as shown in Fig. 3:10(d). However, we observed that the ratio between the total SH intensity scattered by the double-resonant aluminum dimer and that scattered by a single aluminum nanorod (160 nm) supports plasmonic dipolar resonance at the fundamental wavelength is only 1.1, which is much smaller than the value (1.6) for the DRA as mentioned before. Please note that the ratio between the linear scattering intensity at 800 nm for the double-resonant dimer and that for the DRA is 0.9, which shows a very close strength of plasmonic resonance at the fundamental wavelength between both systems. Therefore, the weaker SH enhancement for the double-resonant aluminum dimer might be related to a lower surface area of elements resonant at the SH wavelength, which results in a reduced coupling with the SH quadrupolar mode supported on the long bar. Indeed, the SH near-field distribution clearly reveals that the SH field is stronger nearby the middle bar and short bar for the DRA than that around the short bar of the double-resonant dimer as exhibited in Fig. 3:10.

46
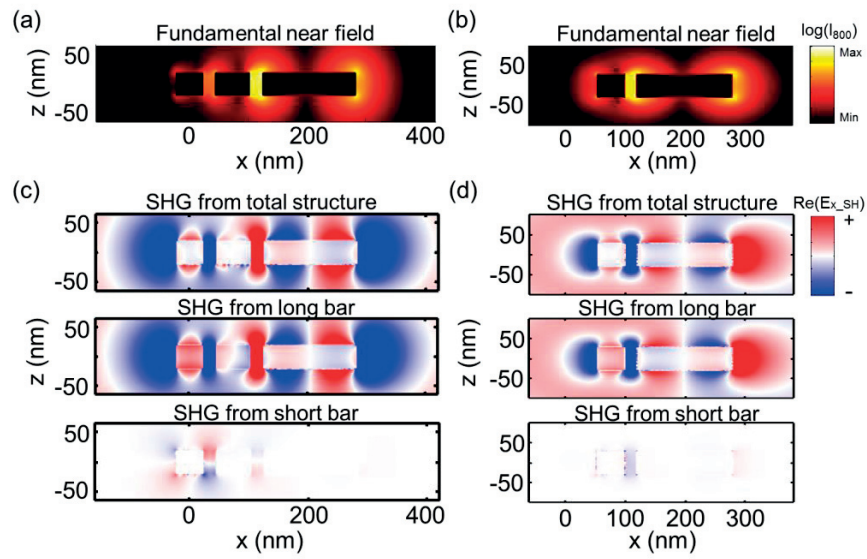
Figure 3:10 The comparison between the SHG in the aluminum DRA and double-resonant dimer. The fundamental near field distributions of the (a) DRA and (b) double-resonant dimer, respectively. (c) The near-field distributions of the real part of the *x*-component SH electric fields for the DRA when the non-zero susceptibility $\chi^{(2)}$ is applied on the surface of the total structure (top), long bar (middle) and short bar (bottom), respectively. (d) The same simulation as (c) for the double-resonant dimer.

3.3 Experimental results

To experimentally investigate the SHG from DRAs, samples were fabricated on a glass substrate with electron beam writer with 100keV electron gun (Vistec EBPG5000) followed by a lift-off. In order to improve the morphologic uniformity of aluminum nanoantennas, the oxidation of aluminum was carefully prevented during the electron beam lithography (EBL). We have fabricated line arrays of DRAs with 17 different lengths L_1 ranging from 39 nm to 175 nm. The DRAs are arranged in single line array with 300 nm period.

For the nonlinear optical measurements, a multi-photon scanning microscopy (LEICA SP5 MULTI-PHOTON) combined with a Ti:Sapphire femtosecond laser working at 800 nm with 140 fs pulse duration (Fig. 3:11(a)) [194, 195]. As the length L_1 increases, the signal intensity decreased to one-half when $L_1 = 115$ nm and rises again close to the symmetry case due to the strong resonance at the fundamental wavelength. The experimental results are in excellent agreement with SIE simulation (Fig. 3:11(b)). The slight shift of the short bar length corresponding to a maximal SH intensity between the measurement and simulation could be induced by geometric defects in the fabricated nanoantennas. Indeed, it has been shown that the SH far-field distribution is extremely sensitive to the nanoantenna morphology [145]. Therefore, the difference of the SH emission patterns for ideal and realistic nanoantenna shapes can lead to variations in SH intensity collected by the objective. Please note that in order to confirm the experimental observation with simulation, the calculated SH intensity for each case is obtained by collecting the backward SH scattering field within the reflection cone 48.8° with the normal. This can be done simply by evaluating the SH electromagnetic field on the surface of a sphere of 10 μm around the nanostructure and integrating the field over the surface area defined by the intersection of the reflection cone and the sphere. Figure 3:12(a) shows the SH backward intensity image. Each bright line corresponds to the SH signal from a line array with a given value of L_1. As expected, the intensity is maximum when the SH dipolar mode on the short bar c is excited. Figure 3:12(b) shows the SEM images of DRA line arrays with 6 different length L_1 revealing high-quality nanostructures.
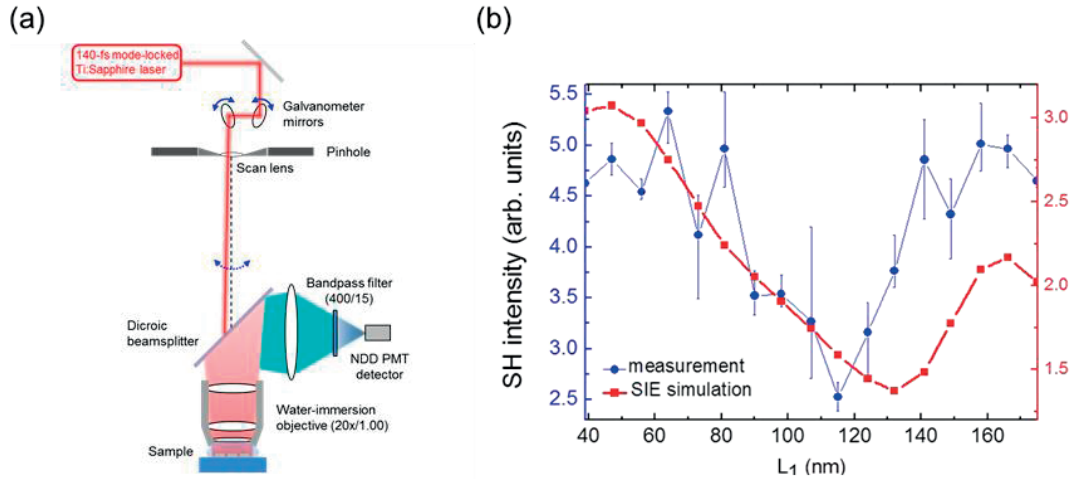
Figure 3:11 Experimental results of the SH generation for different length L_1. (a) The overall system configuration for the nonlinear optical measurements. The multi-photon scanning microscopy with galvanometer resonant mirrors (400 Hz scanning speed), scan lens and 20x/1.00 water-immersion objective enable a $387.5\ \mu m \times 387.5\ \mu m$ scanning field with 758.32 nm pixel resolution for a Ti:Sapphire 140-fs laser working at 800 nm. The backward SH scattering is collected with the same objective, a dichroic beam splitter (reflecting the wavelength below 700nm), a collection lens, a bandpass filter (400/15 nm) and a photomultiplier tube (NDD PMT). (b) Measured and SIE simulated SH scattering intensity as functions of the length L_1. In the SIE simulation, the colleting angle is adjusted to fit the experimental one (angle of $48.8°$ with the normal).
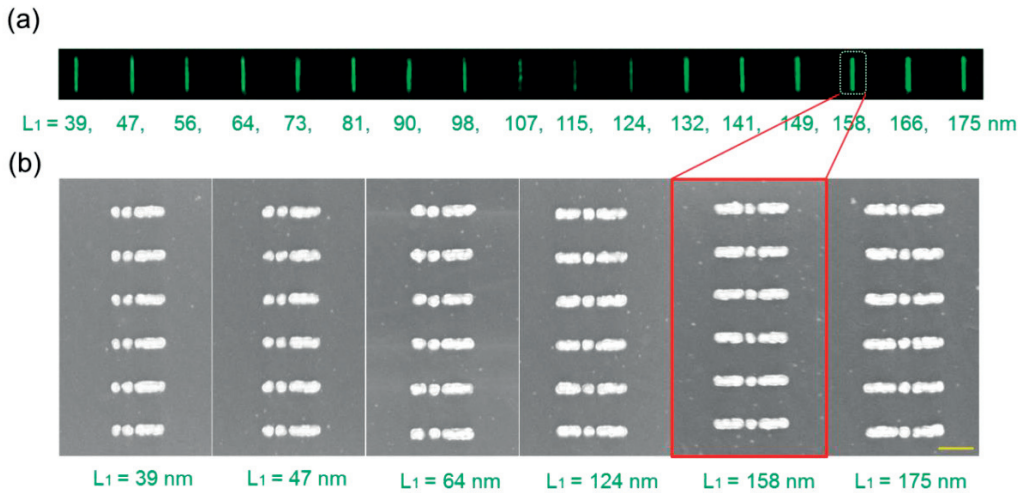
Figure 3:12 (a) SH image showing the signal from 17 line arrays with different length L_1. (b) Scanning electron microscopy (SEM) images of line arrays for 6 selected length L_1 are shown ($L_1 = 39$ nm, 47 nm, 64 nm, 124 nm, 158 nm and 175nm). The scale bar at the right bottom corner corresponds to 200 nm.

Figure 3:13 presents the experimental power dependence of the SH intensity of three DRAs with L_1 = 47 nm, 115 nm, 158 nm. The measurements fit well with a quadratic dependence. Clearly, the SHG from the optimized DRAs L_1 = 47 nm is around 2 times stronger than the off-resonance case (L_1 = 115 nm) and also higher than the case close to symmetric configuration (L_1 = 158 nm).
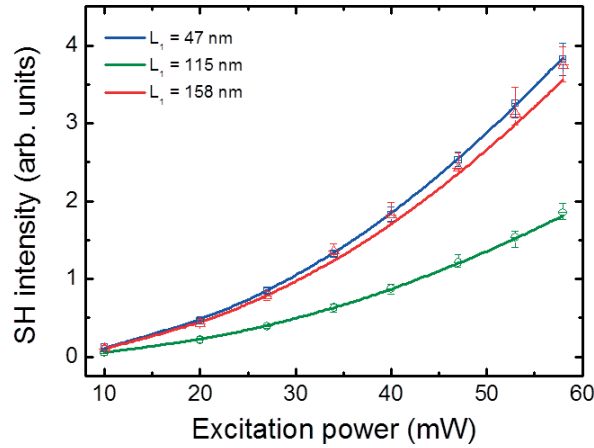
Figure 3:13 SH intensity as a function of the excitation power for three lengths L_1 = 47 nm, 115 nm, and 158 nm.

3.4 Conclusions

In summary, we provide a full understanding of the mechanisms that lead to enhancement of SHG in double-resonant plasmonic nanoantennas. By combining SIE simulations with up-to-date fabrication techniques and sensitive nonlinear optical experiments on aluminum plasmonic nanostructures, the modulation of SHG from DRAs was studied for a broad variety of geometries. For this purpose, the length L_2 of the long bar a of DRAs was first optimized and fixed at 160 nm, while the short bar length L_1 is varied from 20 to 200 nm. We clearly observe that the SH intensity is maximum when the short bar c exhibits a maximum scattering cross section in the linear regime at 400 nm. The SH intensity observed in this case is twice the value obtained when the short bar c does not have any resonant behavior at 400nm. The corresponding SH near-field distribution confirms the presence of a quadrupolar SH supported by the long bar a exciting a dipolar mode on the short bar c. This energy transfer is revealed for the first time in frequency conversion in plasmonic nanostructure and represents a new way for increasing nonlinear optical conversion at the nanoscale. These results provide a clear physical insight of the physical mechanisms of the SHG enhancement in multi-resonant plasmonic structures which are promising for the design efficient EUV sources and SH index sensor [177-179, 184].

4. Wavevector-selective nonlinearity with three-dimensional nanostructures

Nonlinear metasurfaces combine their extraordinary electromagnetic properties with the nonlinear response of their constituting elements. In this chapter, the optical SH generation from plasmonic metasurfaces composed of extended 3D gold nanopillars with different out-of-plane orientations is investigated in detail using the tunable plane-wave illumination scheme with Fourier-plane imaging method. The experimental results demonstrate that, thanks to their 3D nature, the fabricated assemblies act as wavevector selective nonlinear plasmonic metasurfaces beyond the nonlinear response expected for single and isolated nanopillars. Interestingly, specular SH reflection is observed, although the average inter-particle distance is larger than the diffraction limit at the SH wavelength. Nanopillars with various tilt angles and heights are considered, demonstrating how the asymmetry of the SH response can be controlled and emphasizing the importance of both the nanostructure shape and plasmonic enhancement. Indeed, a variation of the SH intensity as high as 80 times is measured for incident waves with opposite illumination angles (see Fig. 4:1), paving the way for an optimal design of directional nonlinear plasmonic meta-mirrors. Parts of this chapter have been published in Ref. [196] and the nanostructures were realized in the group of M. Käll at Chalmers University of Technology. In this study, I have implemented the nonlinear Fourier-plane imaging setup to characterize the SH emission from the metasurfaces. The SH SIE simulation was made by J. Butet from the NAM-EPFL.
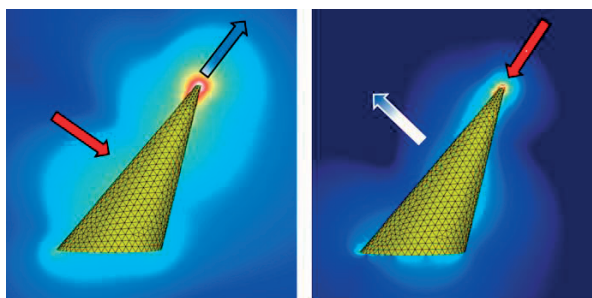
Figure 4:1 Schematic diagram of wavevector-selective nonlinearity in tilted 3D gold nanopillars. The fundamental illumination and SH emission are shown as red and blue arrows, respectively.

4.1 Introduction

Metasurfaces have become an important topic of research in optics during the last year [92, 93, 197, 198]. This interest was triggered by the possibility to observe new optical phenomena, such as negative refraction [199, 200]. The specific control of light offered by metasurfaces enables the design of ultra-thin planar lenses [109], Gaussian-to-Bessel beam transformers [201], broadband optical filters [202], quarter-wave plates [114], and sensitive biosensors [203-205], complex color routing devices [206] to name a few typical examples of the new possibilities they offer. Furthermore, the elements constituting a metasurface, the "meta-atoms", do not only exhibit unexpected linear responses, but also possess an intrinsic nonlinearity [70, 160, 207]. Indeed, when metasurfaces interact with an intense light beam, as that produced by laser systems, various nonlinear optical processes can be observed, such as nonlinear optical conversion, corresponding to the generation of light at a new frequency [70, 160, 207]. However, nonlinear studies of metasurfaces are still rare, in comparison with those reporting observations made in the linear regime. This is probably due to the lack of knowledge about the nonlinear responses of their meta-atoms (dielectric and plasmonic nanoparticles), despite recent important advances in that field [70, 160, 207], that have revealed the enhancement of the nonlinear responses by different mechanisms, including the spatial organization of the meta-molecules [72, 208] or the excitation of magnetic modes [77, 209]. While optimizing the overall nonlinear optical conversion is important for the realization of practical applications, a subtle design of the coupling between the pump laser and the metasurface is also essential for the control of its nonlinear response. In this context, in-plane meta-atoms have only been considered so far, meaning that the best coupling with the incident wave is in general reached at normal incidence and at the resonance wavelength [88, 89, 210-212]. However, simultaneous control of the angular and spectral dependencies of nonlinear metasurfaces, extending the concept of wavevector filtering [213] to the nonlinear regime has not yet been reported, despite possible applications beyond those offered by diffractive optics [214].

In this chapter, the SHG from arrays of tilted gold nanopillars, made using a hole-mask colloidal lithography technique, see Fig. 4:2, are investigated in details. The SHG signal is measured using a nonlinear Fourier microscope permitting recording the angular dependence of the SH intensity for a wide range of illumination angles. The experimental observations are compared with

computations done for single nanostructures. Due to the specific geometry of the plasmonic nanopillars, it has been reported that a strongly enhanced SH field can be induced around the tips when the incident electric field is polarized along the nanocone axis [215, 216]. However, these works only studied the plasmonic-enhanced SHG in a symmetril 3D nanocones. Here, nanocones with various tilt angles and heights are considered in order to determine how the asymmetry in the SH response can be controlled.
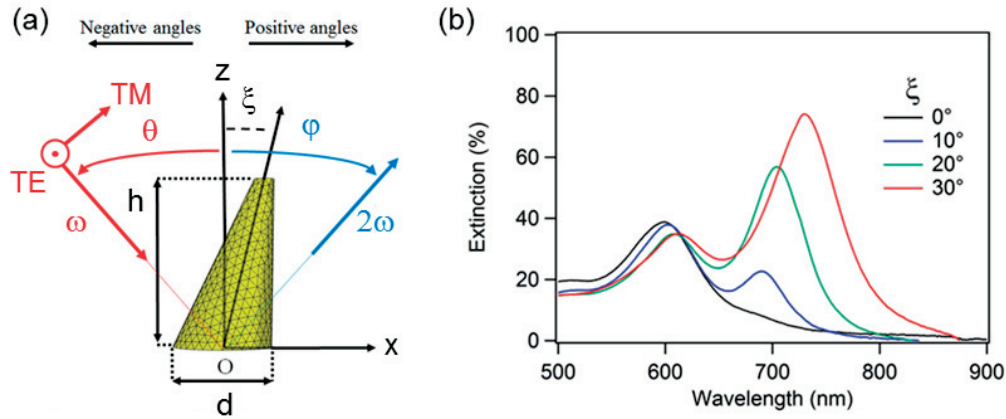
Figure 4:2 (a) Definition of the different parameters used in this chapter. The nanopillars are defined by their tilt angle ξ, their height h, and the diameter of their basis d. The angle θ corresponds to the illumination angle and the angle φ corresponds to the collection angle. (b) Extinction as a function of the incident wavelength for deposition angle ranging from 0° to 30°. The height h is 170 nm and the diameter d is 100 nm. The measurements are performed in air.

4.2 Experimental realization

Several samples, homogeneous over a few cm^2 with a density of ~4 nanocones/μm^2, were produced using a modified version of the hole mask colloidal lithography method [217]. In brief, 100 nm polystyrene beads were dispersed on top of a resist and a 10 nm Au mask was evaporated. After removal of the beads by tape stripping, the resist underneath the hole was etched by oxygen plasma in order to produce a large undercut and Ti and Au layers were deposited at glancing angles followed by lift-off in acetone. During evaporation, the hole of the mask progressively shrinks, resulting in a tapering of the deposited structures. Scanning electron microscope (SEM) measurements confirm that the tilt angle ξ is equal to the deposition angle. Figure 4:4 shows SEM images of the metasurfaces fabricated by deposition of 170 nm of gold with different deposition angles. The surface is covered by short range ordered titled nanoparticles, conical in shape due to complete closing of the holed mask at the end of the evaporation process.

4.2.1 Wavevector-selective response in tilted Au nanopillars

The samples were first characterized by standard transmission spectroscopy in air at normal incidence in Fig. 4:2(b) using linearly polarized light along the x-direction, as well as dipole moment calculations (Fig. 4:3). While the vertical nanocones exhibit a single resonance at 600 nm, by progressively tilting the particles, an additional resonance appears at a longer wavelength. The behavior can be related to a lower symmetry of the system: in the case of the tilted nanocones, the in-plane and out-of-plane resonances start to hybridize, resulting in a tilting of the net dipole moment of the structure even for normal incidence illumination, although in contrast to previous work [217], here the two resonances are spectrally well separated. In particular, from numerical simulations we extracted the net induced dipole moments p along the x- and z-directions and calculated the net tilt angle of the resulting dipole moments for normal illumination. For the non-tilted structure ($\xi = 0°$) the induced dipole is, evidently, parallel to the substrate. However, due to mode hybridization for $\xi \neq 0°$, the dipolar orientation angle changes from close to horizontal to 60° as the wavelength increases, this evolution being related to the deposition angle. Close to the high energy resonance, the dipolar angle is small, indicating an almost in-plane resonance with a small phase offset between the dipole moment in the x- and z-directions. For the long wavelength resonance, the induced dipole is more vertical and, due to the hybridization of the modes, it does not align perfectly with the tilt of the nanostructure. The normal incidence illumination indicates that for tilted nanostructures the main axis of the system does not coincide with the experimental reference frame. As a consequence, for these tilted nanopillars, we can expect a strong asymmetry linear/SHG response on the illumination angle for TM polarized light along the x-direction.
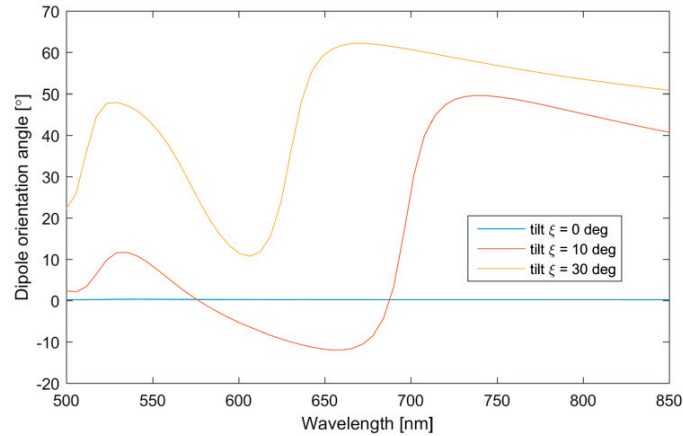
Figure 4:3 Induced dipolar tilt orientation angle with respect to the substrate for normal illumination and different nanopillar tilt angles ξ.

Having characterized the extinction spectra and the excited dipolar orientations under normal incidence for nanopillars with various tilt angles, we now turn our attention to the case with tunable planewave illumination. To do so, the home built plane-wave illumination microscope based on a Fourier-imaging method with an oil immersion objective is utilized (see the method in chapter 2). This home built nonlinear microscope permits recording the angular dependence of the SH intensity in the (O, x, z) plane as a function of the illumination angle. Note that the incident wave propagates in the same plane. The second-row pannels in Fig. 4:4 present the scattering intensity as functions of both illumination angle and wavelength for nanopillars with different tilt angles from 0° to 40°, respectively. First, two strong resonances corresponding to the excited x- and z-directional dipoles can be clearly identified at the wavelength around 650 nm and 810 nm, respectively. Second, the plasmonic resonance corresponding to the z-directional dipole moment can only be sufficiently excited with off-normal light illumination, which is due to the standing features of nanopillars. Finally, as expected, the asymmetry linear scattering on the illumination angle increased gradually with the tilt angle. Please note that the scattering spectra are obtained by removing the specular reflection in the recorded Fourier images.
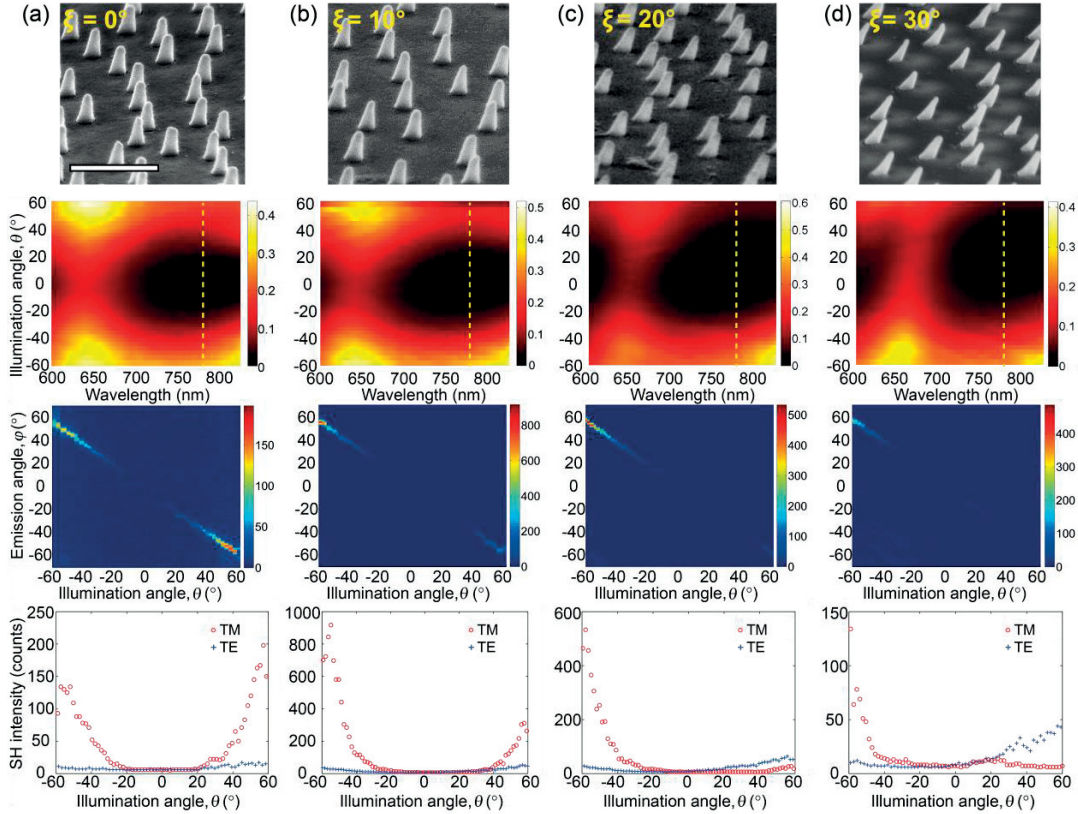
Figure 4:4 SEM images (Top panels), Scattering spectra, SH emission as a function of illumination angle, and angular dependences of the specular SH intensity an incident wave in the (O, *x*, *z*) plane with a TM polarization (red circles) and a TE polarization (blue crosses) (Bottom panels). The tilt angle is (a) 0°, (b) 10°, (c) 20°, and (d) 30°. The nanopillars height is 170 nm. For the measurement of the SHG, the wavelength of the incident laser beam is 780 nm. The scale bar in the SEM image corresponds to 500 nm.

After characterized the linear response, the SH signal of the nanopillar metasurfaces with tilt angles ranging from 0° to 30° are investigated for an incident wavelength $\lambda = 780$ nm and different illumination directions θ. As anticipated from simple symmetry considerations, the SH signal from non-tilted nanopillars (with a vanishing tilt angle) is identical for negative and positive illumination angles. In this case, the maximal SH intensity is obtained for the highest illumination angles reachable with the microscope objective ($\pm 60°$). However, as soon as the tilt angle increases, the SH response is not the same for positive and negative illumination angles and the SH intensity is high when the incident electric field is parallel to the nanopillars axis. The same effect has already been observed in SHG from gold nanotips [218-220] and nanocones [216, 221]. It is interesting to note that, contrary to the linear regime [222], a tilt angle as small as 10° already results in a significant asymmetry in the SH response. In this case, there is a factor 3-difference between the maximal SH intensity obtained for positive illumination angles and that for negative ones. To confirm that the wavevector dependency is solely due to the optical properties of the nanopillars, the SHG signal using TE illumination was also recorded and a small symmetric signal was collected in this case, Fig. 4:4. Note that since the lattice of the fabricated nanopillars sample is disordered, the only SH radiation recorded is along the direction of specular reflection [223]. In other words, the SH wave corresponds to a very narrow light beam oscillating at the SH

frequency, and no diffuse SHG is observed [224, 225]. The divergence of the reflected SH beam is estimated to be smaller than 3°, see Fig. 4:5. This is a very important experimental observation, indicating that the studied arrays of gold nanopillars actually act as nonlinear metasurfaces and that the rules derived for the SHG from surfaces and interfaces are also valid in this study. However, contrary to a flat metal surface, the wavevector-selective SH response can be controlled by the out-of-plane plasmonic modes supported by the individual 3D tilted Au nanopillars. The SH polarizations on each nanopillar can interfere constructively along the specular reflection and provide a high directionality of SH emission thanks to the homogeneity of nanopillar shape in the metasurfaces. The SH polarizations can be enhanced by the excitation of out-of-plane plasmonic modes under a proper angle of illumination. Therefore, the metasurface can be served as a wavevector-selective SH mirror. Actually, this behavior dramatically differs from the common observations made for the SHG from isolated plasmonic nanostructures [71, 84]. In this case of single nanostructures, the SH response is generally described using a multipolar expansion [70, 226], providing a suitable framework for the description of the nonlinear scattering problem.
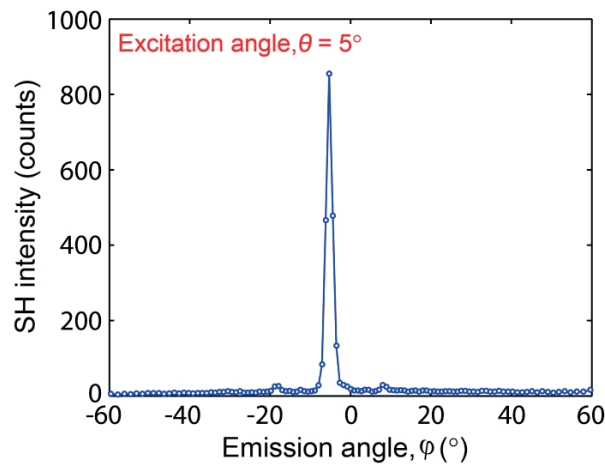
Figure 4:5 SH intensity as a function of the emission angle for the nanopillar array with h = 130 nm and a tilt angle ξ = 30°. The excitation angle is θ = 5°. The divergence of the SH beam is estimated at 3°.

To further investigate the influence of the nanopillar resonant wavelength on the SH responses of the metasurfaces, nanopillars with different heights (h = 50 nm, 90 nm, and 130 nm) but with constant base diameter (100 nm) and tilt angle (30°) have been fabricated and characterized as for the previous samples, see Fig. 4:6. The out of plane resonance in these nanostructures progressively shift from 650 nm to 850 nm for increasing heights. As the dipolar effective tilt angle is comparable for all the nanopillars, it is hence easier to investigate the influence of the resonance wavelength on the SH response. While for the thinnest nanopillar the SH response is within the noise level, it increases progressively once the resonance overlaps with the pump wavelength.
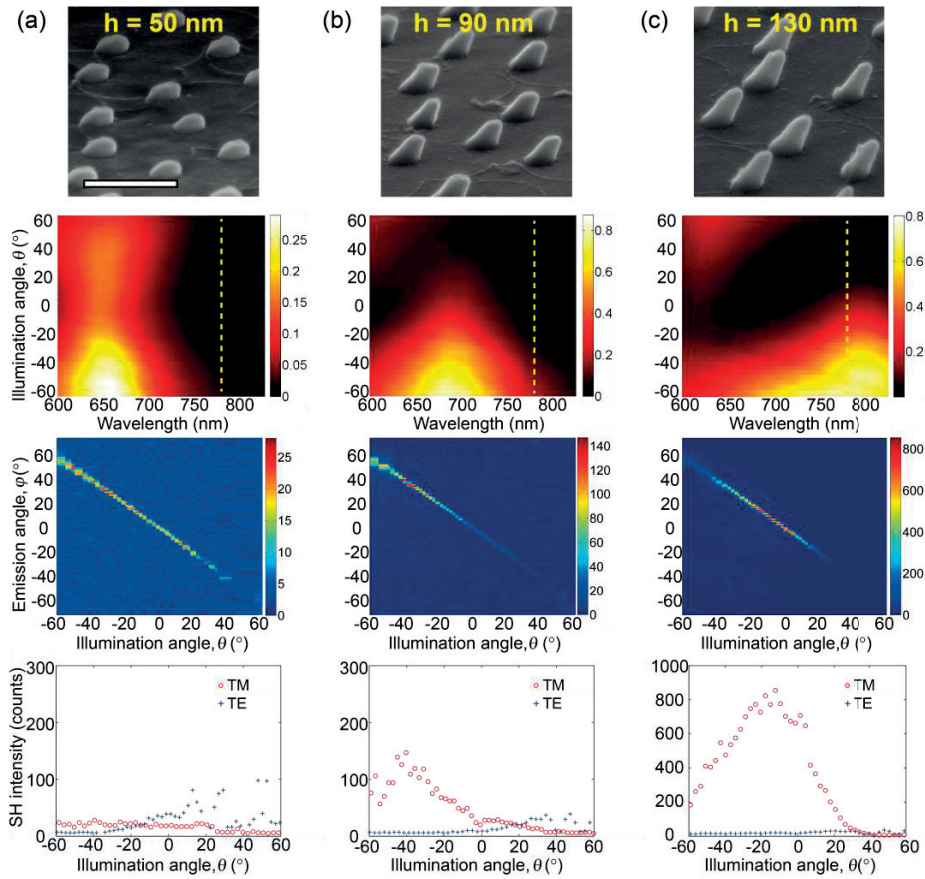
Figure 4:6 SEM images (Top panels), Scattering spectra, SH emission as a function of illumination angle, and angular dependences of the specular SH intensity an incident wave in the (O, *x*, *z*) plane with a TM polarization (red circles) and a TE polarization (blue crosses) (Bottom panels). The tilt angle is 30°. The nanopillars height is (a) 50 nm, (b) 90 nm, (c) 130 nm. For the measurement of the SHG, the wavelength of the incident laser beam is 780 nm. The scale bar in the SEM image corresponds to 500 nm.

4.2.2 Wavevector-selective nonlinearity

In any linear experiment, due to time reversal symmetry, exchanging the source and detector positions will leave the reflections from any metasurface unchanged. This is not the case in the SHG measurements, where the signal is generated by the near-field at the fundamental frequency which is wavevector-dependent. Consequently, the large asymmetry parameter observed implies also that the nanopillar arrays can indeed work as directional nonlinear mirrors. To demonstrate the effect, a focused Gaussian beam is used for illumination, see Fig. 4:7(a). Indeed, such a laser beam can be decomposed into the sum of incident planewaves with different wavevectors [227]. When the incoming beam is focused by the objective lens with a high numerical aperture (NA), the paraxial approximation is no longer valid for a tightly focused Gaussian beam. In this case, the electric field distribution in the focal plane of the Gaussian beam exhibits field components polarized in direction of propagation [227]. In our experiment, the beam diameter has been reduced to a few micrometers by enlarging the laser beam to fill the whole back aperture of the microscope objective. The same incident power is used as previously (10 mW). The SH far-field emission has been recorded in the Fourier plane for gold nanopillars with d = 100 nm, height h = 130 nm, and tilt angle ξ = 30°, see Fig. 4:7. An asymmetry in the nonlinear emission is clearly observed in Fig. 4:7(b), although a symmetric incident beam is used. To prove that this asymmetry is due to the sample properties, not to an experimental bias, the sample has been flipped and measured again in Fig. 4:7(c). In this case, the nonlinear emission pattern also flips, demonstrating the validity of the measurement. The asymmetry of the nonlinear emission pattern is explained by the wavevector selection occurring at the fundamental wavelength. Indeed, as demonstrated previously using a planewave excitation, only the incident conditions able to drive the surface plasmon resonances in the nanopillars give a significant SH emission. In the present case, only a given part of the wavevectors composing the focused Gaussian beam indeed interacts with the sample, explaining the asymmetry in the SH emission. It is worth noting that, due to the beam size reduction, fewer nanopillars are illuminated and the nonlinear response is somehow between that of metasurface (specular reflection) and that of a single nanopillar (nonlinear scattering), explaining the observed two-lobe pattern in Fig. 4:7. Interestingly, in the nonlinear regime, the nanopillars arrays act as optical diodes, filtering the incident light and interacting only with the components propagating in the correct direction.
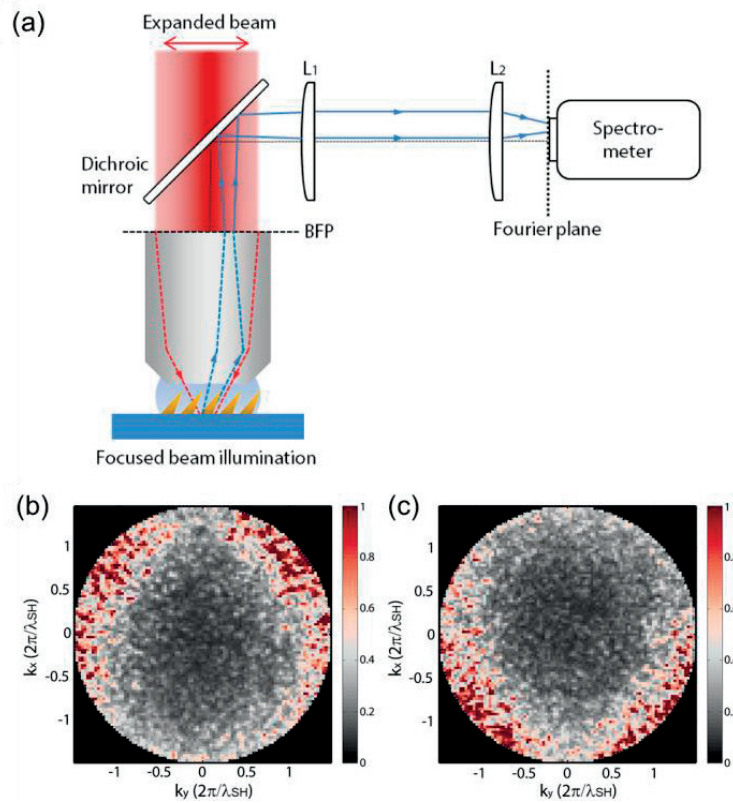
Figure 4:7 (a) Experimental configuration with a focused beam illumination. SH far-field emission recorded in the Fourier plane for gold nanopillars with d = 100 nm, height h = 130 nm, and tilt angle ξ = 30°. The focused incident beam is obtained by enlarging the laser beam to fulfill the whole back aperture of the microscope objective. In panel (b), the sample is oriented as described in Fig. 4:2, while, in panel (c), the nanopillars are pointing along the –x-direction.
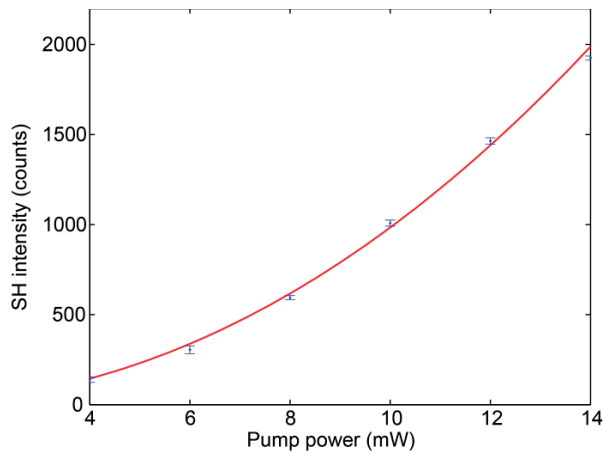
Figure 4:8 SH intensity as a function of the pump power, showing the second order nonlinearity of the recorded signal.

4.3 Simulation

To investigate the detailed properties of the asymmetry in the SH response, simulations of SHG from gold nanopillars with a tilt angle ranging from 0° to 30° have been performed using a SIE method [157, 228], see Fig. 4:9. Single nanopillars embedded in an effective surrounding medium (effective refractive index $n = 1.4$) are considered for all the computations. In the case of nanopillars with a vanishing tilt angle, the total SH intensity is identical for incident waves propagating in the $+x$- and $-x$-directions, as expected from symmetry consideration. However, the near-field distributions of the SH intensity are not symmetric. This reveals that retardation plays an important role in the nonlinear response, despite the non-centrosymmetric shape of the studied nanostructures. As a consequence of retardation, SH emission does not correspond to emission of a pure electric dipole but is multipolar in nature, see Fig. 4:10. This point underlines that full-wave computations are essential for the full understanding of SHG from plasmonic nanostructures [229]. In this framework, it is important to identify the position of the nonlinear sources over the nanopillar surface. The SH intensity is the highest at the nanopillar apex, indicating that the strongest sources of SHG are localized in this area. The strong nonlinear polarization at the nanopillar apex is a direct consequence of the strong fundamental field enhancement, as discussed previously in Refs. [218-221, 226]. For all the gold nanopillars, the SH intensity is higher for an incident wave polarized along the nanopillar axis than for an incident wave polarized along the y- or z-axis. The SH intensity is maximal when the fundamental wavelength matches the resonant wavelength of the longitudinal mode. As the tilt angle increases, the effective length of the nanopillars increases, resulting in a redshift of the longitudinal mode. The computations reveal that the resonant wavelength is an important parameter for designing nonlinear plasmonic metasurfaces sensitive to the illumination condition. Indeed, away from the resonant wavelength, the SH intensity obtained for positive and negative angles is almost the same, see Fig. 4:9.
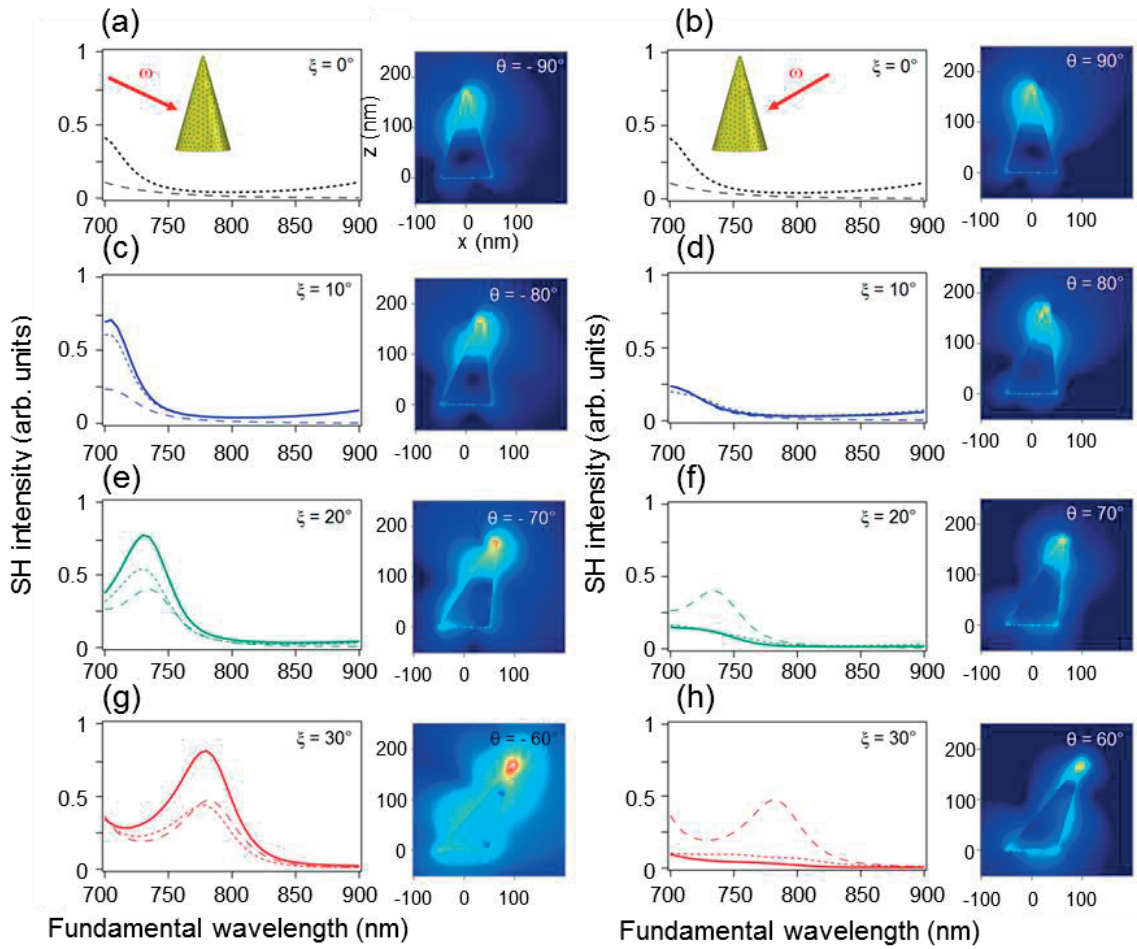
Figure 4:9 Calculated SH intensity for single gold nanopillars with a tilt angle of (a), (b) 0°, (c), (d) 10°, (e), (f) 20°, and (g), (h) 30°. The results for negative and positive illumination angles are shown in the left and right columns, respectively. The dashed lines show the SH intensity for a normal incident wave. The dotted lines show the SH intensity for an incident wave propagating along the x-axis. The full lines show the SH intensity for an incident wave polarized along the nanopillar axis (left column) or for illumination angles with the same norm and negative value (right column). The maps show the SH intensity close to the nanopillars for the denoted illumination angle, corresponding to the full lines, and a fundamental wavelength of 780 nm. The same colorscale is used for all the near-field distributions.
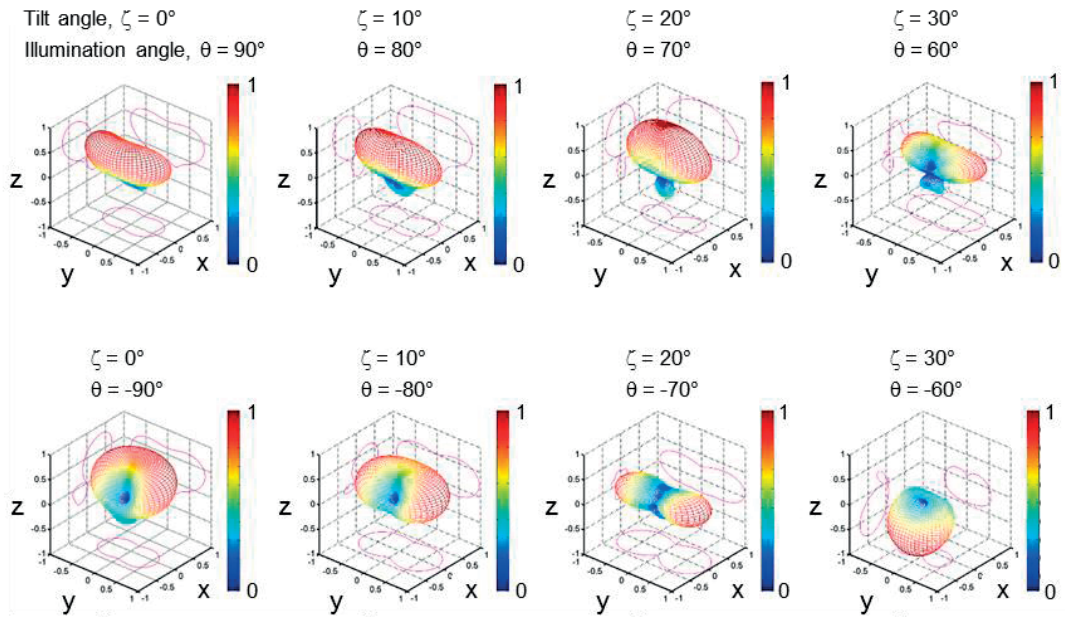
Figure 4:10 SH emission patterns for single nanopillars embedded in a homogenous medium with a refractive index n = 1.4. The fundamental wavelength is 780 nm.

To quantify the action of the nanopillar metasurfaces as nonlinear wavevector filters, an asymmetry parameter ζ is introduced as the ratio between the SH intensities obtained for negative and positive illumination angles: $\zeta = I_{SHG}(-\theta) \, / \, I_{SHG}(+\theta)$. Since measurements are performed in a reflection geometry, the asymmetry parameter hence permits us to assess the influence of the nanopillar tilt ξ on the asymmetry of the nonlinear response both experimentally (as a function of the illumination angle θ) and in simulations (as a function of the fundamental wavelength), see Fig. 4:11. Interestingly, it is observed that the asymmetry parameter ζ is not necessary the highest for the largest tilt angle. Indeed, experimentally, the asymmetry parameter ζ reaches about 30 for nanopillar tilt angles $\xi = 20°$ and $30°$. Note that the illumination angle is limited by the numerical aperture of the microscope objective (NA 1.45) and that the asymmetry parameter ζ may reach higher values for an incident condition beyond those accessible here. This limitation does not stand for the numerical results. In this case, the asymmetry parameter ζ is indeed the highest for the largest nanopillar tilt angle ξ. However, this depends on the fundamental wavelength. For a fundamental wavelength close to 750 nm, the asymmetry parameter ζ is maximal for a nanopillar tilt angle $\xi = 20°$ and, for a wavelength close to 710 nm, the asymmetry parameter ζ is maximal for a nanopillar tilt angle $\xi = 10°$, Fig. 4:11(b). Similarly, the symmetry parameter ζ progressively increases with the nanopillar height, reaching a value close to 80 for illumination angles close to 35° and for the nanopillar (h= 130nm) whose resonance best overlaps with the excitation wavelength. The asymmetry parameter ζ has also been evaluated for nanopillars with fixed tilt angle and varying heights: it is higher than 20 for illumination angles ranging from 25° to 50° for nanopillars with height h = 130 nm. Even more interestingly, for such a height, the asymmetry parameter ζ is close to 80 for illumination angles close to 35°, pointing out a very high asymmetry in the nonlinear properties of the nanopillar metasurfaces, Fig. 4:11(c). This is

due to the spectral proximity between the pump wavelength and the resonant wavelength of the longitudinal mode; see the extinction spectra in Fig. 4:6.
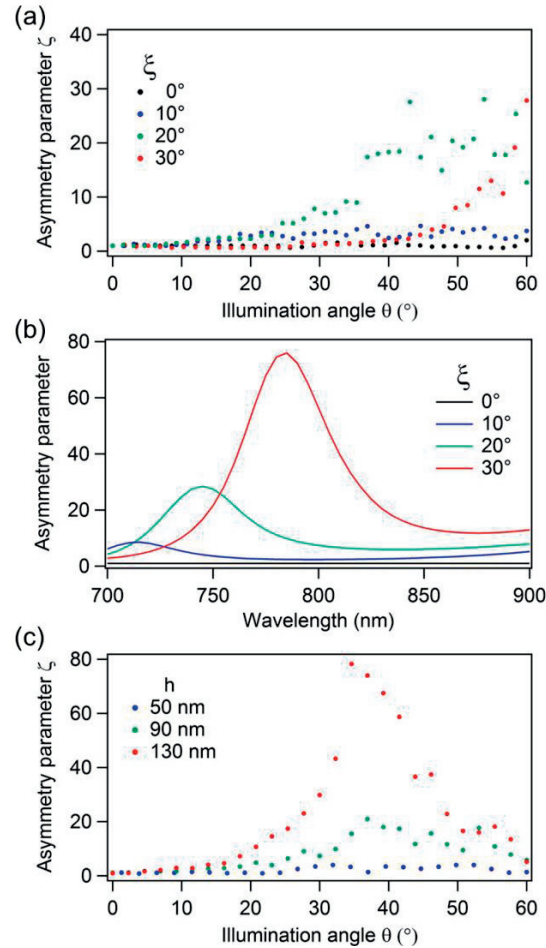
Figure 4:11 Asymmetry parameter ζ, defined as $I_{SHG}(-\theta) / I_{SHG}(+\theta)$, for tilted gold nanopillars with basis diameter d = 100 nm and height h = 170 nm as a function of (a) the illumination angle (Experimental data, Fig. 4:4) and (b) as a function of the wavelength (numerical data, Fig. 4:9). In the first case, the incident wavelength is fixed at 780 nm and, in the second case, the illumination angle giving the highest asymmetry parameter has been selected. (c) Asymmetry parameter ζ, for tilted gold nanopillars with basis diameter d = 100 nm and tilt angle ξ = 30 ° as a function of the illumination angle (Experimental data, Fig. 4:6).

4.4 Conclusions

In conclusion, SHG from arrays of tilted gold nanopillars has been investigated in details using a flexible nonlinear Fourier microscope. The experimental results demonstrate that the fabricated assemblies of gold nanopillars act indeed as wavevector-selective nonlinear plasmonic metasurfaces, beyond the nonlinear response expected for single and isolated nanostructures, but following the nonlinear reflection laws derived for nonlinear planar surfaces and interfaces. Nanocones with various tilt angles and heights have been considered, demonstrating how the illumination angle selectivity and the asymmetry in the SH response can be controlled, emphasizing the importance of both the nanostructure shape and plasmon enhancement. These observations pave the way for an optimal design of directional nonlinear plasmonic meta-mirrors.

5. Enhanced SH emission in phase-gradient metasurface

Optical SHG in plasmonic metasurfaces has gained lots of interest as a possibility to take advantage of the strong near-field enhancement in meta-atoms. This interest was triggered by fascinating symmetry properties ruling the nonlinear optical conversion at the subwavelength scale. However, despite the excitation of highly localized plasmonic modes enhancing the fundamental electric field, the SH light generated by plasmonic metasurfaces is relatively weak due to the intrinsic symmetry properties of SH generation. For example, as shown in Chapter 3, a linearly resonant aluminum nanorod will support a fundamental electric dipole under illumination, while for the SHG an electric quadrupolar mode is dominating and thus limited the SH radiation in the far-field. In this work, we propose a new approach to enhance the SH generation by combining a localized and a propagating plasmon modes in a reflective phase-gradient metasurface composed of silver nanorods on the top of a silver mirror. The SH generation is observed using our nonlinear Fourier microscope and the underlying mechanisms of the SH enhancement are revealed using nonlinear SIE simulations. Interestingly, with the area-selective nonlinearity SIE methods, the SH light is found mainly generated by the silver plate and corresponds to anomalous nonlinear reflection satisfying the phase-matching condition. These results provide a new platform for the design of ultrathin nonlinear mirrors, wavevector-selective nonlinear metasurfaces, and nonlinear metaholograms. In this study, I have done the linear and SH SIE simulation, nanofabrication, and the nonlinear measurement with the homebuilt nonlinear Fourier-plane imaging setup.

5.1 Introduction

Recently, nonlinear metasurfaces enabling the coherent control of SHG have demonstrated the importance of engineering the SH phase [86-90, 230]. These devices are achieved by simply tuning the symmetry of plasmonic constituents and leaving their linear phase and amplitude responses essentially homogeneous along the interfaces. With this design concept, nonlinear image encoding has been demonstrated in metasurfaces for which the hidden images can be only read out by SHG [135]. However, the homogeneous optical response in the linear regime inevitably leads to the radiation losses through the specular reflection and transmission in the linear regime and limits their overall SHG efficiency. On the other hand, since the symmetry of plasmonic resonant systems play an important role in the SH emission [72, 77, 82, 84, 175, 231-233], non-centrosymmetric meta-atoms are usually considered to allow the SH radiation in the forward/backward directions. It is then important to simultaneously reduce the linear radiation losses and control the nonlinear emission for the design of efficient nonlinear metasurfaces [81, 234, 235].

In this chapter, we propose a phase-gradient metasurface that can convert free-space propagating light into a unidirectional hybrid surface plasmon wave in the linear regime, which results in a strong near-field enhancement. We combine both experiments and simulation to demonstrate that the observed SH enhancement is due not only to the field enhancement but also to the near-field energy transfer from the nanostructures to the metallic backplate as the hybrid surface plasmon wave is excited. Interestingly, the single-channel SH emission governed by the SH phase-matching condition reveals the relationship of SH emission channel and excited hybrid surface plasmon wave in the phase-gradient metasurface as schematically shown in Fig. 5:1.
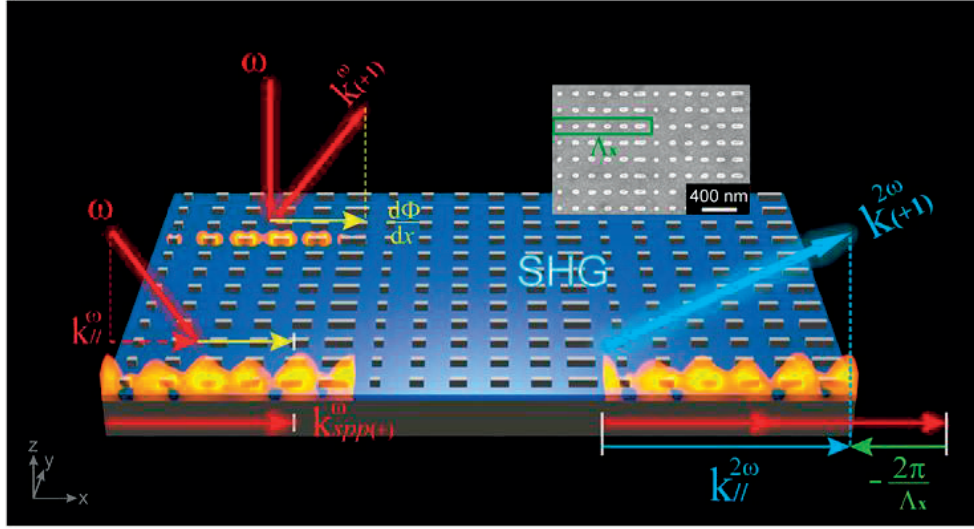
Figure 5:1 Mechanism of SHG from a phase-gradient metasurface. The unit cell of the metasurface is composed of 6 silver nanorods with different lengths (60, 70, 85, 90, 100, 130 nm) and fixed width and height (40 nm) on the top of a silver mirror with a 30-nm SiO$_2$. The in-plane momentum provided by the metasurface (yellow arrow), the wavevector of anomalous reflection (red arrow), the in-plane wavevector of incident light (red dashed arrow), the wavevector of the hybrid surface plasmon mode (long red arrow), the grating momentum (green arrow toward left), the in-plane wavevector of SH emission (blue arrow) and the wavevector of SH emission (blue arrow with glow) are denoted as $\frac{d\Phi}{dx}$, $k_{(+1)}^{\omega}$, $k_{//}^{\omega}$, $k_{spp(+)}^{\omega}$, $\frac{2\pi}{\Lambda_x}$, $k_{//}^{2\omega}$ and $k_{(+1)}^{2\omega}$, respectively. The SEM image of the top view of the fabricated sample is also exhibited in the upper-right corner.

5.2 Anomalous reflection in the linear regime

5.2.1 Phase design and far-field response

A reflective phase-gradient metasurface that works under TM-polarized illumination at 800 nm wavelength has been designed. The investigated metasurface is composed of silver nanorods with 6 different sizes located on the top of a silver mirror with a 30-nm SiO_2 spacer. In order to provide the desired phase distribution along the x direction, the lengths of the nanorods have been carefully chosen to procure a phase evolution between 0 and 2π for 800 nm illuminations.

The constant phase-gradient along the interface provides an in-plane momentum $\frac{d\Phi}{dx}$ following the generalized Snell's law [112], which deflects a normal incident beam into an anomalous reflection channel (+1 diffraction order), as sketched in Fig 5:1. The periodicities of the supercell are $\Lambda_x = 1200$ nm and $\Lambda_y = 200$ nm along the x and y directions, respectively. Now, if the incoming light is oblique, in such a way that the in-plane incident wavevector is along the direction of the momentum provided by the metasurface, then the anomalous reflection beam will be deflected with an angle higher than the specular reflection [103, 112, 113]. This anomalous reflection channel can then be tailored into an evanescent wave when the incident angle is sufficiently large [115]. Interestingly, with the proper incident angle, an unidirectional hybrid surface plasmon (hybrid SPP(+)) mode supported by the phase-gradient metasurface is excited when its dispersion is satisfied as shown in Fig. 5:1. The excitation of the hybrid surface plasmon mode is defined by the in-plane wavevector conservation:

$$k_{//}^{\omega} + \frac{d\Phi}{dx} = k_{spp(+)}^{\omega}, \tag{5.1}$$

where $k_{//}^{\omega}$ and $k_{spp(+)}^{\omega}$ are the in-plane component of the wavevectors of incident light and of wavevectors of the hybrid SPP(+) mode, respectively. It is worth to mention that, besides the excitation of unidirectional surface plasmon wave thanks to the LSPR-induced gradient phase distribution, the asymmetric SPP excitation can also be achieved by introducing a gradient local filling factor of metal in the supercell of a binary two-dimensional grating pattern, so-called blazed coded effective medium structures [236]. In their proposed structures, the blazing effect is solely induced by the gradient effective dielectric constant without utilizing the LSPRs [237]. In the following, we combine both experiments and SIE computations to investigate the linear response of the designed phase-gradient metasurface.
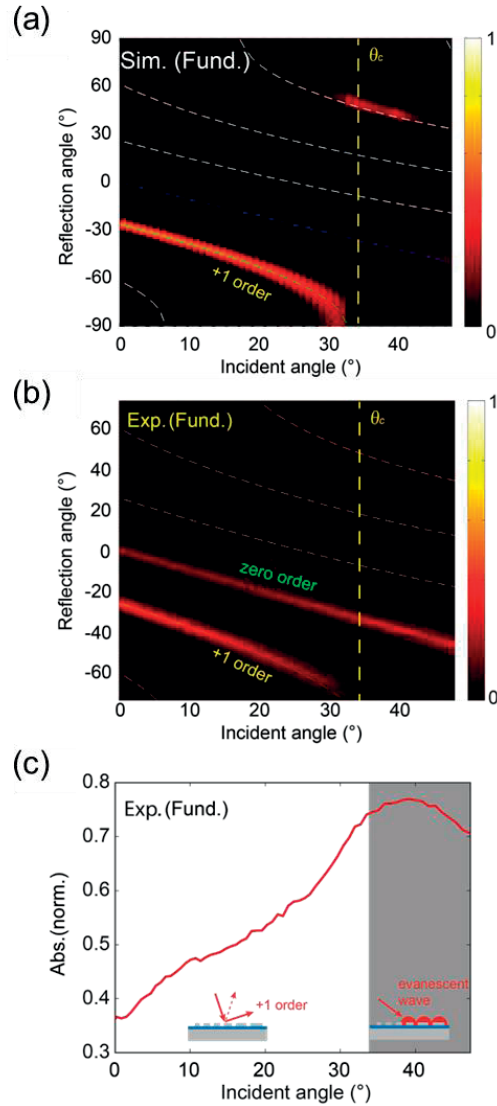
Figure 5:2 (a) simulated and (b) measured linear reflection as a function of both incident angle and reflection angle at 800 nm illumination wavelength for the phase-gradient metasurface. The green, yellow, and white dashed curves show the angular distributions of zero order, +1 order and higher diffraction orders, respectively. The yellow dashed line show the critical incident angle θ_c, for which the anomalous channel (+1 order) becomes evanescent. (c) The absorption measured as a function of incident angle. The absorption is evaluated as 1 minus the normalized reflection as there is no transmission through the metasurface.

To characterize the linear reflection as a function of the incident angle and reflection angle, we developed a linear Fourier imaging system combined with a supercontinuum light source (Fianium FemtoPower 1060) with a 60× oil immersion objective (NA is 1.45). Note that, during the measurements, the silver nanostructures face the objective and are immersed into an index-matching oil. More information on the linear measurement method can be found in section 2.4.1. The linear reflection was recorded at 800 nm wavelength as a function of the incident angle. The anomalous reflection channel corresponding to +1 diffraction order with an efficiency up to 60% can be yield under normal incidence. This channel remains the dominant contribu-

tion to the reflection until turning into an evanescent wave when the critical angle is reached as shown in Fig. 5:2. It is worth to mention that, in the phase-gradient metasurface, all the other diffraction channels are suppressed thanks to the phase distribution [103, 113, 115, 206, 238]. The weak zero order observed in the measurement might be due to small defects in the nanofabrication. For the present metasurface with a periodicity $\Lambda_x = 1200$ *nm* and an operating wavelength 800 nm, the critical incident angle is found to be $\theta_c = 34°$. The anomalous channel does not contribute to the reflection when the incident angle is greater than θ_c. At the same time, the absorption is higher when the incident angle is beyond the critical angle θ_c as shown in Fig. 5:2(c). The absorption is evaluated by 1 minus the normalized reflection collected by the objective as there is no transmission in our system. Figure 5:2(b) presents the linear reflection calculated as a function of the incident angle and the reflection angle for the phase-gradient metasurface under study. The numerical results are in very good agreement with the experimental data and illustrate again that in the linear regime, reflection corresponds to the anomalous reflection (+1 order) for illumination angles below the critical angle θ_c. For larger illumination angles, the anomalous reflection becomes evanescent and does not contribute to the far-field radiation.

5.2.2 Dispersion of excited hybrid surface plasmon wave

To study the mechanisms of the absorption enhancement in the phase-gradient metasurface, both reflection and absorption spectra associated to the anomalous channel have been calculated for incident angles between 0° and 60°, as shown in Figs. 5:3(a) and 5:3(b). First, the reflection spectrum of the anomalous channel reveals a broadband response with an optimal efficiency at the desired wavelength of 800 nm. As expected, the contribution of the anomalous beam to the far-field radiation vanishes when the incident angle becomes larger than the critical angle θ_c associated with the Wood's anomaly. Second, the absorption increases dramatically when the incident angle is beyond the Wood's anomaly line, especially within the working spectral band of the metasurface (between 750 nm and 850 nm). Third, we clearly observe that there are crossing curves with high absorption in the absorption spectrum diagram. These curves with positive and negative slopes correspond, respectively, to the dispersion of the hybrid SPP(+) and SPP(-) modes in the phase-gradient metasurface, which are well fitted with the dispersion of surface plasmon polariton (SPP) propagating along +x and –x directions on a semi-infinite silver/dielectric interface [239]. The effective refractive index of hybrid SPP(+) and SPP(-) modes are found to be 1.61, which is slightly higher than the refractive index of the background index (1.5) due to the presence of the nanostructures layer. Fourth, at 800 nm excitation wavelength, a maximum of absorption can be observed close to the dispersion curve of the hybrid SPP(+) mode owing to the resonant excitation of the anomalous reflection channel. Finally, although not expected in the case of a continuous phase gradient surface, the observation of the hybrid SPP(-) mode can be understood by considering that minor grating effects are inevitable due to the discontinuity induced by the 6-level phase distribution in the designed metasurface. In this case, the hybrid SPP(-) mode can be excited by high diffraction orders with in-plane wavevectors pointing toward the –x direction, although that backward propagating mode should be much weaker than the hybrid SPP(+) mode. For example, while the hybrid SPP(+) mode is resonantly excited by the +1 order anomalous reflection channel under 42° illumination, with slightly lower incident angle, the hybrid SPP(-) mode can be weakly excited at 800 nm by the weak -4 order diffraction channel for an incident angle around 40°, see Fig. 5:3(b).

Figures 5:3(c) and 5:3(d) show the near-field distributions in the supercell of the metasurface for illumination angles ranging from 0° to 48°. At normal incidence, the near-field intensity varies within the supercell from one nanorod to the other due to the influence of the nanorod length on the LSPRs. The near-field intensity is the highest close to the nanorods at the center of the supercell since their LSPRs are close to the pump wavelength (800 nm), see Fig. 5:4. When the hybrid SPP(+) mode is excited (illumination angle of 42°), the near-field intensity becomes more delocalized over the entire supercell, which is a clear fingerprint of a surface mode. At the same time, the near-field intensity is still the highest close to the nanorods owing to the excitation of LSPRs. These observations emphasize the hybrid nature of the excited mode [240]. The near-field distributions are in agreement with the effective wavelength of the hybrid SPP(+) mode (λ_{eff} = 479 nm) calculated using Eq. (5.1). This fact indicates that, when the illumination is such that the in-plane component of the anomalous reflection wavevector $k_{(+1)}^{\omega}$ is matched with the one for the hybrid SPP(+) mode $k_{spp(+)}^{\omega}$, the anomalous channel cannot radiate to the far-field but couple to the unidirectional hybrid SPP(+) wave propagating on the metasurface. For an illumination angle of 48°, although the anomalous reflection channel remains evanescent, the near-field features of the

hybrid mode are strongly altered due to the mismatch between excitation and hybrid SPP(+) mode dispersion. In this case, the near-field enhancement is again mainly due to the excitation of LSPRs. Note that the near-field intensity is higher than the one observed at normal incidence (compare the top and bottom panels in Fig. 5:3(c)). Having characterized the linear properties of the hybrid plasmon modes, we now turn our attention to the SHG from the phase-gradient metasurface.
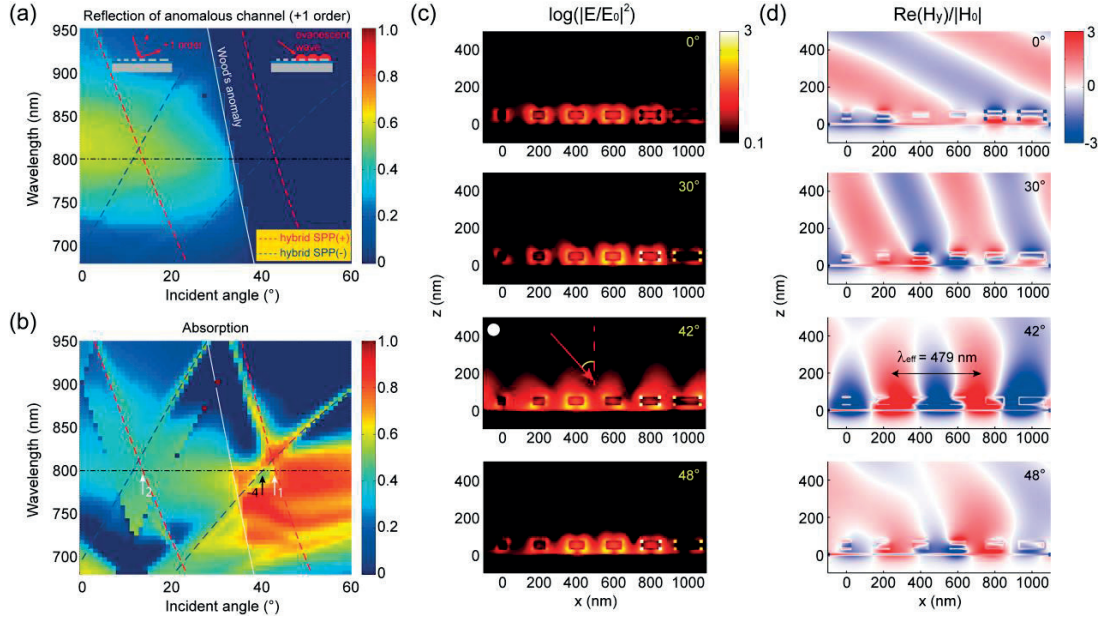
Figure 5:3 Simulated linear dispersion diagrams of (a) reflection and (b) absorption associated with the anomalous channel (+1 order). The intensity is normalized by the illumination. The Wood's anomaly line (white solid line) indicates the relation between the critical incident angle θ_c and the wavelength. The dispersion curves of the hybrid surface plasmon modes propagating along +x and -x directions are shown as red and blue dashed lines, respectively. The white arrow in the absorption diagram depicts the excitation condition of the hybrid SPP(+) under 800 nm illumination. The near-field distributions of (c) the intensity and (d) the real part of the y component of the magnetic field are shown in the (X,Z) plane of a supercell for illumination angle ranging from 0° to 48°. The near-field intensity and magnetic field are normalized to the intensity of electric field $\left|\mathbf{E}_0\right|^2$ and the amplitude of magnetic field $\left|\mathbf{H}_0\right|$ for incident light, respectively. The near-field intensity is shown in logarithmic scale. The effective wavelength of the hybrid surface plasmon mode is $\lambda_{\text{eff}} = 479$ nm, as observed for a 42° incident angle.
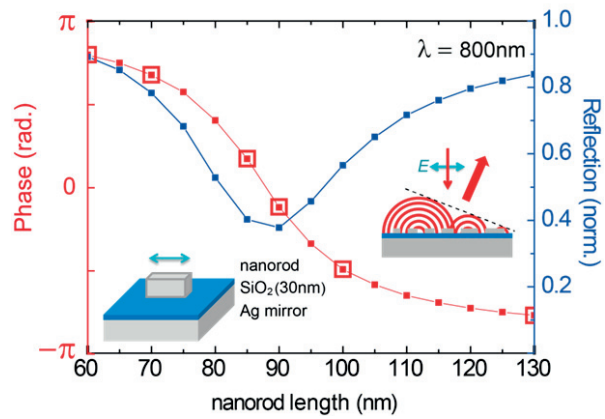
Figure 5:4 Reflection phase and intensity as functions of the nanorod length. The selected 6 different lengths: 60 nm, 70 nm, 85 nm, 90 nm, 100 nm, 130 nm are marked with red square boxes on the phase curve. In the simulation, the width and thickness of nanorod are both 40 nm. The periodicity of the square arrays of nanorods is fixed to 200 nm for both x and y directions. The refractive index of both the background and the SiO_2 spacer is 1.5.

5.3 SH emission

5.3.1 Second harmonic enhancement

To measure the SH emission as a function of the illumination angle, the home built nonlinear Fourier-plane imaging setup was used with a tunable plane-wave illumination scheme (see the method in Chapter 2). The SH intensity was measured for the same metasurface and is shown as a function of both the incident angle and the reflection angle in Fig. 5:5(a). The highest SH intensity is obtained for an illumination angle of 42°. Interestingly, in this case, the main SH emission channel is also the +1 diffraction order computed for the SH frequency. Experimentally, Fig. 5:5(c) indicates that this excitation channel produces an up to 235 fold SH intensity enhancement for incident angles close to 42°, compared with the lowest SH intensity of +1 diffraction order obtained at around 39° incidence.

As for the linear response, the computed angle dependence of the SHG is in excellent agreement with the experimental results. Indeed, a strong SH intensity is observed for the +1 SH diffraction order for illumination angles around 42°, Fig. 5:5(b). Note that, contrary to the experiments where a weak excitation of the other SH orders is observed, only the +1 order gives a significant SH intensity in the simulations. This difference is probably due to small nanofabrication defects [145]. According to the simulation, a SH enhancement up to 6 orders of magnitude is achieved when the incident angle is such that the linear hybrid SPP(+) is excited, see Fig. 5:5(d).
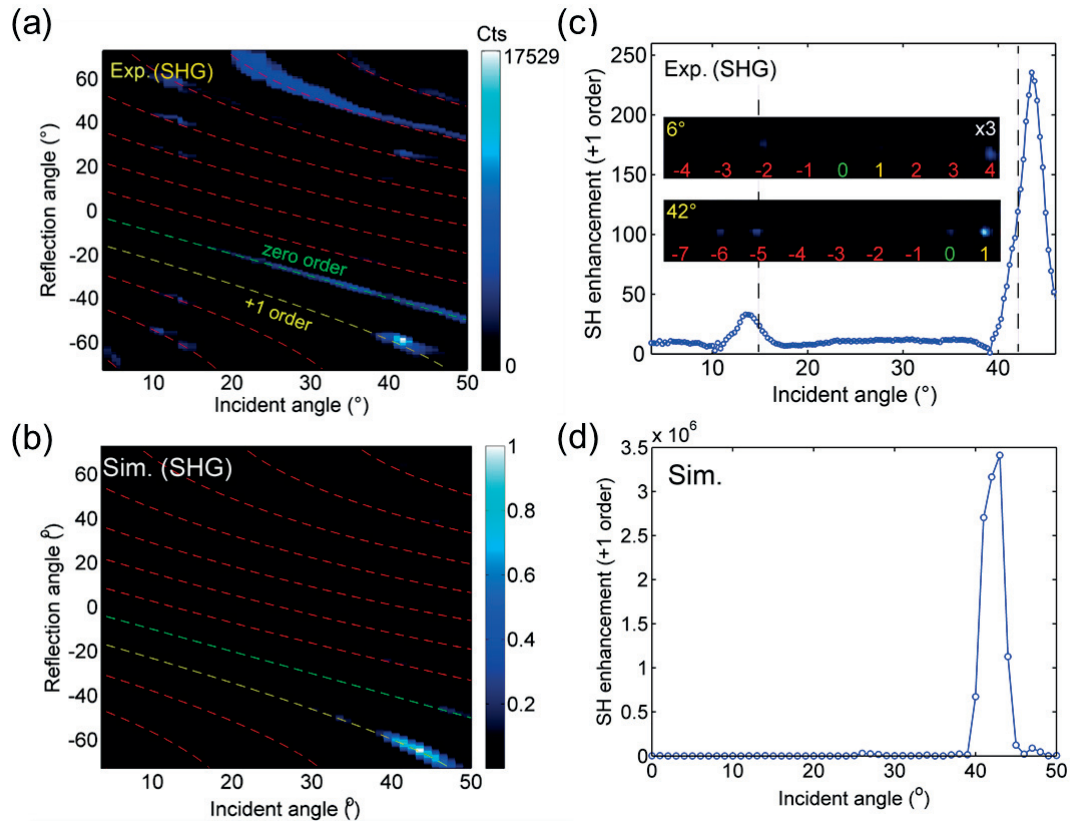
Figure 5:5 (a) measured and (b) simulated SH reflection as a function of both incident angle and reflection angle at 800 nm illumination wavelength, respectively. The green, yellow, and red dashed curve shows the angular distribution of zero order, +1 order, and higher diffraction orders, respectively. The (c) measured and (d) simulated SH enhancement as a function of incident angle for the +1-order SH emission, respectively. The SH enhancement is obtained by normalized with the lowest intensity in the corresponding plot. For the plot for the measurement (c), the left and right dashed lines show the incident angles for which the hybrid SPP(+) mode is excited by the anomalous +1 order reflection channel and the weak +2 order diffraction channels deriving from the dispersion of the hybrid SPP(+) modes. The SH emission recorded in the Fourier plane images under 6° and 42° incidences are shown in the insets. The number in the images denotes the diffraction orders at SH wavelength. In the case of 6° incident angle, the SH intensity is multiplied by 3 for visualization.
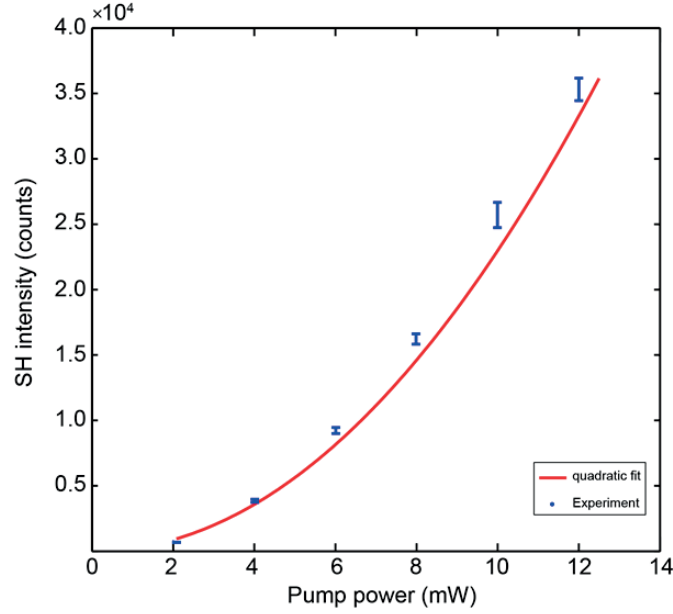
Figure 5:6 SH intensity as a function of the pump power, showing the second order nonlinearity of the recorded signal. The SH power dependence is acquired under 42° incidence.

5.3.2 Second-harmonic phase matching

To explain the observation of dominant +1-order SH emission when the hybrid SPP(+) wave is excited, it is necessary to consider the conservation of the in-plane momentum wavevector during SHG, as for the case of nonlinear reflection from flat interfaces[224, 225]. For a phase-gradient metasurface, we need to establish the relationship between the in-plane wavevector component $k_{spp(+)}^{\omega}$ of the fundamental hybrid SPP(+) mode, the metasurface phase gradient $\frac{2\pi}{\Lambda_x}$ and the wavevector of the SH +1 diffraction order $k_{//}^{2\omega}(+1)$. Here, the wavevector of the linear hybrid SPP(+) mode $k_{spp(+)}^{\omega}$ is considered instead of that of the incident wave, since the excitation of plasmonic modes is known to dramatically enhance the SHG. The linear hybrid SPP(+) mode is involved twice in the generation of the nonlinear polarization – the SH source – leading to a $2k_{spp(+)}^{\omega}$ term. However, this $2k_{spp(+)}^{\omega}$ term is larger than the free-space wavevector at the SH wavelength $k_0^{2\omega}$:

$$2k_{spp(+)}^{\omega} > k_0^{2\omega} = 2k_0^{\omega}, \tag{5.2}$$

where k_0^{ω} denotes the free-space wavevector at the excitation wavelength 800 nm. This is due to the additional momentum provided by the phase-gradient metasurface and it prevents momentums conservation between the fundamental and SH waves. However, momentum conservation can still be satisfied by reducing the momentum by subtracting one grating momentum $\frac{2\pi}{\Lambda_x}$, leading to:

$$2k_{spp(+)}^{\omega} - \frac{2\pi}{\Lambda_x} = k_{//}^{2\omega}(+1), \tag{5.3}$$

The validity of this equation is numerically confirmed for a 42° illumination angle, as presented in Fig. 5:7. Please note that although the in-plane momentum $\frac{d\Phi}{dx}$ and grating momentum $\frac{2\pi}{\Lambda_x}$ have the same quantity in our system, comparing with in-plane momentum which only has +x direction defined by the phase gradient distribution, the grating momentum can be multiplied by any integral. In summary, while the phase-gradient metasurface provides an in-plane momentum to transfer the incoming light into a hybrid plasmonic surface wave, it also plays a key role in the control of the SH emission, since the SH reflection angle also depends on the metasurface periodicity. It is worth to mention that, most of the nonlinear plasmonic metasurfaces reported so far have achieved the manipulation of nonlinear scattering light by solely applying the phase modulation at the nonlinear frequency [86-90, 241, 242]. Here, we have realized anomalous SH reflection by introducing the phase-gradient distribution at the fundamental wavelength, which can provide an efficient coupling of a unidirectional hybrid plasmon wave and result in an anomalous in-plane phase-matching condition for SHG.
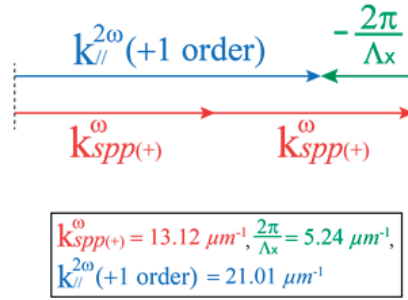
Figure 5:7 The in-plane momentum conservation condition for the linear hybrid surface plasmon mode for an illumination angle of 42°. The in-plane component of the wavevector of the hybrid surface plasmon mode is indicated as $k_{spp(+)}^{\omega}$. The SH in-plane component of wavevector of +1 diffraction order are labelled as $k_{//}^{2\omega}(+1\ order)$. The in-plane grating momentum is denoted as $\frac{2\pi}{\Lambda_x}$.

5.4 Origin of the strong SH enhancement

The phase-gradient metasurface is composed of metallic elements with different natures – the silver backplate and the silver nanorods – and it is important to determine the relative roles played by the localized and propagating plasmon modes in the SH emission. To this end, let us consider separately the linear and nonlinear responses of the nanorods and the backplate. Figure 5:8 presents the absorption in the nanorods and in the silver backplate for incident angles between 30° and 50°. For illumination angles close to 42°, a minimum of the absorption in the nanorod, as well as a maximum of the absorption in the backplate, are observed. This is the evidence of an energy transfer from the nanorods to the silver backplate induced by the excitation of the hybrid SPP(+) mode. To understand the role of this energy transfer in the nonlinear response of the phase-gradient metasurfaces, the SHG is computed using an area-selective nonlinear polarizability method, recently introduced to investigate the energy transfer occurring in DRAs [185]. In this approach, the surface nonlinear susceptibility $\chi^{(2)}$ is set to 0, except for the area of interest, either the nanorods or the backplate in the present case. Comparing the SH intensity from each constituting elements of the metasurface reveals that the silver backplate generates nearly 70% of the SH intensity as the hybrid SPP(+) mode is excited as shown in Figs. 5:8(b) and 5:8(c). This difference in the SH intensity can be explained by the symmetry of the elements. The nanorods are centrosymmetric and the SH sources standing on the nanorod surfaces tend to destructively interfere, thus limiting the nonlinear far-field radiation. At the same time, the centrosymmetry is broken over the entire backplate surface, resulting in an efficient SH emission. Furthermore, the SH sources distributed over the silver backplate surface provide a single SH emission channel corresponding to the +1 diffraction order; on the other hand, the SHG from the nanorods is spatially broad and distributed over several emission channels. This point is further emphasized in the SH near-field intensity distributions. Indeed, regular fringes can be observed in Fig. 5:8(b) for the case of SHG from the backplate, emphasizing the unidirectional nonlinear emission. These results underline the role of the fundamental hybrid SPP(+) mode in the SHG, helping to transfer the incident energy to the silver backplate, which induces a more favorable distribution of the SH sources.
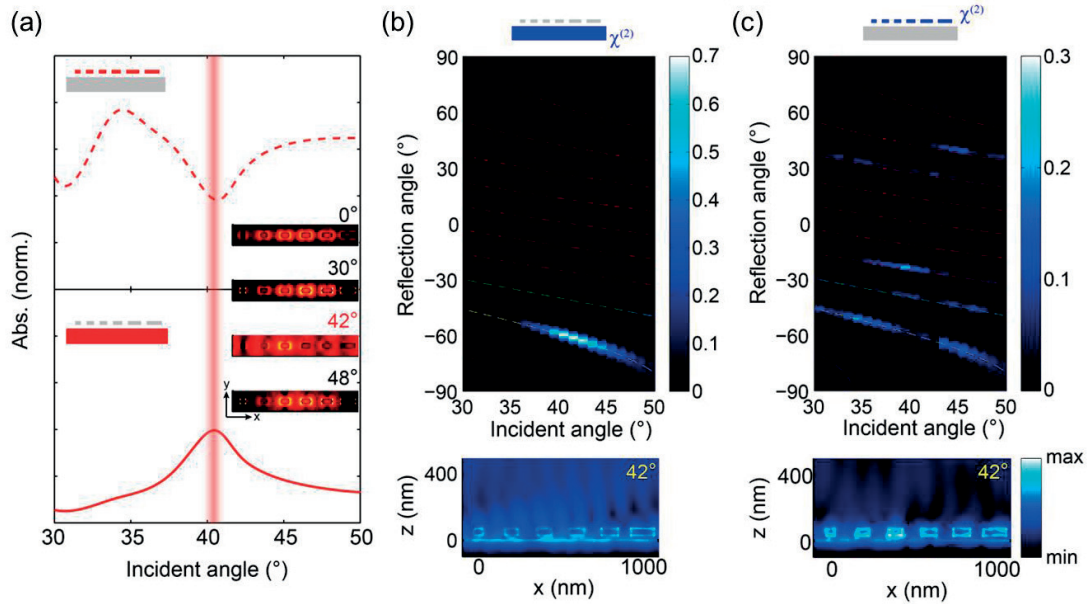
Figure 5:8 The relative roles played by the silver nanostructures and the mirror backplate in the SH emission. (a) Calculated linear absorption in the nanorods (top panel) and in the silver backplate (bottom panel) as a function of the incident angle. The energy transfer from the nanostructures to the backplate is clearly observed for incident angles leading to the excitation of the hybrid surface plasmon mode. The insets show the near-field intensity distributions in the (X,Y) plane of the supercell for incident angle ranging from 0° to 48°. (b) SH emission as a function of both the incident angle and the reflection angle (top panel) and SH near-field distribution in the (X,Z) plane for an incident angle of 42° (bottom panel) considering only the SH sources standing on the surface of the silver backplate. The nonlinear susceptibility $\chi^{(2)}$ is set to 0 at the nanorod surfaces. (c) SH emission as a function of both the incident angle and the reflection angle (top panel) and SH near-field distribution in the (X,Z) plane for an incident angle of 42° (bottom panel) considering only the SH sources standing on the surface of the silver nanorods. The nonlinear susceptibility $\chi^{(2)}$ is set to 0 at the plate surface. The near-field SH intensity distributions are presented in a logarithmic scale for clarity.

5.5 Comparison between the phase-gradient metasurface and binary-phase grating

In order to emphasize the role of the phase design in the excitation of the hybrid surface plasmon and in the strong SH generation, the optical response of the phase-gradient metasurface is compared to that of a binary-phase grating. The binary-phase grating has indeed a 2-level phase design (0 and π) and the supercell is composed of 6 silver nanorods with lengths of 80 nm, 80 nm, 80 nm, 110 nm, 110 nm, and 110 nm arranged along the x direction. Note that others geometric parameters, such as the thicknesses of the SiO_2 spacer and of the silver backplate, the height and width of the silver nanorods are kept the same as in the phase-gradient metasurface. In Figure 5:9, the simulation reveals that the reflection from the binary-phase grating corresponds to several diffraction orders, due to the phase singularity points located at the middle and at the extremities of the supercell. Anomalous reflection in the phase-gradient metasurface can efficiently excite the hybrid surface plasmon mode in the linear regime. As a result, the absorption and the near-field enhancement induced by the hybrid plasmon mode are both higher in the phase-gradient metasurface as shown in Fig. 5:9(c) and 5:9(d).

The distinct linear optical responses of the two systems results in distinct SH properties. The SH intensity is shown as a function of both the incident and the reflection angles in Fig. 5:10, demonstrating that the two metasurfaces have indeed distinct nonlinear properties. Interestingly, the SH intensity from the binary-phase grating is lower than that from the phase-gradient metasurface. Furthermore, in the binary-phase grating, the SHG is spread into several channels, in opposition to the single-channel SH emission from the phase-gradient metasurface. This is a consequence of the diffraction effect in the linear regime. In the phase-gradient metasurface, the dominant hybrid plasmon mode for an illumination angle of 42° results in +1-order SH emission as described in Fig. 5:10(c). In contrast, the binary-phase grating reveals a strong -3-order diffraction in the linear regime and then generates an additional -6-order SH emission as described in Fig. 5:10(d). In summary, the phase-gradient design in the metasurface is crucial not only for an efficient excitation of the hybrid surface plasmon wave through single-channel excitation in the linear regime, but also permits a single-channel SH emission with large enhancement.
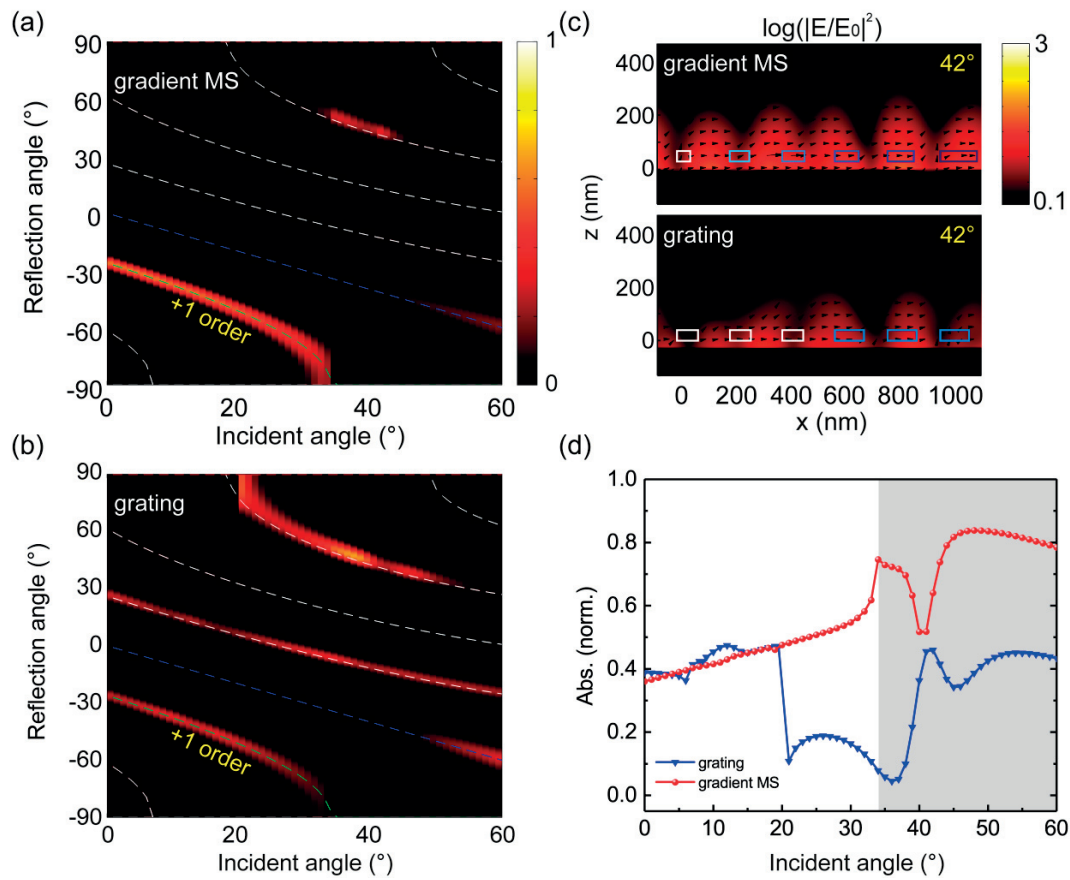
Figure 5:9 Comparison between the linear response of the phase-gradient metasurface and the binary-phase grating. The binary-phase grating is composed of 6 silver nanorods with 2 different lengths. The lengths of silver nanorods are 80 nm, 80 nm, 80nm, 110 nm, 110nm, and 110 nm along the *x* direction in order to generate a π phase shifts at 800 nm wavelength. The reflection calculated as a function of both incident angle and reflection angle for (a) the phase-gradient metasurface and (b) the grating metasurface. (c) Near-field intensity distributions, as well as the Poynting vectors (black arrows), in the (*X, Z*) plane for an illumination angle of 42° for both metasurfaces. (d)The absorption as a function of incident angle for both metasurfaces. The gray zone shows the incident angles beyond the critical angle θ_c.
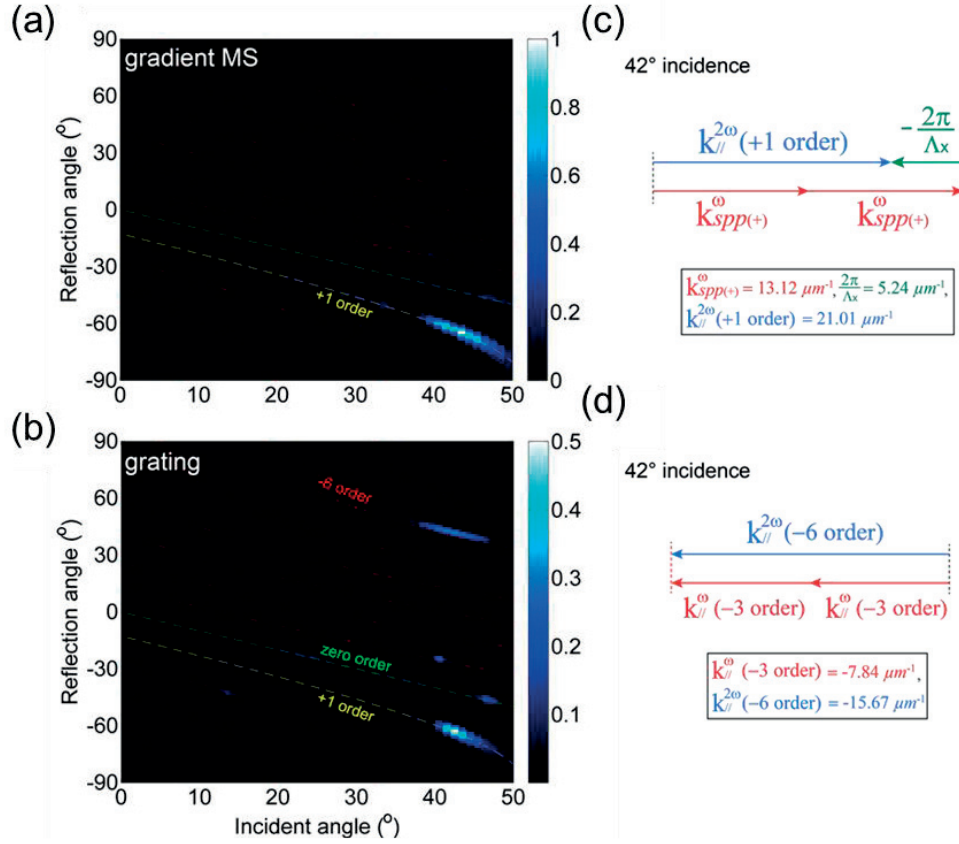
Figure 5:10 Comparison between the SHG from the phase-gradient and the binary-phase grating metasurfaces. The SH emission calculated as a function of both the incident and reflection angles for the (a) phase-gradient metasurface and (b) the grating metasurface. The in-plane momentum conservation condition for (c) the linear hybrid surface plasmon mode and (d) -3-order diffraction for an illumination angle of 42°. The in-plane component of the wavevector of the -3 diffraction order and hybrid surface plasmon mode is indicated as $k_{//}^{\omega}(-3\,order)$ and $k_{spp(+)}^{\omega}$, respectively. The SH in-plane component of wavevector of -6 diffraction order and +1 diffraction order are labelled as $k_{//}^{2\omega}(-6\,order)$ and $k_{//}^{2\omega}(+1\,order)$, respectively. The in-plane grating momentum is denoted as $\frac{2\pi}{\Lambda_x}$.

5.6 Comparison between the phase-gradient metasurface and a thin silver film

In order to emphasize the giant SHG obtained with our design metasurfaces, we experimentally compare with the SHG from a 40-nm silver film supporting propagating surface plamons at 800 nm. Impressively, with the identical measurement parameters, we observe the gradient-phase metasurface exhibits more than 80-times of SH in the reflection geometry than that from the 40-nm silver film when propagating surface plasmons are excited at 42° incidence as shown in Fig. 5:11.
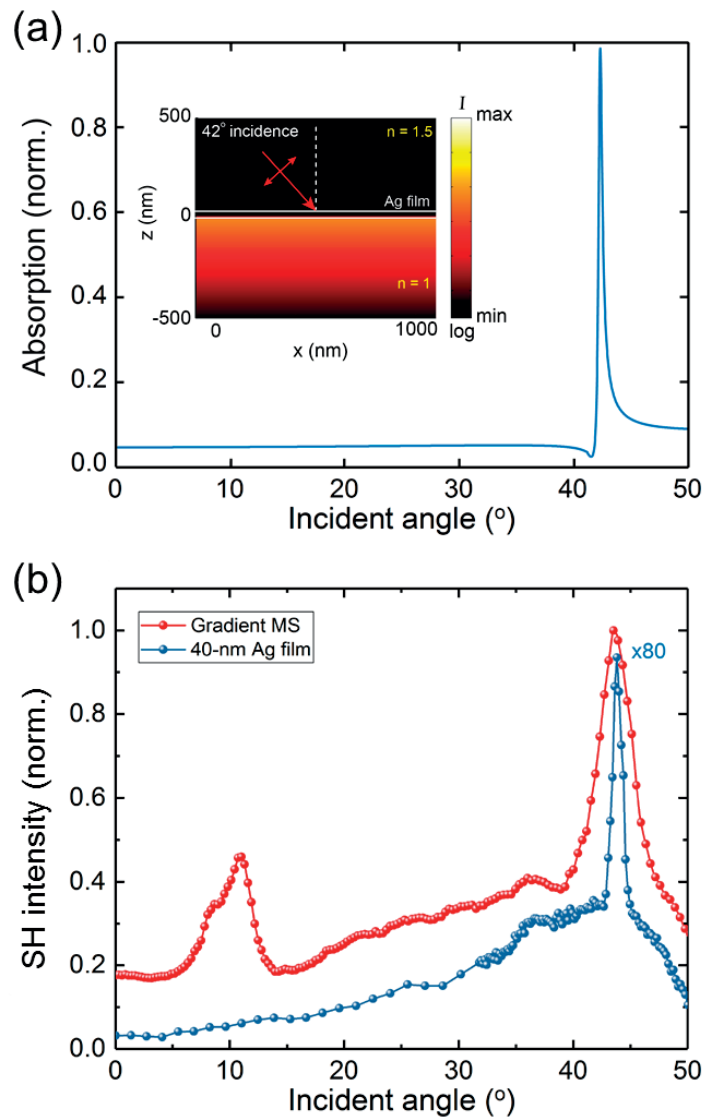
Figure 5:11 Comparison between the SHG from the phase-gradient metasurface and a 40-nm silver film. In order to excite the propagating surface plasmons on the silver thin film, the Kretschmann configuration is employed. The 40-nm silver film is illuminated by a TM-polarized illumination at 800 nm wavelength

from the side of index-matching oil with 1.5 refractive index, and an evanescent wave penetrates through the silver film can excite the surface plasmons at the air side of the film. (a) Calculated absorption as a function of incident angle for the 40-nm silver film. The inset shows the near-field distribution of the excited surface plasmons at 42° incidence. Noted that the maximum and minimum values of the color bar are set to be identical with that in others near-field plots in this work. (b) Measured SH intensity as a function of incident angle for the 40-nm silver film (blue line) and the gradient-phase metasurface (red line), respectively. The SH signal is collected by the objective. Please note that we have applied the same measurement parameters for both systems, and the obtained SH reflection for the 40-nm silver film is multiplied by 80 for comparison.

5.7 Conclusions

In this chapter, a reflective phase-gradient metasurface has been designed to convert a free propagating wave to an unidirectional hybrid SPP(+) mode supported on its silver backplate with 80% absorption efficiency under 800 nm illumination, resulting in a SHG enhancement of 235 folds in the measurement in comparison with the SH intensity obtained at an illumination angle such that only the LSPRs is excited. The mechanisms leading to this strong SH enhancement have been identified. The excitation of the fundamental hybrid SPP(+) mode was found to be important, in order to transfer the pump energy into the silver backplate. The unidirectional and confined propagation along the silver plate interface indeed boosts the in-plane light-matter interactions. At the same time, the backplate induces a favorable SH sources distribution over its surface, resulting in a single-channel nonlinear emission.

Interestingly, this nonlinear metasurface goes beyond previous works about the SH enhancement considering only LSPRs [86-90, 230]. In addition, the wavevector-selective nonlinear response in the designed phase-gradient metasurface opens up a new direction for the design of chromatic-aberration-free nonlinear metalens and metahologram by well-chosen arrangements of supercells in two in-plane directions. By loading the phase-gradient metasurface with a nonlinear medium [243, 244] or adding a quantum wells coating [210, 245], the fabrication of ultrathin nonlinear mirror with high nonlinear conversion efficiency is foreseen.

6. Conclusions and outlook

In this thesis, several plasmonic effects have been utilized in order to develop novel functionalities for light manipulation as well as to enhance the conversion efficiency for SHG using DRAs and subwavelength-thick nonlinear metasurfaces. The reported light manipulations are essentially linked to controlling of SH phase/amplitude modulation with the subwavelength spatial resolution provided by plasmonic meta-atoms. Importantly, we found that the SH response can be dramatically modified by engineering the mode dispersion at either the fundamental or SH wavelengths. Furthermore, the symmetry plays a central role for the observed SH response in all the investigated plasmonic systems.

In Chapter 3, we combine simulations and experiments to investigate in detail the role of the modes coupling in the enhancement of SHG from aluminum DRAs. By performing a comprehensive parametric study, where the geometry of the nanostructure varies, we demonstrate that SHG is enhanced when the coupling between the quadrupolar and the dipolar modes at the SH wavelength is significant. Since the quadrupolar SH mode generally found in the centrosymmetric plasmonic nanoantenna cannot efficiently couple to the far-field, the near-field plasmonic coupling effect at the SH wavelength is found critical for an efficient SH emission. Indeed, the strengthened SH near-field coupling together with enhanced SH emission has been clearly observed in the DRAs when the length of the short bar is such that the dipolar mode can be excited at the SH wavelength. In contrast, the SH field is mainly confined in the near-field when the dipolar mode is detuned from the SH wavelength by varying the short bar length. The presented tunability of the ratio of near-field to far-field intensity for SHG has great potential for practical applications such as tunable EUV nanosources, nonlinear plasmonic nanorulers, nonlinear sensing and nonlinear optical encryption.

The results reported in Chapter 3 reveal the underlying mechanisms for the enhancement of SHG from plasmonic nanostructures and establish new routes for the design of SH phase/amplitude modulation with efficient multiple resonant nanostructures. The latter is essential for the design of nonlinear metasurfaces due to the fact that the exploration of the nonlinear response meta-atoms usually plays a key role in the realization of advanced SH light manipulations. For instance, the modulation of SH emission performed by the DRAs can be useful for the phase/amplitude design of nonlinear metasurfaces capable to work under linear-polarized light illumination. Beside the required circular-polarized incident light for the nonlinear geometric Berry phase method as discussed in section 1.2.4, our system provides an alternative approach to engineering the SH phase/amplitude response under the linear-polarized incident light.

For a few decades, we are witnessing tremendous progress in nanotechnology and plasmonics is certainly a playground of choice for exploring remarkable optical phenomena enabled by the nanoscopic nature of the sample under study. Indeed, plasmonic metasurfaces have provided a framework to control light in different manners based on the wavelength, polarization, and even orbital angular momentum of incident light. While the selective response depend on the wavevector of incident light has barely been explored due to the planar configurations with a subwavelength thickness, In Chapter 4, we demonstrate experimentally a unique nonlinear three-dimensional plasmonic metasurface with a controllable wavevector-selective response for SHG, that is, the nonlinear response is highly anisotropic for various impinging directions and wavelengths of the excitation light. This truly 3D metasurface is composed of gold nanocones supporting out-of-plane plasmonic modes. The wavevector-selective coupling between the illumination field and these modes produce a nonlinear response that depends on the illumination direction, thus providing directionality control over the SH emission. Let us note that this wavevector-selective nonlinear response cannot be realized in purely planar nanostructures, which generally do not exhibit inhomogeneous reflection with respect to the wavevector (i.e. the incident angle) of the incoming light. Here, we combine both experiments and simulations to reveal the mechanisms that lead to a wavevector-selective nonlinear response and discuss in detail how the corresponding selection rule can be engineered by controlling the tilt angle of the gold nanocones on the surface. Remarkably, although the response of the system is determined by its individual components (the nanocones), the overall system behaves as a homogeneous metasurface with only specular SH reflection.

A key innovation in the presented work is the utilization of a particular type of 3D plasmonic nanostructures to provide out-of-plane nonlinear polarizability, such that different SH polarizations are generated for different incident wavevectors at the fundamental wavelength. Particularly, this wavevector-selective response is realized in the homogeneous plasmonic arrays with subwavelength device thickness, which can hardly be achieved by conventional optical components due to the requirement of a sufficient phase accumulation. Together, this work paves the way for an optimal design of directional nonlinear plasmonic meta-mirrors.

In order to generate an arbitrary wavefront of light, the continuous and spatially varying phase/amplitude modulation with the subwavelength resolution along the artificial interface is required according to the Huygens's principle. With the design principle of wavefront construction, plasmonic metasurfaces have opened up a revolutionary way to freely manipulate light with accessible phase/amplitude control of electromagnetic wave with subwavelength domains. This advanced diffraction-free light manipulation permits a high-efficiency tailoring of a propagating wave into a hybrid surface plasmon wave supported on the metallic backplate of metasurface, resulting in a strongly enhanced near-field. The enhanced near-field and the variation of local symmetry from that of LSPR modes are *per se* interesting for SHG. Yet, most nonlinear metasurfaces reported so far are solely relied on the LSPRs to coherently shaping the wavefront of SH emission. Despite that, the limited light harvesting from the radiation loss of LSPR modes at the excitation stage will hamper the overall efficiency of SHG.

In Chapter 5, we experimentally demonstrate the first observation of giant enhancement and high directionality of SH emission from an excited hybrid localized and propagating surface wave in a reflective phase-gradient metasurface. The gradient-phase design provides an in-plane momentum to the incoming light and thus enables to direct the reflected beam into an

anomalous channel following the generalized Snell's law. The anomalous refection in the far-field is contributed by the overall radiation loss of LSPR modes in the metasurface. This radiation loss can be significantly reduced when the incident angle is such that the anomalous reflection channel can be tailored into a hybrid surface plasmon wave confined and in-plane propagating on the metallic backplate of the designed metasurface. This fact emphasizes the novelty of our designed metasurface which enables the possibility to tailor the incident plane wave into a non-radiative hybrid SPP(+) channel supported by the implemented metallic backplate (30-nm beneath the nanorod layer). Indeed, with an appropriated incident angle, the anomalous channel can be tailored into the hybrid surface plasmon wave propagating along the phase-gradient direction on the metasurface. In this case, we experimentally observed a maximum absorption peak with nearly 80% absorption efficiency at 800 nm illumination, almost twice the value at normal incidence. Impressively, a SHG enhancement of 235 folds is experimentally observed with respect to that when only the LSPRs are excited. Interestingly, the single-channel SH emission with high directionality can be clearly observed when the hybrid surface plasmon wave is excited. Importantly, this well-defined SH emission is facilitated by the SH quasi-phase-matching between the SH emission channel and the excited hybrid surface plasmon wave. Besides, the role of the nanorods and metallic backplate for SHG has been carefully addressed thanks to the area-selective nonlinearity method in SIE simulation. When the hybrid surface plasmon wave is excited, the observed energy transfer from the nanoantenna to the metallic backplate at the fundamental wavelength, together with the dominant contribution of SHG from the metallic backplate, indicates that the propagating SPP component plays a key role in the leading giant SH enhancement as well as the high directionality of SH emission.

The key innovation in Chapter 5 is the utilization of a unidirectional hybrid surface plasmon wave as a fundamental driven source of SHG. In comparison with the conventional nonlinear metasurfaces using only LSPR elements, the excitation of non-radiative hybrid surface plasmon mode can further improve the light harvesting by confining the anomalous reflection light on the metallic backplate of the designed metasurface. Moreover, the excited unidirectional propagating surface wave is certainly favorable for various kinds of light-matter interactions at the interface, since this scheme allows the optical response to gradually build up with the in-plane distance along the propagating direction of the hybrid surface wave. For example, if there is a properly designed metasurface supports a unidirectional hybrid surface plasmon modes at both the fundamental and SH wavelengths in the way such that the SH phase-matching condition between these two surface propagating modes can be satisfied, the linear growth of SH intensity for the SH surface waves along the in-plane propagating direction can be foreseen. The idea of in-plane phase matching with the two propagating surface-plasmon waves has been proposed in a nonlinear plasmonic waveguide which exhibits an intriguing backward phase-matching condition for SHG [246]. However, in this proposed system, the quadratic SH intensity growth along the planar plasmonic device has not yet been clearly demonstrated due to the high loss of the supported SH surface mode. In their design, the excitation of propagating surface plasmon is achieved by focusing the illumination light on an open slit in the metal-dielectric-metal plasmonic waveguides. In contrast, our designed metasurface can excite the unidirectional hybrid surface waves in the whole illuminated area and thus provide better light harvesting. Consequently, with the further investigation of mode dispersion for the hybrid surface waves at the SH wavelength, we expect an emergence of the novel in-plane phase-matching device to boost the SH efficiency along the surface in the subwavelength-thick nonlinear metasurfaces. On the other

hand, the excited hybrid surface plasmon wave provides a strongly enhanced and delocalized near-field distributed over the entire plasmonic metasurfaces. This unique characteristic is highly desirable for the enlargement of the optical response of molecules approaching the metasurfaces, facilitating the light-matter interaction [247]. Therefore, besides the efficiency enhancement of nonlinear optical processes, this work also paves a way for the optimal design for practical applications in plasmonic sensing [248], photochemical reactions [249], catalytic reaction [250] and light trapping in thin-film solar cells [251-253].

In this thesis, we mainly focused on the SHG from nanostructures made of noble plasmonic metals due to the interests of strong near-field enhancement and fascinating symmetry selection rules with plasmonic effects involved. Due to the LSPR enhancement plasmonic nanoparticles can indeed generate relatively efficient SH emission with deep subwavelength dimensions. However, due to the loss issues in the metals, the resulting heating effects will eventually constrain the optical damage threshold for the plasmonic systems. These effects will limit the overall conversion efficiency of SHG which should be scaled up with the pump power like a second-order nonlinear process. To overcome this issue, dielectric/semiconductor nonlinear materials with a high refractive index will be highly desirable to sustain a higher damage threshold while remaining the ultrathin device thickness [254, 255]. In comparison with plasmonic nanoparticles, dielectric/semiconductor nanoparticles can support magnetic dipole modes with field mainly confined in the bulk instead of the surface of the nanoparticles, thus noncentrosymmetric materials are required for SHG from the bulk [256, 257]. By replacing the materials from noble metals to nonlinear materials while employing the design principle of phase-gradient metasurfaces proposed in this thesis, further improvements of SH conversion efficiency can be foreseen thanks to a higher input-power tolerance for such all-dielectric nonlinear metasurfaces.

Bibliography

[1]   T. H. Maiman, "Stimulated Optical Radiation in Ruby," *Nature* 187, 493-494 (1960).

[2]   P. A. Franken, A. E. Hill, C. W. Peters, and G. Weinreich, "Generation of Optical Harmonics," *Phys. Rev. Lett.* 7, 118-119 (1961).

[3]   R. W. Boyd, *Nonlinear Optics* (Academic Press, 1992).

[4]   Y. R. Shen, *The Principles of Nonlinear Optics* (Wiley, 1984).

[5]   J. Larmor, "On the Theory of the Magnetic Influence on Spectra; and on the Radiation from Moving Ions," *Philos. Mag.* 44, 503-512 (1897).

[6]   M. A. Persaurd, J. M. Tolchard, and A. I. Ferguson, "Efficient Generation of Picosecond Pulses at 243nm," *IEEE J. Quantum Electron.* 26, 109-124 (1990).

[7]   A. Ashkin, G. Boyd, and J. Dziedzic, "Resonant Optical Second Harmonic Generation and Mixing," IEEE J. Quantum Electron. 2, 1253-1258 (1966).

[8]   W. Kaiser, and C. G. B. Garrett, "Two-Photon Excitation in Caf2: Eu2+," Phys. Rev. Lett. 7, 229-231 (1961).

[9]   K. Kamada, K. Ohta, T. Kubo, A. Shimizu, Y. Morita, K. Nakasuji, R. Kishi, S. Ohta, S.-i. Furukawa, H. Takahashi, and M. Nakano, "Strong Two-Photon Absorption of Singlet Diradical Hydrocarbons," Angew. Chem. Int. Ed. 46, 3544-3546 (2007).

[10]   N. Bloembergen, "Nonlinear Laser Spectroscopy," Ann. N.Y. Acad. Sci. 267, 51-60 (1976).

[11]   F. Biraben, B. Cagnac, and G. Grynberg, "Experimental Evidence of Two-Photon Transition without Doppler Broadening," Phys. Rev. Lett. 32, 643-645 (1974).

[12]   M. D. Levenson, and N. Bloembergen, "Observation of Two-Photon Absorption without Doppler Broadening on the 3s-5s Transition in Sodium Vapor," Phys. Rev. Lett. 32, 645-648 (1974).

[13]   J. E. Bjorkholm, and P. F. Liao, "Resonant Enhancement of Two-Photon Absorption in Sodium Vapor," Phys. Rev. Lett. 33, 128-131 (1974).

[14]   P. F. Curley, A. I. Ferguson, J. G. White, and W. B. Amos, "Application of a Femtosecond Self-Sustaining Mode-Locked Ti:Sapphire Laser to the Field of Laser Scanning Confocal Microscopy," Opt. Quantum Electron. 24, 851-859 (1992).

[15]   P. J. Campagnola, M.-d. Wei, A. Lewis, and L. M. Loew, "High-Resolution Nonlinear Optical Imaging of Live Cells by Second Harmonic Generation," *Biophys. J.* 77, 3341-3349 (1999).

[16] Müller, Squier, Wilson, and Brakenhoff, "3d Microscopy of Transparent Objects Using Third-Harmonic Generation," *Journal of Microscopy* 191, 266-274 (1998).

[17] D. Yelin, and Y. Silberberg, "Laser Scanning Third-Harmonic-Generation Microscopy in Biology," *Opt. Express* 5, 169-175 (1999).

[18] W. R. Zipfel, R. M. Williams, and W. W. Webb, "Nonlinear Magic: Multiphoton Microscopy in the Biosciences," *Nat Biotech* 21, 1369-1377 (2003).

[19] W. Denk, J. Strickler, and W. Webb, "Two-Photon Laser Scanning Fluorescence Microscopy," *Science* 248, 73-76 (1990).

[20] R. Gauderon, P. B. Lukins, and C. J. R. Sheppard, "Three-Dimensional Second-Harmonic Generation Imaging with Femtosecond Laser Pulses," *Opt. Lett.* 23, 1209-1211 (1998).

[21] N. Bloembergen, R. K. Chang, S. S. Jha, and C. H. Lee, "Optical Second-Harmonic Generation in Reflection from Media with Inversion Symmetry," *Physical Review* 178, 1528-1528 (1969).

[22] V. Mizrahi, and J. E. Sipe, "Phenomenological Treatment of Surface Second-Harmonic Generation," *J. Opt. Soc. Am. B* 5, 660-667 (1988).

[23] Y. R. Shen, "Optical Second Harmonic Generation at Interfaces," *Annu. Rev. Phys. Chem.* 40, 327-350 (1989).

[24] J. E. Midwinter, and J. Warner, "The Effects of Phase Matching Method and of Uniaxial Crystal Symmetry on the Polar Distribution of Second-Order Non-Linear Optical Polarization," *Br. J. Appl. Phys.* 16, 1135 (1965).

[25] J. A. Armstrong, N. Bloembergen, J. Ducuing, and P. S. Pershan, "Interactions between Light Waves in a Nonlinear Dielectric," *Physical Review* 127, 1918-1939 (1962).

[26] Y. R. Shen, "Surface Properties Probed by Second-Harmonic and Sum-Frequency Generation," *Nature* 337, 519-525 (1989).

[27] P. Guyot-Sionnest, W. Chen, and Y. R. Shen, "General Considerations on Optical Second-Harmonic Generation from Surfaces and Interfaces," *Phys. Rev. B* 33, 8254-8263 (1986).

[28] P. Guyot-Sionnest, and Y. R. Shen, "Local and Nonlocal Surface Nonlinearities for Surface Optical Second-Harmonic Generation," *Phys. Rev. B* 35, 4420-4426 (1987).

[29] H. W. K. Tom, and G. D. Aumiller, "Observation of Rotational Anisotropy in the Second-Harmonic Generation from a Metal Surface," *Phys. Rev. B* 33, 8818-8821 (1986).

[30]   T. F. Heinz, M. M. T. Loy, and W. A. Thompson, "Study of Si(111) Surfaces by Optical Second-Harmonic Generation: Reconstruction and Surface Phase Transformation," *Phys. Rev. Lett.* 54, 63-66 (1985).

[31]   J. M. Chen, J. R. Bower, C. S. Wang, and C. H. Lee, "Optical Second-Harmonic Generation from Submonolayer Na-Covered Ge Surfaces," *Optics Communications* 9, 132-134 (1973).

[32]   H. W. K. Tom, C. M. Mate, X. D. Zhu, J. E. Crowell, T. F. Heinz, G. A. Somorjai, and Y. R. Shen, "Surface Studies by Optical Second-Harmonic Generation: The Adsorption of O_2, Co, and Sodium on the Rh(111) Surface," *Phys. Rev. Lett.* 52, 348-351 (1984).

[33]   E. V. Sitzmann, and K. B. Eisenthal, "Picosecond Dynamics of a Chemical Reaction at the Air-Water Interface Studied by Surface Second Harmonic Generation," *The Journal of Physical Chemistry* 92, 4579-4580 (1988).

[34]   S. R. Meech, and K. Yoshihara, "Time-Resolved Surface Second Harmonic Generation: A Test of the Method and Its Application to Picosecond Isomerization in Adsorbates," *The Journal of Physical Chemistry* 94, 4913-4920 (1990).

[35]   D. A. Higgins, M. B. Abrams, S. K. Byerly, and R. M. Corn, "Resonant Second Harmonic Generation Studies of P-Nitrophenol Adsorption at Condensed-Phase Interfaces," *Langmuir* 8, 1994-2000 (1992).

[36]   A. Castro, K. Bhattacharyya, and K. B. Eisenthal, "Energetics of Adsorption of Neutral and Charged Molecules at the Air/Water Interface by Second Harmonic Generation: Hydrophobic and Solvation Effects," *The Journal of Chemical Physics* 95, 1310-1315 (1991).

[37]   O. Sato, R. Baba, K. Hashimoto, and A. Fujishima, "Coherent Interferometric Analysis of the Molecular Orientation Based on the Study of the Optical Second Harmonic Generation," *J. Electroanal. Chem. Interfacial Electrochem.* 306, 291-296 (1991).

[38]   I. Freund, and M. Deutsch, "Second-Harmonic Microscopy of Biological Tissue," *Opt. Lett.* 11, 94-96 (1986).

[39]   M. A. van der Veen, V. K. Valev, T. Verbiest, and D. E. De Vos, "In Situ Orientation-Sensitive Observation of Molecular Adsorption on a Liquid/Zeolite Interface by Second-Harmonic Generation," *Langmuir* 25, 4256-4261 (2009).

[40]   T. Rasing, J. Huang, A. Lewis, T. Stehlin, and Y. R. Shen, "In Situ," *Phys. Rev. A* 40, 1684-1687 (1989).

[41]   C. Guo, G. Rodriguez, and A. J. Taylor, "Ultrafast Dynamics of Electron Thermalization in Gold," *Phys. Rev. Lett.* 86, 1638-1641 (2001).

[42] C. V. Shank, R. Yen, and C. Hirlimann, "Femtosecond-Time-Resolved Surface Structural Dynamics of Optically Excited Silicon," *Phys. Rev. Lett.* 51, 900-902 (1983).

[43] C. K. Chen, A. R. B. de Castro, and Y. R. Shen, "Surface-Enhanced Second-Harmonic Generation," *Phys. Rev. Lett.* 46, 145-148 (1981).

[44] A. Otto, "Excitation of Nonradiative Surface Plasma Waves in Silver by the Method of Frustrated Total Reflection," *Zeitschrift für Physik A Hadrons and nuclei* 216, 398-410 (1968).

[45] E. Kretschmann, and H. Raether, "Notizen: Radiative Decay of Non Radiative Surface Plasmons Excited by Light," in *Zeitschrift für Naturforschung A*(1968), p. 2135.

[46] H. Raether, *Surface Plasmons on Smooth and Rough Surfaces and on Gratings* (Springer Berlin Heidelberg, 1988).

[47] M. Song, J. Dellinger, O. Demichel, M. Buret, G. Colas Des Francs, D. Zhang, E. Dujardin, and A. Bouhelier, "Selective Excitation of Surface Plasmon Modes Propagating in Ag Nanowires," *Opt. Express* 25, 9138-9149 (2017).

[48] E. Kretschmann, and H. Raether, "Radiative Decay of Non-Radiative Surface Plasmons Excited by Light," *Z. Naturforsch. A* 23, 2135 (1968).

[49] H. J. Simon, D. E. Mitchell, and J. G. Watson, "Optical Second-Harmonic Generation with Surface Plasmons in Silver Films," *Phys. Rev. Lett.* 33, 1531-1534 (1974).

[50] A. V. Zayats, and I. I. Smolyaninov, "Near-Field Photonics: Surface Plasmon Polaritons and Localized Surface Plasmons," *J. Opt. A: Pure Appl. Opt.* , S16 (2003).

[51] J. I. Dadap, J. Shan, K. B. Eisenthal, and T. F. Heinz, "Second-Harmonic Rayleigh Scattering from a Sphere of Centrosymmetric Material," *Phys. Rev. Lett.* 83, 4045-4048 (1999).

[52] J. I. Dadap, J. Shan, and T. F. Heinz, "Theory of Optical Second-Harmonic Generation from a Sphere of Centrosymmetric Material: Small-Particle Limit," *J. Opt. Soc. Am. B* 21, 1328-1347 (2004).

[53] F. W. Vance, B. I. Lemon, and J. T. Hupp, "Enormous Hyper-Rayleigh Scattering from Nanocrystalline Gold Particle Suspensions," *The Journal of Physical Chemistry B* 102, 10091-10093 (1998).

[54] D. Staedler, T. Magouroux, R. Hadji, C. Joulaud, J. Extermann, S. Schwung, S. Passemard, C. Kasparian, G. Clarke, M. Gerrmann, R. Le Dantec, Y. Mugnier, D. Rytz, D. Ciepielewski, C. Galez, S. Gerber-Lemaire, L. Juillerat-Jeanneret, L. Bonacina, and J.-P. Wolf, "Harmonic Nanocrystals for Biolabeling: A Survey of Optical Properties and Biocompatibility," *ACS Nano* 6, 2542-2549 (2012).

[55]   C. Langhammer, M. Schwind, B. Kasemo, and I. Zorić, "Localized Surface Plasmon Resonances in Aluminum Nanodisks," *Nano Lett.* 8, 1461-1471 (2008).

[56]   M. W. Knight, N. S. King, L. Liu, H. O. Everitt, P. Nordlander, and N. J. Halas, "Aluminum for Plasmonics," *ACS Nano* 8, 834-840 (2014).

[57]   H. U. Yang, J. D'Archangel, M. L. Sundheimer, E. Tucker, G. D. Boreman, and M. B. Raschke, "Optical Dielectric Function of Silver," *Phys. Rev. B* 91, 235137 (2015).

[58]   D. Krause, C. W. Teplin, and C. T. Rogers, "Optical Surface Second Harmonic Measurements of Isotropic Thin-Film Metals: Gold, Silver, Copper, Aluminum, and Tantalum," *J. Appl. Phys.* 96, 3626-3634 (2004).

[59]   M. Castro-Lopez, D. Brinks, R. Sapienza, and N. F. van Hulst, "Aluminum for Nonlinear Plasmonics: Resonance-Driven Polarized Luminescence of Al, Ag, and Au Nanoantennas," *Nano Lett.* 11, 4674-4678 (2011).

[60]   K. Thyagarajan, S. Rivier, A. Lovera, and O. J. F. Martin, "Enhanced Second-Harmonic Generation from Double Resonant Plasmonic Antennae," *Opt. Express* 20, 12860-12865 (2012).

[61]   B. Metzger, L. Gui, J. Fuchs, D. Floess, M. Hentschel, and H. Giessen, "Strong Enhancement of Second Harmonic Emission by Plasmonic Resonances at the Second Harmonic Wavelength," *Nano Lett.* 15, 3917-3922 (2015).

[62]   E. C. Hao, G. C. Schatz, R. C. Johnson, and J. T. Hupp, "Hyper-Rayleigh Scattering from Silver Nanoparticles," *The Journal of Chemical Physics* 117, 5963-5966 (2002).

[63]   H. Aouani, M. Navarro-Cia, M. Rahmani, T. P. H. Sidiropoulos, M. Hong, R. F. Oulton, and S. A. Maier, "Multiresonant Broadband Optical Antennas as Efficient Tunable Nanosources of Second Harmonic Light," *Nano Lett.* (2012).

[64]   M. Celebrano, X. Wu, M. Baselli, S. Großmann, P. Biagioni, A. Locatelli, C. De Angelis, G. Cerullo, R. Osellame, B. Hecht, L. Duò, F. Ciccacci, and M. Finazzi, "Mode Matching in Multiresonant Plasmonic Nanoantennas for Enhanced Second Harmonic Generation," *Nat. Nanotech.* 10, 412–417 (2015).

[65]   K. Thyagarajan, J. Butet, and O. J. F. Martin, "Augmenting Second Harmonic Generation Using Fano Resonances in Plasmonic Systems," *Nano Lett.* 13, 1847-1851 (2013).

[66]   G. D. Bernasconi, J. Butet, and O. J. F. Martin, "Mode Analysis of Second-Harmonic Generation in Plasmonic Nanostructures," *J. Opt. Soc. Am. B* 33, 768-779 (2016).

[67]   M. Ethis de Corny, N. Chauvet, G. Laurent, M. Jeannin, L. Olgeirsson, A. Drezet, S. Huant, G. Dantelle, G. Nogues, and G. Bachelier, "Wave-Mixing Origin and Optimization in Single and Compact Aluminum Nanoantennas," *ACS Photonics* 3, 1840-1846 (2016).

[68]   F. X. Wang, F. J. Rodríguez, W. M. Albers, R. Ahorinta, J. E. Sipe, and M. Kauranen, "Surface and Bulk Contributions to the Second-Order Nonlinear Optical Response of a Gold Film," *Phys. Rev. B* 80, 233402 (2009).

[69]   G. Bachelier, J. Butet, I. Russier-Antoine, C. Jonin, E. Benichou, and P. F. Brevet, "Origin of Optical Second-Harmonic Generation in Spherical Gold Nanoparticles: Local Surface and Nonlocal Bulk Contributions," *Phys. Rev. B* 82, 235403 (2010).

[70]   J. Butet, P.-F. Brevet, and O. J. F. Martin, "Optical Second Harmonic Generation in Plasmonic Nanostructures: From Fundamental Principles to Advanced Applications," *ACS Nano* 9, 10545-10562 (2015).

[71]   J. Butet, J. Duboisset, G. Bachelier, I. Russier-Antoine, E. Benichou, C. Jonin, and P.-F. Brevet, "Optical Second Harmonic Generation of Single Metallic Nanoparticles Embedded in a Homogeneous Medium," *Nano Lett.* 10, 1717-1721 (2010).

[72]   H. Husu, R. Siikanen, J. Mäkitalo, J. Lehtolahti, J. Laukkanen, M. Kuittinen, and M. Kauranen, "Metamaterials with Tailored Nonlinear Optical Response," *Nano Lett.* 12, 673-677 (2012).

[73]   R. Czaplicki, M. Zdanowicz, K. Koskinen, J. Laukkanen, M. Kuittinen, and M. Kauranen, "Dipole Limit in Second-Harmonic Generation from Arrays of Gold Nanoparticles," *Opt. Express* 19, 26866-26871 (2011).

[74]   S. Kujala, B. K. Canfield, M. Kauranen, Y. Svirko, and J. Turunen, "Multipole Interference in the Second-Harmonic Optical Radiation from Gold Nanoparticles," *Phys. Rev. Lett.* 98 (2007).

[75]   K. C. Brian, K. Sami, J. Konstantins, S. Yuri, T. Jari, and K. Martti, "A Macroscopic Formalism to Describe the Second-Order Nonlinear Optical Response of Nanostructures," *J. Opt. A: Pure Appl. Opt.* 8, S278 (2006).

[76]   S. Kujala, B. K. Canfield, M. Kauranen, Y. Svirko, and J. Turunen, "Multipolar Analysis of Second-Harmonic Radiation from Gold Nanoparticles," *Opt. Express* 16, 17196-17208 (2008).

[77]   M. W. Klein, C. Enrich, M. Wegener, and S. Linden, "Second-Harmonic Generation from Magnetic Metamaterials," *Science* 313, 502-504 (2006).

[78]   C. Ciracì, E. Poutrina, M. Scalora, and D. R. Smith, "Origin of Second-Harmonic Generation Enhancement in Optical Split-Ring Resonators," *Phys. Rev. B* 85, 201403 (2012).

[79]   S. Linden, F. B. P. Niesler, J. Förstner, Y. Grynko, T. Meier, and M. Wegener, "Collective Effects in Second-Harmonic Generation from Split-Ring-Resonator Arrays," *Phys. Rev. Lett.* 109, 015502 (2012).

[80]   A. Slablab, L. Le Xuan, M. Zielinski, Y. de Wilde, V. Jacques, D. Chauvat, and J. F. Roch, "Second-Harmonic Generation from Coupled Plasmon Modes in a Single Dimer of Gold Nanospheres," *Opt. Express* 20, 220-227 (2012).

[81]   J. Berthelot, G. Bachelier, M. Song, P. Rai, G. Colas des Francs, A. Dereux, and A. Bouhelier, "Silencing and Enhancement of Second-Harmonic Generation in Optical Gap Antennas," *Opt. Express* 20, 10498-10508 (2012).

[82]   B. K. Canfield, H. Husu, J. Laukkanen, B. Bai, M. Kuittinen, J. Turunen, and M. Kauranen, "Local Field Asymmetry Drives Second-Harmonic Generation in Noncentrosymmetric Nanodimers," *Nano Lett.* 7, 1251-1255 (2007).

[83]   D. de Ceglia, M. A. Vincenti, C. De Angelis, A. Locatelli, J. W. Haus, and M. Scalora, "Role of Antenna Modes and Field Enhancement in Second Harmonic Generation from Dipole Nanoantennas," *Opt. Express* 23, 1715-1729 (2015).

[84]   Y. Zhang, N. K. Grady, C. Ayala-Orozco, and N. J. Halas, "Three-Dimensional Nanostructures as Highly Efficient Generators of Second Harmonic Light," *Nano Lett.* 11, 5519-5523 (2011).

[85]   J. Butet, G. D. Bernasconi, M. Petit, A. Bouhelier, C. Yan, O. J. F. Martin, B. Cluzel, and O. Demichel, "Revealing a Mode Interplay That Controls Second-Harmonic Radiation in Gold Nanoantennas," *ACS Photonics* (2017).

[86]   N. Segal, S. Keren-Zur, N. Hendler, and T. Ellenbogen, "Controlling Light with Metamaterial-Based Nonlinear Photonic Crystals," *Nature Photonics* 9, 180-184 (2015).

[87]   W. Ye, F. Zeuner, X. Li, B. Reineke, S. He, C.-W. Qiu, J. Liu, Y. Wang, S. Zhang, and T. Zentgraf, "Spin and Wavelength Multiplexed Nonlinear Metasurface Holography," *Nature Commun.* 7 (2016).

[88]   S. Keren-Zur, O. Avayu, L. Michaeli, and T. Ellenbogen, "Nonlinear Beam Shaping with Plasmonic Metasurfaces," *ACS Photonics* 3, 117-123 (2016).

[89]   G. Li, S. Chen, N. Pholchai, B. Reineke, P. W. H. Wong, E. Y. B. Pun, K. W. Cheah, T. Zentgraf, and S. Zhang, "Continuous Control of the Nonlinearity Phase for Harmonic Generations," *Nature Mater.* 14, 607-612 (2015).

[90]   M. Tymchenko, J. S. Gomez-Diaz, J. Lee, N. Nookala, M. A. Belkin, and A. Alù, "Gradient Nonlinear Pancharatnam-Berry Metasurfaces," *Phys. Rev. Lett.* 115, 207403 (2015).

[91]   C. Huygens, P. v. d. Aa, and G. C. Romano, *Traite De La Lumiere* (chez Pierre Vander Aa marchand libraire, 1690).

[92]   N. Yu, and F. Capasso, "Flat Optics with Designer Metasurfaces," *Nat. Mater.* 13, 139-150 (2014).

[93] A. V. Kildishev, A. Boltasseva, and V. M. Shalaev, "Planar Photonics with Metasurfaces," *Science* 339 (2013).

[94] H.-H. Hsiao, C. H. Chu, and D. P. Tsai, "Fundamentals and Applications of Metasurfaces," *Small Methods* 1, 1600064 (2017).

[95] A. E. H. Love, "The Integration of the Equations of Propagation of Electric Waves," *Philosophical Transactions of the Royal Society of London. Series A, Containing Papers of a Mathematical or Physical Character* 197, 1-45 (1901).

[96] M. Sivis, M. Duwe, B. Abel, and C. Ropers, "Extreme-Ultraviolet Light Generation in Plasmonic Nanostructures," *Nat Phys* 9, 304-309 (2013).

[97] T. B. Hoang, G. M. Akselrod, C. Argyropoulos, J. Huang, D. R. Smith, and M. H. Mikkelsen, "Ultrafast Spontaneous Emission Source Using Plasmonic Nanoantennas," 6, 7788 (2015).

[98] S. A. Maier, and H. A. Atwater, "Plasmonics: Localization and Guiding of Electromagnetic Energy in Metal/Dielectric Structures," *J. Appl. Phys.* 98, 011101-011110 (2005).

[99] S. Kim, J. H. Jin, Y. J. Kim, I. Y. Park, Y. Kim, and S. W. Kim, "High-Harmonic Generation by Resonant Plasmon Field Enhancement," *Nature* 453, 757-760 (2008).

[100] J. Ye, F. Wen, H. Sobhani, J. B. Lassiter, P. V. Dorpe, P. Nordlander, and N. J. Halas, "Plasmonic Nanoclusters: Near Field Properties of the Fano Resonance Interrogated with Sers," *Nano Lett.* 12, 1660-1667 (2012).

[101] A. Slablab, L. Le Xuan, M. Zielinski, Y. de Wilde, V. Jacques, D. Chauvat, and J.-F. Roch, "Second-Harmonic Generation from Coupled Plasmon Modes in a Single Dimer of Gold Nanospheres," *Opt. Express* 20, 220-227 (2012).

[102] R. T. Hill, J. J. Mock, Y. Urzhumov, D. S. Sebba, S. J. Oldenburg, S.-Y. Chen, A. A. Lazarides, A. Chilkoti, and D. R. Smith, "Leveraging Nanoscale Plasmonic Modes to Achieve Reproducible Enhancement of Light," *Nano Letters* 10, 4150-4154 (2010).

[103] S. Sun, K.-Y. Yang, C.-M. Wang, T.-K. Juan, W. T. Chen, C. Y. Liao, Q. He, S. Xiao, W.-T. Kung, G.-Y. Guo, L. Zhou, and D. P. Tsai, "High-Efficiency Broadband Anomalous Reflection by Gradient Meta-Surfaces," *Nano Lett.* 12, 6223-6229 (2012).

[104] A. Pors, and S. I. Bozhevolnyi, "Plasmonic Metasurfaces for Efficient Phase Control in Reflection," *Opt. Express* 21, 27438-27451 (2013).

[105] A. Pors, M. G. Nielsen, R. L. Eriksen, and S. I. Bozhevolnyi, "Broadband Focusing Flat Mirrors Based on Plasmonic Gradient Metasurfaces," *Nano Lett.* 13, 829-834 (2013).

[106] L. Zhang, J. Hao, M. Qiu, S. Zouhdi, J. K. W. Yang, and C.-W. Qiu, "Anomalous Behavior of Nearly-Entire Visible Band Manipulated with Degenerated Image Dipole Array," *Nanoscale* 6, 12303-12309 (2014).

[107] G. Zheng, H. Mühlenbernd, M. Kenney, G. Li, T. Zentgraf, and S. Zhang, "Metasurface Holograms Reaching 80% Efficiency," *Nature Nanotechnol.* 10, 308-312 (2015).

[108] W. T. Chen, K.-Y. Yang, C.-M. Wang, Y.-W. Huang, G. Sun, I. D. Chiang, C. Y. Liao, W.-L. Hsu, H. T. Lin, S. Sun, L. Zhou, A. Q. Liu, and D. P. Tsai, "High-Efficiency Broadband Meta-Hologram with Polarization-Controlled Dual Images," *Nano Lett.* 14, 225-230 (2014).

[109] F. Aieta, P. Genevet, M. A. Kats, N. Yu, R. Blanchard, Z. Gaburro, and F. Capasso, "Aberration-Free Ultrathin Flat Lenses and Axicons at Telecom Wavelengths Based on Plasmonic Metasurfaces," *Nano Lett.* 12, 4932-4936 (2012).

[110] L. Huang, X. Chen, H. Mühlenbernd, H. Zhang, S. Chen, B. Bai, Q. Tan, G. Jin, K.-W. Cheah, C.-W. Qiu, J. Li, T. Zentgraf, and S. Zhang, "Three-Dimensional Optical Holography Using a Plasmonic Metasurface," *Nature Commun.* 4, 2808 (2013).

[111] D. Veksler, E. Maguid, N. Shitrit, D. Ozeri, V. Kleiner, and E. Hasman, "Multiple Wavefront Shaping by Metasurface Based on Mixed Random Antenna Groups," *ACS Photonics* 2, 661-667 (2015).

[112] N. Yu, P. Genevet, M. A. Kats, F. Aieta, J.-P. Tetienne, F. Capasso, and Z. Gaburro, "Light Propagation with Phase Discontinuities: Generalized Laws of Reflection and Refraction," *Science* 334, 333-337 (2011).

[113] X. Ni, N. K. Emani, A. V. Kildishev, A. Boltasseva, and V. M. Shalaev, "Broadband Light Bending with Plasmonic Nanoantennas," *Science* 335, 427-427 (2012).

[114] N. F. Yu, F. Aieta, P. Genevet, M. A. Kats, Z. Gaburro, and F. Capasso, "A Broadband, Background-Free Quarter-Wave Plate Based on Plasmonic Metasurfaces," *Nano Lett.* 12, 6328-6333 (2012).

[115] S. Sun, Q. He, S. Xiao, Q. Xu, X. Li, and L. Zhou, "Gradient-Index Meta-Surfaces as a Bridge Linking Propagating Waves and Surface Waves," *Nature Mater.* 11, 426-431 (2012).

[116] J. Duan, H. Guo, S. Dong, T. Cai, W. Luo, Z. Liang, Q. He, L. Zhou, and S. Sun, "High-Efficiency Chirality-Modulated Spoof Surface Plasmon Meta-Coupler," *Sci. Rep.* 7, 1354 (2017).

[117] L. Huang, X. Chen, B. Bai, Q. Tan, G. Jin, T. Zentgraf, and S. Zhang, "Helicity Dependent Directional Surface Plasmon Polariton Excitation Using a Metasurface with Interfacial Phase Discontinuity," *Light: Sci. Appl.* 2, e70 (2013).

[118] J. Lin, J. P. B. Mueller, Q. Wang, G. Yuan, N. Antoniou, X.-C. Yuan, and F. Capasso, "Polarization-Controlled Tunable Directional Coupling of Surface Plasmon Polaritons," *Science* 340, 331-334 (2013).

[119] X. Ni, S. Ishii, A. V. Kildishev, and V. M. Shalaev, "Ultra-Thin, Planar, Babinet-Inverted Plasmonic Metalenses," *Light: Sci. Appl.* 2, e72 (2013).

[120] X. Chen, L. Huang, H. Mühlenbernd, G. Li, B. Bai, Q. Tan, G. Jin, C.-W. Qiu, S. Zhang, and T. Zentgraf, "Dual-Polarity Plasmonic Metalens for Visible Light," 3, 1198 (2012).

[121] B. Walther, C. Helgert, C. Rockstuhl, F. Setzpfandt, F. Eilenberger, E.-B. Kley, F. Lederer, A. Tünnermann, and T. Pertsch, "Spatial and Spectral Light Shaping with Metamaterials," *Adv. Mater.* 24, 6300-6304 (2012).

[122] L. Huang, X. Chen, H. Mühlenbernd, H. Zhang, S. Chen, B. Bai, Q. Tan, G. Jin, K.-W. Cheah, C.-W. Qiu, J. Li, T. Zentgraf, and S. Zhang, "Three-Dimensional Optical Holography Using a Plasmonic Metasurface," 4, 2808 (2013).

[123] N. Yu, F. Aieta, P. Genevet, M. A. Kats, Z. Gaburro, and F. Capasso, "A Broadband, Background-Free Quarter-Wave Plate Based on Plasmonic Metasurfaces," *Nano Lett.* 12, 6328-6333 (2012).

[124] F. Ding, Z. Wang, S. He, V. M. Shalaev, and A. V. Kildishev, "Broadband High-Efficiency Half-Wave Plate: A Supercell-Based Plasmonic Metasurface Approach," *ACS Nano* 9, 4111-4119 (2015).

[125] C. Yan, K.-Y. Yang, and O. J. F. Martin, "Fano-Resonance-Assisted Metasurface for Color Routing," *Light Sci Appl.* 6, e17017 (2017).

[126] D. Wen, F. Yue, S. Kumar, Y. Ma, M. Chen, X. Ren, P. E. Kremer, B. D. Gerardot, M. R. Taghizadeh, G. S. Buller, and X. Chen, "Metasurface for Characterization of the Polarization State of Light," *Opt. Express* 23, 10272-10281 (2015).

[127] A. Shaltout, J. Liu, A. Kildishev, and V. Shalaev, "Photonic Spin Hall Effect in Gap-Plasmon Metasurfaces for on-Chip Chiroptical Spectroscopy," *Optica* 2, 860-863 (2015).

[128] A. Pors, M. G. Nielsen, and S. I. Bozhevolnyi, "Plasmonic Metagratings for Simultaneous Determination of Stokes Parameters," *Optica* 2, 716-723 (2015).

[129] Y.-J. Tsai, S. Larouche, T. Tyler, G. Lipworth, N. M. Jokerst, and D. R. Smith, "Design and Fabrication of a Metamaterial Gradient Index Diffraction Grating at Infrared Wavelengths," *Opt. Express* 19, 24411-24423 (2011).

[130] S. Larouche, Y.-J. Tsai, T. Tyler, N. M. Jokerst, and D. R. Smith, "Infrared Metamaterial Phase Holograms," *Nature Mater.* 11, 450-454 (2012).

[131] T. Koschny, P. Markoš, E. N. Economou, D. R. Smith, D. C. Vier, and C. M. Soukoulis, "Impact of Inherent Periodic Structure on Effective Medium Description of Left-Handed and Related Metamaterials," *Phys. Rev. B* 71, 245105 (2005).

[132] A. Rose, D. Huang, and D. R. Smith, "Controlling the Second Harmonic in a Phase-Matched Negative-Index Metamaterial," *Phys. Rev. Lett.* 107, 063902 (2011).

[133] M. Yamada, N. Nada, M. Saitoh, and K. Watanabe, "First-Order Quasi-Phase Matched Linbo3 Waveguide Periodically Poled by Applying an External Field for Efficient Blue Second-Harmonic Generation," *Appl. Phys. Lett.* 62, 435-436 (1993).

[134] G. Li, S. Zhang, and T. Zentgraf, "Nonlinear Photonic Metasurfaces," 2, 17010 (2017).

[135] F. Walter, G. Li, C. Meier, S. Zhang, and T. Zentgraf, "Ultrathin Nonlinear Metasurface for Optical Image Encoding," *Nano Lett.* 17, 3171-3175 (2017).

[136] W. Ye, F. Zeuner, X. Li, B. Reineke, S. He, C.-W. Qiu, J. Liu, Y. Wang, S. Zhang, and T. Zentgraf, "Spin and Wavelength Multiplexed Nonlinear Metasurface Holography," 7, 11930 (2016).

[137] D. Baykusheva, M. S. Ahsan, N. Lin, and H. J. Wörner, "Bicircular High-Harmonic Spectroscopy Reveals Dynamical Symmetries of Atoms and Molecules," *Phys. Rev. Lett.* 116, 123001 (2016).

[138] I. A. Walmsley, "Quantum Optics: Science and Technology in a New Light," *Science* 348, 525-530 (2015).

[139] E. A. Mamonov, T. V. Murzina, I. A. Kolmychek, A. I. Maydykovsky, V. K. Valev, A. V. Silhanek, T. Verbiest, V. V. Moshchalkov, and O. A. Aktsipetrov, "Chirality in Nonlinear-Optical Response of Planar G-Shaped Nanostructures," *Opt. Express* 20, 8518-8523 (2012).

[140] V. K. Valev, X. Zheng, C. G. Biris, A. V. Silhanek, V. Volskiy, B. De Clercq, O. A. Aktsipetrov, M. Ameloot, N. C. Panoiu, G. A. E. Vandenbosch, and V. V. Moshchalkov, "The Origin of Second Harmonic Generation Hotspots in Chiral Optical Metamaterials [Invited]," *Opt. Mater. Express* 1, 36-45 (2011).

[141] V. K. Valev, J. J. Baumberg, B. De Clercq, N. Braz, X. Zheng, E. J. Osley, S. Vandendriessche, M. Hojeij, C. Blejean, J. Mertens, C. G. Biris, V. Volskiy, M. Ameloot, Y. Ekinci, G. A. E. Vandenbosch, P. A. Warburton, V. V. Moshchalkov, N. C. Panoiu, and T. Verbiest, "Nonlinear Superchiral Meta-Surfaces: Tuning Chirality and Disentangling Non-Reciprocity at the Nanoscale," *Adv. Mater.* 26, 4074-4081 (2014).

[142] A. M. Kern, and O. J. F. Martin, "Excitation and Reemission of Molecules near Realistic Plasmonic Nanostructures," *Nano Lett.* 11, 482-487 (2011).

[143] B. Gallinet, J. Butet, and O. J. F. Martin, "Numerical Methods for Nanophotonics: Standard Problems and Future Challenges," *Laser Photonics Rev.* 9, 577-603 (2015).

[144] T. V. Raziman, and O. J. F. Martin, "Polarisation Charges and Scattering Behaviour of Realistically Rounded Plasmonic Nanostructures," *Opt. Express* 21, 21500-21507 (2013).

[145] J. Butet, K. Thyagarajan, and O. J. F. Martin, "Ultrasensitive Optical Shape Characterization of Gold Nanoantennas Using Second Harmonic Generation," *Nano Lett.* 13, 1787-1792 (2013).

[146] J. Mäkitalo, S. Suuriniemi, and M. Kauranen, "Enforcing Symmetries in Boundary Element Formulation of Plasmonic and Second-Harmonic Scattering Problems," *J. Opt. Soc. Am.* 31 (2014).

[147] M. Nieto-Vesperinas, *Scattering and Diffraction in Physical Optics* (2006).

[148] D. L. Colton, and R. Kress, *Integral Equation Methods in Scattering Theory* (Krieger Publishing Company, 1992).

[149] A. M. Kern, and O. J. F. Martin, "Surface Integral Formulation for 3d Simulations of Plasmonic and High Permittivity Nanostructures," *Journal of the Optical Society of America A* 26, 732-740 (2009).

[150] B. Gallinet, A. M. Kern, and O. J. F. Martin, "Accurate and Versatile Modeling of Electromagnetic Scattering on Periodic Nanostructures with a Surface Integral Approach," *J. Opt. Soc. Am. A* 27, 2261-2271 (2010).

[151] B. Gallinet, and O. J. F. Martin, "Scattering on Plasmonic Nanostructures Arrays Modeled with a Surface Integral Formulation," *Photonics Nanostruct. Fundam. Appl.* 8, 278-284 (2010).

[152] S. Rao, D. Wilton, and A. Glisson, "Electromagnetic Scattering by Surfaces of Arbitrary Shape," *IEEE Trans. Antennas. Propag.* 30, 409-418 (1982).

[153] I. Stevanovic, P. Crespo-Valero, K. Blagovic, F. Bongard, and J. R. Mosig, "Integral-Equation Analysis of 3-D Metallic Objects Arranged in 2-D Lattices Using the Ewald Transformation," *IEEE Trans. Microwave Theory Tech.* 54, 3688-3697 (2006).

[154] T.-K. Wu, and L. L. Tsai, "Scattering from Arbitrarily-Shaped Lossy Dielectric Bodies of Revolution," *Radio Sci.* 12, 709-718 (1977).

[155] J. E. Sipe, V. C. Y. So, M. Fukui, and G. I. Stegeman, "Analysis of Second-Harmonic Generation at Metal Surfaces," *Phys. Rev. B* 21, 4389-4402 (1980).

[156] F. X. Wang, F. J. Rodriguez, M. Kauranen, W. M. Albers, R. Ahorinta, and J. E. Sipe, "Surface and Bulk Contributions to the Second-Order Nonlinearity of Gold," in *2009 Conference on Lasers and Electro-Optics and 2009 Conference on Quantum electronics and Laser Science Conference*(2009), pp. 1-2.

[157] J. Mäkitalo, S. Suuriniemi, and M. Kauranen, "Boundary Element Method for Surface Nonlinear Optics of Nanoparticles," *Opt. Express* 19, 23386-23399 (2011).

[158] T. F. Heinz, "Second-Order Nonlinear Optical Effects at Surfaces and Interfaces," in *Nonlinear Surface Electromagnetic Phenomena*(Elsevier, 1991).

[159] R. F. Harrington, *Field Computation by Moment Methods* (IEEE Press, 1993).

[160] M. Kauranen, and A. V. Zayats, "Nonlinear Plasmonics," *Nat. Photonics* 6, 737-748 (2012).

[161] J. Butet, B. Gallinet, K. Thyagarajan, and O. J. F. Martin, "Second-Harmonic Generation from Periodic Arrays of Arbitrary Shape Plasmonic Nanostructures: A Surface Integral Approach," *J. Opt. Soc. Am. B* 30, 2970-2979 (2013).

[162] K.-Y. Yang, J. Butet, C. Yan, G. D. Bernasconi, and O. J. F. Martin, "Enhancement Mechanisms of the Second Harmonic Generation from Double Resonant Aluminum Nanostructures," *ACS Photonics* 4, 1522-1530 (2017).

[163] K. Thyagarajan, C. Santschi, P. Langlet, and O. J. F. Martin, "Highly Improved Fabrication of Ag and Al Nanostructures for Uv and Nonlinear Plasmonics," *Advanced Optical Materials* 4, 871-876 (2016).

[164] X. Wang, C. Santschi, and O. J. F. Martin, "Strong Improvement of Long-Term Chemical and Thermal Stability of Plasmonic Silver Nanoantennas and Films," *Small*, 1700044-n/a.

[165] M. J. Verkerk, and W. A. M. C. Brankaert, "Effects of Water on the Growth of Aluminium Films Deposited by Vacuum Evaporation," *Thin Solid Films* 139, 77-88 (1986).

[166] S. Viarbitskaya, O. Demichel, B. Cluzel, G. Colas des Francs, and A. Bouhelier, "Delocalization of Nonlinear Optical Responses in Plasmonic Nanoantennas," *Phys. Rev. Lett.* 115, 197401 (2015).

[167] C. Yan, X. Wang, T. V. Raziman, and O. J. F. Martin, "Twisting Fluorescence through Extrinsic Chiral Antennas," *Nano Lett.* 17, 2265-2272 (2017).

[168] H. Harutyunyan, G. Volpe, R. Quidant, and L. Novotny, "Enhancing the Nonlinear Optical Response Using Multifrequency Gold-Nanowire Antennas," *Physical Review Letters* 108, 217403 (2012).

[169] K. Thyagarajan, S. Rivier, A. Lovera, and O. J. F. Martin, "Enhanced Second-Harmonic Generation from Double Resonant Plasmonic Antennae," *Opt. Express* 20, 12860-12865 (2012).

[170] H. Aouani, M. Navarro-Cia, M. Rahmani, T. P. H. Sidiropoulos, M. Hong, R. F. Oulton, and S. A. Maier, "Multiresonant Broadband Optical Antennas as Efficient

Tunable Nanosources of Second Harmonic Light," *Nano Letters* 12, 4997-5002 (2012).

[171] K. Thyagarajan, J. Butet, and O. J. F. Martin, "Augmenting Second Harmonic Generation Using Fano Resonances in Plasmonic Systems," *Nano Lett.* 13, 1847-1851 (2013).

[172] M. Abb, Y. Wang, C. H. de Groot, and O. L. Muskens, "Hotspot-Mediated Ultrafast Nonlinear Control of Multifrequency Plasmonic Nanoantennas," *Nat Commun* 5 (2014).

[173] M. Celebrano, X. Wu, M. Baselli, S. Großmann, P. Biagioni, A. Locatelli, C. De Angelis, G. Cerullo, R. Osellame, B. Hecht, L. Duò, F. Ciccacci, and M. Finazzi, "Mode Matching in Multiresonant Plasmonic Nanoantennas for Enhanced Second Harmonic Generation," *Nat Nano* 10, 412-417 (2015).

[174] B. Metzger, M. Hentschel, and H. Giessen, "Probing the near-Field of Second-Harmonic Light around Plasmonic Nanoantennas," *Nano Letters* 17, 1931-1937 (2017).

[175] S. D. Gennaro, M. Rahmani, V. Giannini, H. Aouani, T. P. H. Sidiropoulos, M. Navarro-Cía, S. A. Maier, and R. F. Oulton, "The Interplay of Symmetry and Scattering Phase in Second Harmonic Generation from Gold Nanoantennas," *Nano Lett.* 16, 5278-5285 (2016).

[176] J. Butet, G. Bachelier, I. Russier-Antoine, C. Jonin, E. Benichou, and P. F. Brevet, "Interference between Selected Dipoles and Octupoles in the Optical Second-Harmonic Generation from Spherical Gold Nanoparticles," *Physical Review Letters* 105, 077401 (2010).

[177] S. Kim, J. Jin, Y.-J. Kim, I.-Y. Park, Y. Kim, and S.-W. Kim, "High-Harmonic Generation by Resonant Plasmon Field Enhancement," *Nature* 453, 757-760 (2008).

[178] J. Butet, and O. J. F. Martin, "Refractive Index Sensing with Fano Resonant Plasmonic Nanostructures: A Symmetry Based Nonlinear Approach," *Nanoscale* 6, 15262-15270 (2014).

[179] J. Butet, I. Russier-Antoine, C. Jonin, N. Lascoux, E. Benichou, and P.-F. Brevet, "Effect of the Dielectric Core and Embedding Medium on the Second Harmonic Generation from Plasmonic Nanoshells: Tunability and Sensing," *The Journal of Physical Chemistry C* 117, 1172-1177 (2012).

[180] J. J. Maki, M. Kauranen, and A. Persoons, "Surface Second-Harmonic Generation from Chiral Materials," *Physical Review B* 51, 1425-1434 (1995).

[181] V. K. Valev, "Characterization of Nanostructured Plasmonic Surfaces with Second Harmonic Generation," *Langmuir* 28, 15454-15471 (2012).

[182] M. Kauranen, and A. V. Zayats, "Nonlinear Plasmonics," *Nat Photon* 6, 737-748 (2012).

[183] M. Ren, E. Plum, J. Xu, and N. I. Zheludev, "Giant Nonlinear Optical Activity in a Plasmonic Metamaterial," *Nat Commun* 3, 833 (2012).

[184] J. Butet, I. Russier-Antoine, C. Jonin, N. Lascoux, E. Benichou, and P.-F. Brevet, "Sensing with Multipolar Second Harmonic Generation from Spherical Metallic Nanoparticles," *Nano Letters* 12, 1697-1701 (2012).

[185] K.-Y. Yang, J. Butet, C. Yan, G. D. Bernasconi, and O. J. F. Martin, "Enhancement Mechanisms of the Second Harmonic Generation from Double Resonant Aluminum Nanostructures," *ACS Photonics* (2017).

[186] J. Butet, and O. J. F. Martin, "Nonlinear Plasmonic Nanorulers," *ACS Nano* 8, 4931-4939 (2014).

[187] J. Mäkitalo, S. Suuriniemi, and M. Kauranen, "Boundary Element Method for Surface Nonlinear Optics of Nanoparticles," *Opt. Express* 19, 23386-23399 (2011).

[188] M. Agio, and A. Alù, *Optical Antennas* (Cambridge University Press, 2013).

[189] S. Mühlig, C. Menzel, C. Rockstuhl, and F. Lederer, "Multipole Analysis of Meta-Atoms," *Metamaterials* 5, 64-73 (2011).

[190] A. Rose, and D. R. Smith, "Overcoming Phase Mismatch in Nonlinear Metamaterials [Invited]," *Optical Materials Express* 1, 1232-1243 (2011).

[191] J. I. Dadap, J. Shan, K. B. Eisenthal, and T. F. Heinz, "Theory of Second-Harmonic Generation from a Sphere of Centrosymmetric Material," in *Technical Digest. Summaries of Papers Presented at the Quantum Electronics and Laser Science Conference*(1999), p. 179.

[192] J. Nappa, G. Revillod, I. Russier-Antoine, E. Benichou, C. Jonin, and P. F. Brevet, "Electric Dipole Origin of the Second Harmonic Generation of Small Metallic Particles," *Physical Review B* 71, 165407 (2005).

[193] I. Russier-Antoine, E. Benichou, G. Bachelier, C. Jonin, and P. F. Brevet, "Multipolar Contributions of the Second Harmonic Generation from Silver and Gold Nanoparticles," *The Journal of Physical Chemistry C* 111, 9044-9048 (2007).

[194] C. Anceau, S. Brasselet, J. Zyss, and P. Gadenne, "Local Second-Harmonic Generation Enhancement on Gold Nanostructures Probed by Two-Photon Microscopy," *Opt. Lett.* 28, 713-715 (2003).

[195] D. Yelin, D. Oron, S. Thiberge, E. Moses, and Y. Silberberg, "Multiphoton Plasmon-Resonance Microscopy," *Opt. Express* 11, 1385-1391 (2003).

[196] K.-Y. Yang, R. Verre, J. Butet, C. Yan, T. J. Antosiewicz, M. Käll, and O. J. F. Martin, "Wavevector-Selective Nonlinear Plasmonic Metasurfaces," *Nano Lett.* 17, 5258-5263 (2017).

[197] N. Meinzer, W. L. Barnes, and I. R. Hooper, "Plasmonic Meta-Atoms and Metasurfaces," *Nature Photonics* 8, 889-898 (2014).

[198] S. Jahani, and Z. Jacob, "All-Dielectric Metamaterials," *Nature Nanotechnol.* 11, 23-36 (2016).

[199] J. B. Pendry, "Negative Refraction Makes a Perfect Lens," *Phys. Rev. Lett.* 85, 3966-3969 (2000).

[200] J. B. Pendry, and S. A. Ramakrishna, "Focusing Light Using Negative Refraction," *J. Phys. Condens. Matter* 15, 6345 (2003).

[201] C. Pfeiffer, and A. Grbic, "Metamaterial Huygens' Surfaces: Tailoring Wave Fronts with Reflectionless Sheets," *Phys. Rev. Lett.* 110, 197401 (2013).

[202] Z. H. Jiang, S. Yun, L. Lin, J. A. Bossard, D. H. Werner, and T. S. Mayer, "Tailoring Dispersion for Broadband Low-Loss Optical Metamaterials Using Deep-Subwavelength Inclusions," 3, 1571 (2013).

[203] R. Verre, N. Maccaferri, K. Fleischer, M. Svedendahl, N. Odebo Lank, A. Dmitriev, P. Vavassori, I. V. Shvets, and M. Kall, "Polarization Conversion-Based Molecular Sensing Using Anisotropic Plasmonic Metasurfaces," *Nanoscale* 8, 10576-10581 (2016).

[204] A. Hakonen, M. Svedendahl, R. Ogier, Z.-J. Yang, K. Lodewijks, R. Verre, T. Shegai, P. O. Andersson, and M. Kall, "Dimer-on-Mirror Sers Substrates with Attogram Sensitivity Fabricated by Colloidal Lithography," *Nanoscale* 7, 9405-9410 (2015).

[205] M. Svedendahl, R. Verre, and M. Kall, "Refractometric Biosensing Based on Optical Phase Flips in Sparse and Short-Range-Ordered Nanoplasmonic Layers," *Light: Sci. Appl.* 3, e220 (2014).

[206] C. Yan, K.-Y. Yang, and O. J. Martin, "Fano-Resonance-Assisted Metasurface for Color Routing," *Light: Sci. Appl.* 6, e17017 (2017).

[207] A. E. Minovich, A. E. Miroshnichenko, A. Y. Bykov, T. V. Murzina, D. N. Neshev, and Y. S. Kivshar, "Functional and Nonlinear Optical Metasurfaces," *Laser Photonics Rev.* 9, 195-213 (2015).

[208] R. Czaplicki, H. Husu, R. Siikanen, J. Mäkitalo, M. Kauranen, J. Laukkanen, J. Lehtolahti, and M. Kuittinen, "Enhancement of Second-Harmonic Generation from Metal Nanoparticles by Passive Elements," *Phys. Rev. Lett.* 110, 093902 (2013).

[209] S. Kruk, M. Weismann, A. Y. Bykov, E. A. Mamonov, I. A. Kolmychek, T. Murzina, N. C. Panoiu, D. N. Neshev, and Y. S. Kivshar, "Enhanced Magnetic Second-

Harmonic Generation from Resonant Metasurfaces," *ACS Photonics* 2, 1007-1012 (2015).

[210] J. Lee, M. Tymchenko, C. Argyropoulos, P.-Y. Chen, F. Lu, F. Demmerle, G. Boehm, M.-C. Amann, A. Alu, and M. A. Belkin, "Giant Nonlinear Response from Plasmonic Metasurfaces Coupled to Intersubband Transitions," *Nature* 511, 65-69 (2014).

[211] H. Linnenbank, and S. Linden, "Second Harmonic Generation Spectroscopy on Second Harmonic Resonant Plasmonic Metamaterials," *Optica* 2, 698-701 (2015).

[212] B. Metzger, M. Hentschel, and H. Giessen, "Ultrafast Nonlinear Plasmonic Spectroscopy: From Dipole Nanoantennas to Complex Hybrid Plasmonic Structures," *ACS Photonics* 3, 1336-1350 (2016).

[213] V. A. Fedotov, J. Wallauer, M. Walther, M. Perino, N. Papasimakis, and N. I. Zheludev, "Wavevector Selective Metasurfaces and Tunnel Vision Filters," *Light: Sci. Appl.* 4, e306 (2015).

[214] R. Czaplicki, A. Kiviniemi, J. Laukkanen, J. Lehtolahti, M. Kuittinen, and M. Kauranen, "Surface Lattice Resonances in Second-Harmonic Generation from Metasurfaces," *Opt. Lett.* 41, 2684-2687 (2016).

[215] G. Bautista, M. J. Huttunen, J. M. Kontio, J. Simonen, and M. Kauranen, "Third- and Second-Harmonic Generation Microscopy of Individual Metal Nanocones Using Cylindrical Vector Beams," *Opt. Express* 21, 21918-21923 (2013).

[216] P. Reichenbach, A. Horneber, D. A. Gollmer, A. Hille, J. Mihaljevic, C. Schäfer, D. P. Kern, A. J. Meixner, D. Zhang, M. Fleischer, and L. M. Eng, "Nonlinear Optical Point Light Sources through Field Enhancement at Metallic Nanocones," *Opt. Express* 22, 15484-15501 (2014).

[217] R. Verre, M. Svedendahl, N. O. Lank, Z. J. Yang, G. Zengin, T. J. Antosiewicz, and M. Kall, "Directional Light Extinction and Emission in a Metasurface of Tilted Plasmonic Nanopillars," *Nano Lett.* 16, 98-104 (2016).

[218] A. Bouhelier, M. Beversluis, A. Hartschuh, and L. Novotny, "Near-Field Second-Harmonic Generation Induced by Local Field Enhancement," *Phys. Rev. Lett.* 90, 013903 (2003).

[219] C. C. Neacsu, G. A. Reider, and M. B. Raschke, "Second-Harmonic Generation from Nanoscopic Metal Tips: Symmetry Selection Rules for Single Asymmetric Nanostructures," *Phys. Rev. B* 71, 201402 (2005).

[220] A. Anderson, K. S. Deryckx, X. G. Xu, G. Steinmeyer, and M. B. Raschke, "Few-Femtosecond Plasmon Dephasing of a Single Metallic Nanostructure from Optical Response Function Reconstruction by Interferometric Frequency Resolved Optical Gating," *Nano Lett.* 10, 2519-2524 (2010).

[221] G. Bautista, M. J. Huttunen, J. Mäkitalo, J. M. Kontio, J. Simonen, and M. Kauranen, "Second-Harmonic Generation Imaging of Metal Nano-Objects with Cylindrical Vector Beams," *Nano Lett.* 12, 3207-3212 (2012).

[222] O. J. F. Martin, and C. Girard, "Controlling and Tuning Strong Optical Field Gradients at a Local Probe Microscope Tip Apex," *Appl. Phys. Lett.* 70, 705-707 (1997).

[223] T. Xu, X. Jiao, G. P. Zhang, and S. Blair, "Second-Harmonic Emission from Sub-Wavelength Apertures: Effects of Aperture Symmetry and Lattice Arrangement," *Opt. Express* 15, 13894-13906 (2007).

[224] N. Bloembergen, and P. S. Pershan, "Light Waves at the Boundary of Nonlinear Media," *Physical Review* 128, 606-622 (1962).

[225] N. Bloembergen, R. K. Chang, S. S. Jha, and C. H. Lee, "Optical Second-Harmonic Generation in Reflection from Media with Inversion Symmetry," *Physical Review* 174, 813-822 (1968).

[226] D. Smirnova, and Y. S. Kivshar, "Multipolar Nonlinear Nanophotonics," *Optica* 3, 1241-1255 (2016).

[227] L. Novotny, and B. Hecht, "Principles of Nano-Optics," *(Cambridge University Press, Cambridge, England).* (2006).

[228] J. Butet, B. Gallinet, K. Thyagarajan, and O. J. F. Martin, "Second-Harmonic Generation from Periodic Arrays of Arbitrary Shape Plasmonic Nanostructures: A Surface Integral Approach," *J. Opt. Soc. Am. B* 30, 2970-2979 (2013).

[229] J. Butet, and O. J. F. Martin, "Evaluation of the Nonlinear Response of Plasmonic Metasurfaces: Miller's Rule, Nonlinear Effective Susceptibility Method, and Full-Wave Computation," *J. Opt. Soc. Am. B* 33, A8-A15 (2016).

[230] W. Ye, X. Li, J. Liu, and S. Zhang, "Phenomenological Modeling of Nonlinear Holograms Based on Metallic Geometric Metasurfaces," *Opt. Express* 24, 25805-25815 (2016).

[231] S. Kujala, B. K. Canfield, M. Kauranen, Y. Svirko, and J. Turunen, "Multipole Interference in the Second-Harmonic Optical Radiation from Gold Nanoparticles," *Phys. Rev. Lett.* 98, 167403 (2007).

[232] J. Butet, T. V. Raziman, K.-Y. Yang, G. D. Bernasconi, and O. J. F. Martin, "Controlling the Nonlinear Optical Properties of Plasmonic Nanoparticles with the Phase of Their Linear Response," *Opt. Express* 24, 17138-17148 (2016).

[233] J. Butet, and O. J. F. Martin, "Evaluation of the Nonlinear Response of Plasmonic Metasurfaces: Miller's Rule, Nonlinear Effective Susceptibility Method, and Full-Wave Computation," *J. Opt. Soc. Am. B* 33, A8-A15 (2016).

[234] H. Husu, B. K. Canfield, J. Laukkanen, B. Bai, M. Kuittinen, J. Turunen, and M. Kauranen, "Local-Field Effects in the Nonlinear Optical Response of Metamaterials," *Metamaterials* 2, 155-168 (2008).

[235] P. Ginzburg, A. Krasavin, Y. Sonnefraud, A. Murphy, R. J. Pollard, S. A. Maier, and A. V. Zayats, "Nonlinearly Coupled Localized Plasmon Resonances: Resonant Second-Harmonic Generation," *Phys. Rev. B* 86, 085422 (2012).

[236] B. H. Kleemann, J. Ruoff, and R. Arnold, "Area-Coded Effective Medium Structures, a New Type of Grating Design," *Opt. Lett.* 30, 1617-1619 (2005).

[237] B. Bai, X. Meng, J. Laukkanen, T. Sfez, L. Yu, W. Nakagawa, H. P. Herzig, L. Li, and J. Turunen, "Asymmetrical Excitation of Surface Plasmon Polaritons on Blazed Gratings at Normal Incidence," *Phys. Rev. B* 80, 035407 (2009).

[238] Z. Li, E. Palacios, S. Butun, and K. Aydin, "Visible-Frequency Metasurfaces for Broadband Anomalous Reflection and High-Efficiency Spectrum Splitting," *Nano Lett.* 15, 1615-1621 (2015).

[239] R. B. M. Schasfoort, and A. J. Tudos, *Handbook of Surface Plasmon Resonance* (Royal Society of Chemistry, 2008).

[240] A. Farhang, T. Siegfried, Y. Ekinci, H. Sigg, and O. J. F. Martin, "Large-Scale Sub-100 nm Compound Plasmonic Grating Arrays to Control the Interaction between Localized and Propagating Plasmons," *J. Nanophotonics* 8, 083897-083897 (2014).

[241] E. Almeida, G. Shalem, and Y. Prior, "Subwavelength Nonlinear Phase Control and Anomalous Phase Matching in Plasmonic Metasurfaces," *Nature Commun.* 7, 10367 (2016).

[242] E. Almeida, O. Bitton, and Y. Prior, "Nonlinear Metamaterials for Holography," *Nature Commun.* 7, 12533 (2016).

[243] W. Fan, S. Zhang, N. C. Panoiu, A. Abdenour, S. Krishna, R. M. Osgood, K. J. Malloy, and S. R. J. Brueck, "Second Harmonic Generation from a Nanopatterned Isotropic Nonlinear Material," *Nano Lett.* 6, 1027-1030 (2006).

[244] M. Hentschel, B. Metzger, B. Knabe, K. Buse, and H. Giessen, "Linear and Nonlinear Optical Properties of Hybrid Metallic–Dielectric Plasmonic Nanoantennas," *Beilstein Journal of Nanotechnology* 7, 111-120 (2016).

[245] J. Lee, N. Nookala, J. S. Gomez-Diaz, M. Tymchenko, F. Demmerle, G. Boehm, M.-C. Amann, A. Alù, and M. A. Belkin, "Ultrathin Second-Harmonic Metasurfaces with Record-High Nonlinear Optical Response," *Adv. Opt. Mater.* 4, 664-670 (2016).

[246] S. Lan, L. Kang, D. T. Schoen, S. P. Rodrigues, Y. Cui, M. L. Brongersma, and W. Cai, "Backward Phase-Matching for Nonlinear Optical Generation in Negative-Index Materials," *Nature Mater.* 14, 807-811 (2015).

[247] V. K. Valev, B. De Clercq, C. G. Biris, X. Zheng, S. Vandendriessche, M. Hojeij, D. Denkova, Y. Jeyaram, N. C. Panoiu, Y. Ekinci, A. V. Silhanek, V. Volskiy, G. A. E. Vandenbosch, M. Ameloot, V. V. Moshchalkov, and T. Verbiest, "Distributing the Optical near-Field for Efficient Field-Enhancements in Nanostructures," *Adv. Mater.* 24, OP208-OP215 (2012).

[248] S. Herminjard, L. Sirigu, H. P. Herzig, E. Studemann, A. Crottini, J.-P. Pellaux, T. Gresch, M. Fischer, and J. Faist, "Surface Plasmon Resonance Sensor Showing Enhanced Sensitivity for Co2 Detection in the Mid-Infrared Range," *Opt. Express* 17, 293-303 (2009).

[249] K.-H. Dostert, M. Álvarez, K. Koynov, A. del Campo, H.-J. Butt, and M. Kreiter, "Near Field Guided Chemical Nanopatterning," *Langmuir* 28, 3699-3703 (2012).

[250] A. Nitzan, and L. E. Brus, "Theoretical Model for Enhanced Photochemistry on Rough Surfaces," *The Journal of Chemical Physics* 75, 2205-2214 (1981).

[251] H. A. Atwater, and A. Polman, "Plasmonics for Improved Photovoltaic Devices," 9, 205 (2010).

[252] A. Naqavi, F.-J. Haug, C. Battaglia, H. P. Herzig, and C. Ballif, "Light Trapping in Solar Cells at the Extreme Coupling Limit," *J. Opt. Soc. Am. B* 30, 13-20 (2013).

[253] A. Naqavi, K. Söderström, F.-J. Haug, V. Paeder, T. Scharf, H. P. Herzig, and C. Ballif, "Understanding of Photocurrent Enhancement in Real Thin Film Solar Cells: Towards Optimal One-Dimensional Gratings," *Opt. Express* 19, 128-140 (2011).

[254] T. Ning, H. Pietarinen, O. Hyvärinen, R. Kumar, T. Kaplas, M. Kauranen, and G. Genty, "Efficient Second-Harmonic Generation in Silicon Nitride Resonant Waveguide Gratings," *Opt. Lett.* 37, 4269-4271 (2012).

[255] M. Siltanen, S. Leivo, P. Voima, M. Kauranen, P. Karvinen, P. Vahimaa, and M. Kuittinen, "Strong Enhancement of Second-Harmonic Generation in All-Dielectric Resonant Waveguide Grating," *Appl. Phys. Lett.* 91, 111109 (2007).

[256] I. Staude, A. E. Miroshnichenko, M. Decker, N. T. Fofang, S. Liu, E. Gonzales, J. Dominguez, T. S. Luk, D. N. Neshev, I. Brener, and Y. Kivshar, "Tailoring Directional Scattering through Magnetic and Electric Resonances in Subwavelength Silicon Nanodisks," *ACS Nano* 7, 7824-7832 (2013).

[257] K. E. Chong, B. Hopkins, I. Staude, A. E. Miroshnichenko, J. Dominguez, M. Decker, D. N. Neshev, I. Brener, and Y. S. Kivshar, "Observation of Fano Resonances in All-Dielectric Nanoparticle Oligomers," Small 10, 1985-1990 (2014).

Curriculum Vitae

Personal Information

Name: Kuang-Yu Yang
Date of birth: Aug 14, 1988
Nationality: Taiwan
Address: Avenue du Chateau 22, CH-1008, Prilly, Switzerland
Email :   piano77814@gmail.com

Education

2014 – 2018   **PhD in nanophotonics.** École Polytechnique Fédérale de Lausanne (EPFL), Switzerland.

Thesis: ''Plasmonic Metasurfaces to Tailor Second Harmonic Generation''

2010 – 2012   **Master of Applied Physics.** National Taiwan University (NTU), Graduate Institute of Applied Physics, Taiwan.

Thesis: ''Manipulate light propagation based on gradient-phase meta-interfaces''

2006 – 2010   **Bachelor of Physics.** Chung Yuan Christian University (CYCU), Department of Physics, Taiwan.

Thesis: ''Voltage-assisted photoaligning effect of an azo dye doped in a liquid crystal with negative dielectric anisotropy''

Peer Reviewed Publications

1. C. Yan, K.-Y. Yang, and O. J. F. Martin, "Fano-Resonance-Assisted Metasurface for Color Routing," Light Sci Appl. 6, e17017 (2017).

2. K.-Y. Yang, J. Butet, C. Yan, G. D. Bernasconi, and O. J. F. Martin, "Enhancement Mechanisms of the Second Harmonic Generation from Double Resonant Aluminum Nanostructures," ACS Photonics 4, 1522-1530 (2017).

3. K.-Y. Yang, R. Verre, J. Butet, C. Yan, T. J. Antosiewicz, M. Käll, and O. J. F. Martin, "Wavevector-Selective Nonlinear Plasmonic Metasurfaces," Nano Lett. 17, 5258-5263 (2017).

4. J. Butet, T. V. Raziman, K.-Y. Yang, G. D. Bernasconi, and O. J. F. Martin, "Controlling the Nonlinear Optical Properties of Plasmonic Nanoparticles with the Phase of Their Linear Response," Opt. Express 24, 17138-17148 (2016).

5. J. Butet, K.-Y. Yang, S. Dutta-Gupta, and O. J. F. Martin, "Maximizing Nonlinear Optical Conversion in Plasmonic Nanoparticles through Ideal Absorption of Light," ACS Photonics 3, 1453-1460 (2016).

Publication in Preparation

1. K.-Y. Yang, J. Butet, X. Wang, C. Yen and O. J. F. Martin, "Surface nonlinear optics beyond

the standard reflection laws," to be submitted to Nature Communications.

Presentations

1. K.-Y. Yang, J. Butet, X. Wang, C. Yen and O. J. F. Martin, "Second Harmonic Generation from Reflective Gradient Metasurfaces," The 8th Int. Conf. on Surface Plasmon Photonics SPP8, Taipei, Taiwan (2017).

2. K.-Y. Yang, R. Verre, J. Butet, C. Yan, T. J. Antosiexicz, M. Käll and O. J. F. Martin, "Out-of-plane Nonlinear Susceptibilities in 3-D Nanostructure Arrays," The 8th Int. Conf. on Surface Plasmon Photonics SPP8, Taipei, Taiwan (2017).

3. K.-Y. Yang, J. Butet and O. J. F. Martin, "Second Harmonic Generation in Reflective Gradient Metasurfaces," The 8th Int. Conf. on Nanophotonics ICNP, Taipei, Taiwan (2016).

4. K.-Y. Yang, J. Butet and O. J. F. Martin, "Mechanisms of Second Harmonic Generation in Plasmonic Nanostructures," The 7th Int. Conf. on Surface Plasmon Photonics SPP7, Jerusalem, Isreal (2015).